An investigation into the dynamical and statistical properties of dominant ocean surface waves using close-range remote sensing

Mika Petteri Malila

Thesis for the degree of Philosophiae Doctor (PhD)
University of Bergen, Norway
2022

UNIVERSITY OF BERGEN

An investigation into the dynamical and statistical properties of dominant ocean surface waves using close-range remote sensing

Mika Petteri Malila

Thesis for the degree of Philosophiae Doctor (PhD)
at the University of Bergen

Date of defense: 16.09.2022

Year: 2022

Title: An investigation into the dynamical and statistical properties of dominant ocean surface waves using close-range remote sensing

Name: Mika Petteri Malila

Print: Skipnes Kommunikasjon / University of Bergen

Scientific environment

This thesis is submitted in partial fulfillment of the degree of Philosophiae Doctor (PhD) at the Geophysical Institute at the University of Bergen, Norway. The research was to a large part carried out at the Norwegian Meteorological Institute (MET Norway) in Bergen, Norway. The main funding was provided by the StereoWave joint industry project financed by MET Norway, ConocoPhillips Norway ASA and Equinor ASA. A substantial portion of the research was also carried out at the Department of Civil and Environmental Engineering at the University of Washington (UW) in Seattle, Washington, USA. The 15-month exchange at UW was funded by the Valle Scholarship and internal UW funding. Throughout the course of this work, the author has been enrolled in the Norwegian Research School on Changing Climates in the coupled Earth System (CHESS). The work presented herein was done under the supervision of Pr. Øyvind Breivik and Pr. Kai H. Christensen at MET Norway and the Universities of Bergen and Oslo, respectively, and Pr. Jim Thomson at the Applied Physics Laboratory at UW.

UNIVERSITY OF BERGEN

Acknowledgements

I would like to express my gratitude to my advisors Øyvind Breivik, Jim Thomson and Kai Christensen for their support and guidance throughout the last four years. A number of other people have also provided me with excellent knowledge and advice. Among those are my close colleagues at MET Norway, especially Anne Karin Magnusson, Patrik Bohlinger, Konstantinos Christakos and Jan-Victor Björkqvist, as well as the rest of the Oceanography and Marine Meteorology group in Bergen. I would also like to thank my international colleagues and collaborators: Brian Ward and Brian Scanlon at NUI Galway, for their assistance with the Ekofisk cameras; Alvise Benetazzo, Filippo Bergamasco, Francesco Barbariol and Silvio Davison at ISMAR, for their input on stereo processing and space-time statistics; Susanne Støle-Hentschel at ENS Paris-Saclay, for help with wave signal processing; and the Environmental Fluid Mechanics community at the University of Washington, for their hospitality. Lars Bahr and Kjell Sandve at ConocoPhillips Norway have also provided valuable technical support on all things related to the scientific instrumentation at Ekofisk. Lastly, I want to thank my family and friends in Finland and abroad for all the support.

Abstract in English

The research presented in this thesis characterizes statistical and dynamical aspects of dominant wind-generated surface gravity waves inferred from field observations in intermediate-to-deep water. Dominant waves are the most energetic waves in a sea state, and as such, understanding their behavior is important in both engineering and geophysical contexts. Large waves impart considerable impact forces on marine structures such as oil and gas platforms and offshore wind turbines, and these forces may multiply manyfold when waves break. Wave breaking in deep water, often referred to as whitecapping, is also a key, though incompletely understood, process regulating the transfer of momentum, gas and heat across the air-sea interface, and must thus be accurately parameterized in large-scale weather and climate models. Current theory holds that the wave breaking process is closely linked kinematically and dynamically to the group structure inherent in ocean surface wave fields. Wave group dynamics is also believed to govern the characteristic shape and motion of so-called extreme or rogue waves, whose correct statistical description is central to many offshore activities.

The work presented herein shows, using state-of-the-art stereoscopic imaging techniques employed at the Ekofisk platform complex in the central North Sea, that large-scale wave breaking activity in the open ocean is strongly enhanced in dominant wave groups. The topic of wave group-modulated wave breaking has received considerable attention in the past two decades from theoretical, numerical and laboratory perspectives; however, quantitative field studies of the phenomenon remain comparatively rare. The current results also support the general notion that the dominant waves in a given sea state regulate the breaking of shorter waves.

The statistics of extreme wave crest elevations is investigated using a novel long-term laser altimeter data set, also located at the Ekofisk field. The validity of the extreme values is verified using a newly developed despiking methodology, and the quality controlled data set, which covers storm events over an 18-year period, is used to investigate the effects of wave steepness and directionality on crest height statistics. Narrow directional spread combined with high wave steepness is found to lead to crest height statistics that

deviate the most from standard linear and second-order formulations.

Finally, geometric wave shape and crest speed dynamics are analyzed for the highest wave crests encountered in three-dimensional, spatially and temporally resolved segments of the stereo-reconstructed sea surface fields. The directly measured crest steepness is found to conform to the classical breaking limit of Stokes, whereas crest steepness estimated from one-dimensional time series measurements using the linear gravity-wave dispersion relation are systematically higher. This may be at least in part explained by the observation that the directly measured crest speed just before, during and after the moment of maximum crest elevation slows down compared to the linear gravity-wave phase speed estimate. For the first time, the crest speed slowdown is shown with field measurements to apply to both breaking and non-breaking dominant wave crests.

Abstract in Norwegian

Denne avhandlingen er basert på forskningsresultat som behandler statistiske og dynamiske egenskaper av dominante vinddrevne overflatebølger i åpent hav. Med uttrykket *dominante bølger* refererer vi her til de største bølgene, med størst energi, i en gitt sjøtilstand. Bølgedrevne prosesser er viktige både i klimasammenheng via atmosfære–hav interaksjon som drives i stor grad av bølgebrytning, samt for kommersiell og rekreasjonell offshorevirksomhet p.g.a. risikoen for å bli utsatt for f.eks. ekstreme enkeltbølger. Både bølgebrytning og ekstrembølgestatistikk er i skrivende stund ufullstendig representert i teoretiske og numeriske modeller. Arbeidet som presenteres i denne avhandlingen undersøker de ovennevnte temaene ved bruk av bølgeobservasjoner som er primært samlet inn på Ekofiskfeltet i den sentrale delen av Nordsjøen. Observasjonsdatasettene består av en langtidstidsserie av laser-altimetermålinger og stereoskopiske videodata fra Ekofisk, samt videomålinger av brytende bølger fra et forskningstokt i nordre Stillehavet.

Forskningsresultatene er presentert i artikkelform med to publiserte verk og ett innlevert manuskript. Det blir påvist en tydelig forbindelse mellom økt bølgebrytning og dominante bølgegrupper, et resultat som tidligere har blitt påvist i laboratorie- og modelleksperiment, men sjeldent ved bruk av feltobservasjoner. Tredimensjonale stereorekonstruksjoner viser også at ekstreme bølgekammer, både brytende og ikke-brytende, følger nylig utviklet teori om ikke-lineær bølgegruppedynamikk. Dette funnet har konsekvenser f.eks. for estimering av geometriske og kinematiske bølgeegenskaper såsom steilhet og kamhastighet fra endimensjonale tidsseriemålinger. Som følge av en langtidsanalyse av endimensjonal bølgestatistikk blir det vist at enrettet, langkammet og bratt sjø mest sannsynlig leder til ekstreme enkeltbølger med statistiske egenskaper som avviker systematisk fra ordinære statistiske modeller. Tredimensjonal, kortsiktig tid-rom-statistikk av ekstreme bølgekammer blir også undersøkt v.h.a. stereomålingene fra Ekofisk. Her blir det vist at statistiske modeller utvidet fra endimensjonale til tredimensjonale bølgefelt i snitt er velegnet til å beskrive forekomsten av de høyeste bølgekammene, spesielt for relativt store tid-rom segment.

List of publications

1. **Malila, M. P.**, P. Bohlinger, S. Støle-Hentschel, Ø Breivik, G. Hope and A. K. Magnusson, A Nonparametric, Data-Driven Approach to Despiking Ocean Surface Wave Time Series, *Journal of Atmospheric and Oceanic Technology* **39**, 1, doi:10.1175/JTECH-D-21-0067.1, 2022.

2. **Malila, M. P.**, J. Thomson, Ø. Breivik, A. Benetazzo, B. Scanlon, and B. Ward, On the groupiness and intermittency of oceanic whitecaps, *Journal of Geophysical Research: Oceans* **127**, 1, doi:10.1029/2021JC017938, 2022.

3. **Malila, M. P.**, F. Barbariol, A. Benetazzo, Ø Breivik, A. K. Magnusson, J. Thomson and B. Ward, Statistical and dynamical characteristics of extreme wave crests assessed with field measurements from the North Sea, under review for *Journal of Physical Oceanography*.

Contents

Chapter 1

Introduction

1.1 Motivation

Surface gravity waves generated by the wind cover the world's oceans and are central to a host of phenomena of interest in engineering, geophysical and even recreational contexts. From an engineering and shipping perspective, large waves pose a safety hazard to personnel, operations and equipment, especially if their size exceeds the expectations for given environmental conditions. Tales of the sudden appearance of single waves (or, at times, groups of waves) much higher than the surrounding waves abound in historical oceangoing accounts [see, e.g., Olagnon, 2017]. However, direct evidence of such extreme waves—sometimes, especially in popular reports, called *rogue* or *freak* waves—has only started to emerge in the past three decades as wave observations at offshore oil platforms and other monitoring stations have become more widespread [Dysthe et al., 2008; Haver, 2004].

Because extraordinarily large waves are by definition rare, the validity of existing statistical models based on empirical data becomes increasingly uncertain as one approaches the poorly sampled tails of wave and crest height distributions [Adcock and Taylor, 2014; Dysthe et al., 2008]. This is especially true in severe storm conditions, during which wave fields become exceedingly nonlinear and, potentially, susceptible to height-amplifying effects due to increased wave steepness [Janssen, 2003; Mori and Janssen, 2006]. Moreover, wave and crest height measurements are traditionally obtained at a single point on the sea surface using wave buoys or probe-like instruments. Recent research, based on novel measuring techniques, indicates that neglecting the spatial dimension in realistic, directionally spread and short-crested wave fields may lead to a significant underestimation of the maximum expected wave amplitude encountered over a finite-sized patch of the

ocean surface [Benetazzo et al., 2015; Fedele, 2012].

As waves grow steep they begin to break, as evidenced by the increased abundance of whitecaps, coherent conglomerations of air bubbles, visible on water surfaces with increasing wind speed. Besides multiplying the forces imparted on structures, large-scale wave breaking also impacts the height distributions of large waves [see, e.g., Donelan and Magnusson, 2005; Karmpadakis et al., 2019; Latheef and Swan, 2013]. Furthermore, wave breaking in deep water drives many geophysically significant processes at the air-sea interface, including gas exchange [Deike and Melville, 2018; Woolf, 1997], mass and momentum transfer [Deike, 2022; Gemmrich et al., 2008; Melville, 1996], sea spray production [De Leeuw et al., 2011] and turbulent mixing [Agrawal et al., 1992; Gemmrich and Farmer, 2004; Thomson et al., 2016]. Advancing our understanding of the energy-dissipating processes related to wave breaking is also important for the further development of numerical wave prediction models, which provide important information about the sea state to beachgoers and ship captains alike [e.g., Ardhuin et al., 2010; Komen et al., 1994]. Increasingly, numerical wave models are also starting to be coupled to ocean, weather and climate models in order to better parameterize the small-scale, wave-driven exchange processes that occur at the air-sea interface [Ali et al., 2019; Belcher et al., 2012; Cavaleri et al., 2012; Li et al., 2019].

Obtaining open-ocean wave measurements in the full range of possible sea states is challenging both because of the remoteness of the environment and the risks involved in deploying and recovering instruments, especially in strongly forced conditions [Sullivan and McWilliams, 2010]. For this reason, *in-situ* instruments installed on, e.g., offshore platforms provide unique data sets from conditions in which direct human involvement would be irresponsible or impractical. For the past few decades, platform-based instruments and offshore wave buoys have provided valuable data on wave and crest height statistics [Christou and Ewans, 2014; Forristall et al., 2004; Gibson et al., 2014; Häfner et al., 2021b]. More recently, stereo camera-based wave sensing systems are becoming increasingly popular additions to offshore platforms thanks to their relatively inexpensive equipment requirements [Benetazzo, 2006; Benetazzo et al., 2012; Bergamasco et al., 2017; Vieira et al., 2020]. One consequence stemming from the vast amounts of scientific data collected on offshore platforms is that robust quality control becomes demanding on both computational and human resources [Cattrell et al., 2018; Häfner et al., 2021a]. This aspect is especially important in extreme event (e.g., rogue wave) analyses, where the validity of observed extreme data points is critical [Dysthe et al., 2008].

1.2 Objectives

The research presented herein is aimed at analyzing the prevalence and behavior of dominant sea surface waves in an open-ocean field setting. The observational techniques used are mainly based on non-intrusive, close-range remote sensing instrumentation installed on the Ekofisk offshore platform in the central North Sea. While the experimental data are largely focused geographically on the North Sea region, the exposed offshore environment gives the results global relevance. The data sets employed range from long-term, high-frequency point measurements, which allow us to study the statistical characteristics of extreme wave crest heights, to spatially and temporally phase-resolving stereo video measurements, which lend themselves to investigating in detail dynamical processes such as wave breaking and crest speed kinematics as well as the space-time statistical properties of extreme wave crests.

The scientific results are presented in two scientific publications and one manuscript under review, referred to hereafter as Papers I–III. The central objectives of the papers are summarized below.

- Paper I introduces a novel wave-signal despiking methodology targeted at robust noise detection and differentiation between artificial measurement errors and genuine extreme wave measurements.
- Paper II is a field study comprising measurements from the North Sea and the north Pacific Ocean, investigating the manner in which wave breaking is modulated by wave groups.
- Paper III combines long-term crest height statistics from a newly quality-controlled set of laser altimeter measurements with co-located stereo video measurements from selected storm events to investigate the effects of wave steepness and directionality on crest height statistics and crest speed kinematics.

1.3 Structure

The remainder of this thesis is structured as follows. Relevant theoretical concepts are reviewed in Chapter 2, and the observational data sets and instrumentation are described in Chapter 3. Chapter 4 summarizes the papers (Papers I–III) that constitute the main body of work in the thesis, and Chapter 5 provides concluding remarks regarding the main takeaways and discusses possible future avenues of applying and extending the work presented herein. Finally, the full texts of Papers I–III are appended in Chapter 6.

Chapter 2

Scientific background

2.1 Random waves and the wave spectrum

Perhaps the most conspicuous feature of the water surface in any large body of water, such as the open ocean or a large lake, is the presence of waves of varying size, ranging from small ripples to larger waves up to several hundred meters in length depending on the environmental conditions. These waves are generated by the wind [Miles, 1957; Phillips, 1957] and driven to oscillate about the mean sea level by the restoring force of gravity, as opposed to other, larger-scale gravity wave phenomena such as tides, tsunamis or infra-gravity waves which have different generating mechanisms [see, e.g., Kinsman, 1965]. The wind-generated surface gravity waves, or just surface waves for short, are seemingly irregular in terms of their amplitude and phase, which makes it a natural choice to represent the wave field in a stochastic manner. To a reasonable approximation, the sea surface can be modeled as a linear combination of statistically independent (and therefore uncorrelated), sinusoidal wave components. In mathematical terms, this can be expressed as [see, e.g., Holthuijsen, 2007]

$$\eta(x,\, y,\, t) = \sum_{m=1}^{M} \sum_{n=1}^{N} a_{m,n} \cos\left(\omega_m\, t - k_m\, x\, \cos\left(\theta_n\right) - k_m\, y\, \sin\left(\theta_n\right) + \phi_{m,n}\right), \tag{2.1}$$

where sea-surface elevation $\eta(x,\, y,\, t)$ is a sum of discrete wave components defined by their radian frequency ω and wavenumber vector $\mathbf{k} = (k\cos(\theta), k\sin(\theta))$, where θ indicates the wave propagation direction. The wave amplitudes a and phases ϕ are stochastic (i.e., random) variables. Assuming that the sea surface elevation η forms a zero-mean Gaussian process, the amplitudes a were shown by Longuet-Higgins [1952] to follow the Rayleigh distribution [Rayleigh, 1880]. The phases, on the other hand, are generally

assumed to be uniformly distributed between 0 and 2π.

In the linear (i.e., Gaussian) model, for arbitrary water depth d, there exists a unique relationship between the wave frequency ω and wavenumber magnitude $k = |\mathbf{k}|$ given by the *dispersion relation*,

$$\omega^2 = gk \tanh(kd), \tag{2.2}$$

where $g = 9.81\,\mathrm{m\,s^{-2}}$ is the gravitational acceleration. In the shallow-water limit, where the wavelength $L = 2\pi/k$ is much greater than the water depth, kd tends to zero and $\omega \approx k\sqrt{gd}$. This implies that the phase speed $c = \omega/k$ in shallow water is independent of the wavenumber; i.e., shallow-water waves are non-dispersive. Conversely, in deep water where $kd \to \infty$, the dispersion relation can be approximated as $\omega \approx \sqrt{gk}$; i.e., deep-water waves are dispersive. This means that the wave phase speed is dictated by the wavelength, with long waves (low k) travelling faster than shorter waves (higher k).

The total energy of a wave field is given as $E_{\mathrm{tot}} = \rho g \eta^2$, where ρ is the water density. Consequently, the wave energy is proportional to the variance of the wave amplitudes, $E_{\mathrm{tot}} \sim \mathrm{E}\{a^2/2\}$. Here, $\mathrm{E}\{\cdot\}$ is the expected value operator for stochastic variables. The energy content of a stochastic wave field $\eta(x,\, y,\, t)$ is therefore commonly represented with the variance density spectrum $E(\omega,\, \theta)$, defined for vanishing increments in frequency and direction $\Delta\omega$ and $\Delta\theta$ as [Holthuijsen, 2007]

$$E(\omega,\, \theta) = \lim_{\Delta\omega \to 0} \lim_{\Delta\theta \to 0} \frac{1}{\Delta\omega\, \Delta\theta}\, \mathrm{E}\{\frac{1}{2} a^2\}. \tag{2.3}$$

Formally, the variance density spectrum (often referred to simply as the *wave spectrum* for short) is defined as the Fourier transform of the sea surface auto-covariance function $C(\tau) = \mathrm{E}\{\eta(t),\, \eta(t+\tau)\}$, shown here for the one-dimensional case with $\eta = \eta(t)$,

$$E(f) = 2 \int_{-\infty}^{\infty} C(\tau) \cos(2\pi f \tau)\, \mathrm{d}\tau, \tag{2.4}$$

where $f = \omega/2\pi$ is the wave frequency in units of Hz. The formal definition in Eq. (2.4) requires stationarity of the stochastic process $\eta(t)$, in the sense that its auto-covariance C must depend only on the time difference τ. As a consequence, real-world wave energy spectra are generally estimated by applying power spectral analysis [Welch, 1967] on time series measurements of the sea surface elevation $\eta(t)$, often also called wave records, collected over short-enough periods such that sufficient stationarity of the environmental conditions can be assumed. In practice, the standard duration of a wave record is approximately 20 minutes.

Despite the fact that the real sea surface is neither strictly linear nor stationary, the

wave energy spectrum is, nonetheless, widely used for describing the wave field (i.e., the sea state) in practical applications. Many characteristic sea state parameters can be approximated from the moments of the wave spectrum,

$$m_i = \int_0^\infty f^i E(f)\,\mathrm{d}f. \tag{2.5}$$

For example, the most common measure of the predominant wave height in a given sea state is the significant wave height H_s, defined as the mean of the highest one-third of a sorted sequence of crest-to-trough wave heights in a wave record. If the wave spectrum is narrow-banded in frequency, H_s is very closely approximated by

$$H_\mathrm{s} \approx 4\sqrt{m_0}, \tag{2.6}$$

where the zeroth-order spectral moment m_0 is equal to the variance of the wave amplitudes. Due to the finite frequency bandwidth and weak nonlinearity of realistic wave fields, H_s estimated from an empirical wave spectrum typically overestimates the value obtained from an ordered list of wave heights by 5–10% [Longuet-Higgins, 1980].

2.1.1 The shape and evolution of the wave spectrum

To leading order, the wave energy content in a given sea state is determined by the strength, duration and spatial distance (also known as *fetch*) covered by the wind that generated the wave field. The combination of these factors leads the wave spectrum to evolve over time. The evolution of the wave spectrum in deep water can be expressed with the energy balance equation [e.g., Komen et al., 1994]

$$\frac{\mathrm{d}E(f)}{\mathrm{d}t} = S_\mathrm{in} + S_\mathrm{ds} + S_\mathrm{nl}, \tag{2.7}$$

where the left hand side is the material derivative of the time evolution and advection of the wave energy by the group velocity $c_\mathrm{g} = \partial\omega/\partial k$, and the right-hand side contains the main source terms affecting the shape of the wave spectrum. The first term on the right-hand side, S_in, represents the energy input by the wind, the middle term, S_ds, the dissipation of wave energy by wave breaking and the last term, S_nl, represents nonlinear four-wave resonant interactions which redistribute wave energy between wave components in the wave spectrum [Hasselmann, 1962; Phillips, 1977].

Figure 2.1 uses a sample storm event, the Andrea storm of Nov 2007 [Donelan and Magnusson, 2017; Magnusson and Donelan, 2013; Malila et al., 2022a], to illustrate the evolution of the wave spectrum at different stages of the storm. Four points in time are

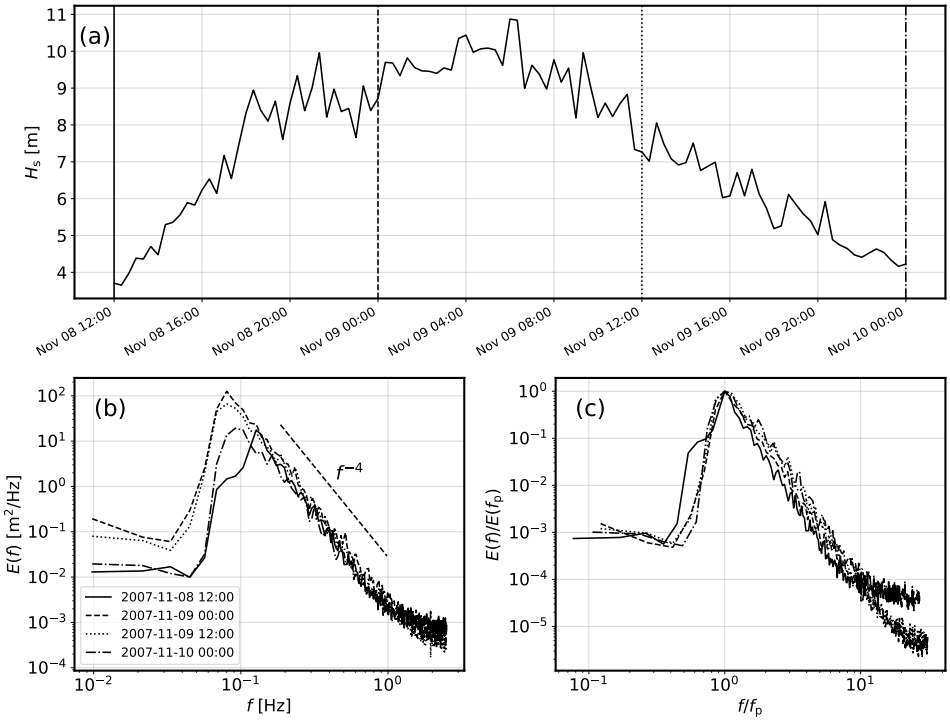

Figure 2.1: (a) The evolution of H_s during the Andrea storm on Nov 8–10 2007 as recorded by a laser altimeter on the Ekofisk platform. (b) Scalar variance density wave spectra $E(f)$ at four selected points in time during the storm. The dashed line shows the f^{-4} theoretical spectral tail slope. (c) The spectra from (b), with frequencies f normalized by the peak frequency f_p and variance densities $E(f)$ normalized by the variance density at the peak frequency $E(f_p)$.

picked in the early stages of the storm (solid lines), near the peak of the storm (dashed lines), during the decay stage of the storm (dotted lines) and in the late stages of the storm (dash-dotted lines). As displayed by Figure 2.1(b), the peak frequency of the wave spectrum starts out at roughly $f_p = 0.13$ at 12:00 on Nov 8, drops down to $f_p = 0.08$ at 00:00 and 12:00 on Nov 9, before increasing somewhat to $f_p = 0.09$ at 00:00 on Nov 10. This down-shifting of the peak frequency (or, equivalently, the growth of the peak wave period $T_p = 1/f_p$) happens due to the nonlinear wave-wave energy transfer by the S_{nl} term in Eq. (2.7), which predominantly reshuffles the energy from high frequencies to low frequencies as the storm progresses. At the end stage of the storm, once the wind input has significantly decreased and H_s is back down to its value at the beginning of roughly 4 m, we see from Figure 2.1(b) that the peak frequency remains at a much lower level than during the storm's early stages. This reflects the change of the sea state from a developing, *windsea*-dominated sea state to a more mature sea state with a larger *swell*

component. Swell refers to long-period wave components which travel faster than the wind, and which are therefore not affected directly by the energy input by the wind.

While the majority of the wave energy is transferred towards lower frequencies (i.e., large scales) by nonlinear interactions, a smaller fraction of the energy is also transferred to higher frequencies (i.e., smaller wave scales). At mid-to-high frequencies, the wave energy is ultimately dissipated by wave breaking. Wave breaking in deep water (i.e., unaffected by depth-induced shoaling) is also commonly called *whitecapping*. The normalized wave spectra in Figure 2.1(c) suggest that there exists a similarity scaling law for the shape of the spectrum at these high frequencies. That is, while the integrated total energy of the spectrum (i.e., the variance m_0) may change, the spectral profile remains approximately similar. Following Phillips [1958] and Phillips [1985], the high-frequency tail of a windsea spectrum is commonly referred to as the *equilibrium range*. In the equilibrium range, the source terms for wind input, dissipation and nonlinear interactions are balanced, leading to the universal power-law decay visible in the tails of the spectra in Figure 2.1.

Initially, Phillips [1958] argued on dimensional grounds, excluding the effects of wind, viscosity and surface tension, that the slope of the frequency spectrum in the equilibrium range should be proportional to f^{-5}. The assumption behind this relation was that wave amplitudes at scales smaller than the spectral peak are constrained by wave breaking, which occurs when the local crest acceleration exceeds a certain fraction of the gravitational acceleration g. In essence, Phillips [1958] assumed that the spectral density is saturated at high frequencies, such that any excess spectral density at high frequencies is immediately dissipated by breaking. However, the Phillips [1958] formulation does not explicitly account for the effects on spectral shape due to nonlinear wave-wave interactions. Later, Phillips revised his formulation of the expected power law behavior of the high-frequency spectral tail to be proportional to f^{-4} [Phillips, 1985]. The revised formulation was based on an assumed balance and approximately equal magnitude of all three source terms in Eq. (2.7), and was found to better represent the shapes of measured open ocean spectra. As highlighted by Kitaigordskii et al. [1975], dimensional analysis can be strictly applied only to spectra represented in wavenumber space; therefore, the spectral power laws given in terms of frequency f are necessarily approximations based on an assumption of the validity of the dispersion relation. The equilibrium and saturation ranges in wavenumber space correspond to spectral slopes of $k^{-2/5}$ and k^{-3}, respectively. However, because most wave spectra are estimated from sea surface elevation time series, the frequency domain representation is the most widely used in observational wave spectral analysis.

At present, it is widely accepted that the tails of real-world windsea spectra exhibit both an equilibrium range with decay proportional to f^{-4}, as well as a saturation range

proportional to f^{-5} [Banner, 1990; Kahma and Calkoen, 1992; Lenain and Melville, 2017]. Recent results indicate that these ranges are present even in swell-dominated wave spectra [Vincent et al., 2019]. The transition from the equilibrium range to the saturation range is believed to occur rather abruptly at a high threshold frequency corresponding to an as of yet uncertain multiple of the spectral peak frequency [Björkqvist et al., 2019; Lenain and Melville, 2017].

The power-law shape of the spectral tail is used in the work presented herein mainly to validate the quality control methodology introduced in Paper I [Malila et al., 2022a]. In this study, we compare the tails of wave spectra estimated from noise-corrupted raw signals of four effectively co-located (spaced in a 2.6-m^2 array) laser altimeters (see Section 3.2.1) before and after a novel quality control (QC) procedure. The paper shows that the power-law shape of the spectral tail is robustly recovered by applying the QC procedure.

2.1.2 Parametric spectra

A number of large-scale field experiments have been devoted to measuring the shapes of wave spectra in varying environmental conditions with the aim of defining a self-similar spectral profile applicable to a wide range of situations. Pierson and Moskowitz [1964] estimated an ideal spectral shape for *fully developed* sea states, in which the wind has blown over an effectively infinite fetch for long enough such that the wave field is in a state of equilibrium in terms of wind input and wave breaking. The tail of the idealized Pierson-Moskowitz spectrum is set to follow the f^{-5} power law of Phillips [1958].

The most widespread spectral shape for *developing* sea states is based on the Joint North Sea Wave Project (JONSWAP) experiment [Hasselmann et al., 1973]. The JONSWAP spectrum builds on the Pierson-Moskowitz spectral shape by adding a peak enhancement term, which accounts for the *peakedness* of the spectrum. The spectral peakedness, essentially the inverse of the spectral width, is known to be related to the group structure of the wave field, which arises due to the amplitude and frequency modulation inherent in random, dispersive deep-water waves [e.g., Kimura, 1980]. A narrow, peaked spectrum is generally associated with longer, more pronounced wave groups [Goda, 1978; Longuet-Higgins, 1975].

2.2 Nonlinear waves

While the Gaussian model introduced above provides a reasonable first-order description of wave properties, real ocean surface waves are in general nonlinear. In physical terms, wave nonlinearity is represented by the processes on the right-hand side of Eq. (2.7), that is, dissipative processes such as wave breaking, wave growth by wind forcing, and nonlinear energy transfer between wave components. Mathematically, nonlinearity manifests as the breakdown of the assumption of statistical independence, and, consequently, the breakdown of the Gaussian model [e.g., Trulsen, 2006].

The linear, Gaussian theory of wave mechanics builds on the constraint that wave steepness (i.e., the wave slope) is very low, that is, the wave length is much longer than the wave amplitude. The dimensionless wave steepness, ϵ, is therefore commonly expressed as the product of the wave amplitude and the wavenumber (i.e., the inverse wavelength),

$$\epsilon = ak. \tag{2.8}$$

As the wave steepness grows larger, nonlinear effects become more prevalent. The elementary theory of nonlinear surface gravity waves was developed by Stokes [1847], whose model of the sea-surface elevation η is based on a perturbation expansion in terms of ϵ. The Stokes wave can, therefore, be written in terms of so-called *Stokes corrections* of increasing order in steepness,

$$\eta(x,t) = \epsilon\eta_1(x,t) + \epsilon^2\eta_2(x,t) + \epsilon^3\eta_3(x,t) + ..., \tag{2.9}$$

where $\eta_1(x,t) = k^{-1}\cos(\omega t - kx)$ is the linear harmonic wave component, and higher-order corrections follow from nonlinear equations of motion and boundary conditions expanded to higher order in ϵ [see, e.g., Holthuijsen, 2007, p. 140]. The second-order Stokes wave can be approximated in deep water as [see, e.g., Lamb, 1932]

$$\eta(x,t) = a\Big(\cos(\omega t - kx) + \frac{1}{2}ka\cos[2(\omega t - kx)]\Big). \tag{2.10}$$

The corresponding, second-order, deep-water dispersion relation is given by

$$\omega^2 = gk\Big(1 + \frac{1}{2}a^2k^2\Big). \tag{2.11}$$

The Stokes corrections (to any order in ϵ) are so-called *bound harmonics*, which implies that their phase speeds correspond to the phase speed of the first (linear) harmonic. The most noticeable effect of the Stokes corrections is a modification of the wave profile. The crests of Stokes waves are somewhat sharper and higher than linear crests, and the

troughs are somewhat flatter and shallower than linear troughs. It has been shown by Longuet-Higgins [1963] (for deep water) and Sharma and Dean [1981] (for intermediate water depth) that the interaction of an arbitrary number of second-order Stokes waves can be expressed by positive and negative interaction terms. The positive interactions occur due to the superposition of interacting, phase-locked wave components, and lead to the aforementioned wave profile modification. The negative interactions are related to the difference in frequency between interacting wave components, and are responsible for a slow modulation of the water level that manifests as a setdown under large wave groups.

Uniform Stokes waves are known to be susceptible to resonant interactions due to small perturbations in the wave form, which, under certain conditions rarely encountered in the ocean (including a narrow spectrum combined with steep, long-crested waves), may lead to an energy-focusing instability mechanism [Benjamin and Feir, 1967; Lighthill, 1965; Trulsen and Dysthe, 1996; Zakharov and Ostrovsky, 2009]. This instability, often called *modulational instability* or Benjamin–Feir instability, has been proposed as a mechanism responsible for wave breaking [Melville, 1982], and also for the generation of wave crests of extreme amplitude in the ocean [Dysthe et al., 2008; Janssen, 2003]. The mathematical treatment of high-order nonlinear wave phenomena is outside of the scope of the present thesis; however, the practical applicability of these high-order theories to real-world wave fields is discussed in Section 2.2.2 as well as in Paper III of this thesis [Malila et al., 2022, under review]

2.2.1 Wave breaking

The strongly nonlinear phenomenon of wave breaking is the dominant sink of wave energy, and comprises the largest contribution to the dissipation source term in the energy balance equation of Eq. (2.7) [Ardhuin et al., 2010; Komen et al., 1994]. The dynamical description of wave breaking is a complex hydrodynamical problem, and remains the topic of active ongoing research [e.g., Barthelemy et al., 2018; Craciunescu and Christou, 2020; Derakhti et al., 2020; Pizzo and Melville, 2019; Stringari et al., 2021].

Breaking onset and its relation to wave groups

The onset of wave breaking can be described from geometric, kinematic and dynamic perspectives [e.g., Perlin et al., 2013]. The underlying principle behind all descriptions is that the particle velocity at the wave crest exceeds the phase speed of the wave [Stokes, 1880]. In geometric terms, it can be shown that the profile of an idealized (i.e., stationary

and one-dimensional) Stokes wave in deep water becomes unstable and disintegrates (i.e., breaks) when the crest forms a 120° angle, corresponding to a local steepness value of $\epsilon = 0.443$ [Michell, 1893]. The breaking-constrained wave steepness limit was later extended to intermediate water depth by Miche [1944]. While a number of studies have found that breaking regularly starts at much lower bulk wave steepness than that implied by the Stokes and Miche limits [Banner and Peirson, 2007; Holthuijsen and Herbers, 1986], the validity of the Stokes breaking-limited profile in the immediate vicinity of incipient breaking crests has been verified with open-ocean stereo video measurements by Schwendeman and Thomson [2017].

The kinematic breaking criterion is generally described as the aforementioned point at which the horizontal velocity of a particle at the wave crest exceeds the phase speed of the wave, leading to wave-crest overturning. The observational verification of the kinematic criterion, especially in field conditions, is complicated by the difficulty of measuring the particle velocity and ambiguities in defining the phase speed in broad-banded and directionally spread wave fields [Perlin et al., 2013].

Finally, the classical dynamic breaking criterion states that wave profile overturning commences when the downward acceleration of the water surface on the front face of a wave crest exceeds a threshold level [e.g., Babanin, 2011]. Recent research has focused on dynamical breaking criteria based on the local rate of wave energy convergence [Banner and Peirson, 2007; Barthelemy et al., 2018; Derakhti et al., 2020; Saket et al., 2017; Song and Banner, 2002]. Wave group dynamics is also believed to play a key role in the onset of wave breaking. First observed by Donelan et al. [1972], the amplitude modulation experienced by wave crests as they propagate through a wave group envelope naturally steepens the crests periodically, pushing their profile closer to the limiting geometry. Similarly, the long-wave modulation of shorter wave components is known to impact the breaking onset of short waves at scales (i.e., frequencies and wavenumbers) above the spectral peak [Dulov et al., 2002; Longuet-Higgins and Stewart, 1960]. In the recently developed wave breaking framework of Barthelemy et al. [2018], the wave crest profile disintegrates as a consequence of intra-group energy focusing. Formally, their wave-crest breaking criterion depends on the ratio of the local energy flux to the local energy density normalized by the crest propagation velocity.

Real-world, dispersive and nonlinear temporally evolving wave groups are governed by complex kinematic and dynamic behavior, as initially described by Banner et al. [2014]. Compared to steady (i.e., non-evolving) wave crests which have constant phase speed, wave crests in unsteady wave groups tend to slow down as they grow in amplitude and steepness, followed by an acceleration as they progress past the maximum group envelope (i.e., wave-group *focus*). This behavior is in contrast to the steady nonlinear

theory of Stokes [1847], which predicts an increase of the phase speed with growing steepness. The crest speed kinematics of realistic wave groups are a key factor in wave breaking onset through the kinematic breaking criterion, as well as in the breaking crest length distribution framework of Phillips [1985]. Field observations of the crest speed slowdown are still relatively rare; however, existing studies have found comparatively similar results of focused wave crests momentarily slowing down roughly 20% from the linear phase speed estimate [Banner et al., 2014; Fedele et al., 2020; Schwendeman and Thomson, 2017, see also Paper III of this thesis].

Field measurements of wave breaking

Large-scale wave breaking events in the open ocean are easily identified visually by the formation of foamy patches of air bubbles called whitecaps.[1] Photographing the sea surface from above and separating the brightly-colored whitecap features from the darker unbroken background thus readily allows for the estimation of the fraction of the visible area that is covered by whitecap foam [Callaghan and White, 2009; Kleiss and Melville, 2011; Scanlon and Ward, 2013]. This quantity is known as the *whitecap coverage*, and is typically denoted by W [Monahan, 1971]. Thanks to the relatively straightforward means of acquisition, the whitecap coverage is a commonly used proxy for quantifying momentum, gas and heat exchange processes at the air-sea interface [Brumer et al., 2017; Callaghan et al., 2008; Kleiss and Melville, 2010; Scanlon and Ward, 2016; Schwendeman and Thomson, 2015]. The detection of whitecaps in optical imagery is also central in estimating breaking crest speed distributions in the wave breaking dissipation framework introduced by Phillips [1985].

Most commonly, the whitecap coverage is related to the wind speed U_{10}, measured or estimated at 10-m height above the sea surface, through a power-law relation [Monahan and Muircheartaigh, 1980], above a threshold wind speed. According to the reviews of historical whitecap coverage data sets provided by Anguelova and Webster [2006], Schwendeman et al. [2014] and Brumer et al. [2017], the most common $W(U_{10})$ parameterizations either use a tunable power-law coefficient or assume a cubic relation between the parameters.

The work presented in this thesis addresses the topic of wave group-induced modulation of wave breaking through field measurements of the whitecap coverage combined with coherent measurements of the sea-surface elevation from the Ekofisk stereo video data set (Paper II). Moreover, the crest speed dynamics of breaking and non-breaking focused

[1] Very small-scale *micro-breakers* do not entrain air bubbles, and thus do not create an optically discernible signal [Jessup et al., 1997; Sutherland and Melville, 2013].

wave groups is investigated, also with the Ekofisk stereo video data, in Paper III. Paper III also investigates the validity of the geometric steepness limits of Stokes and Miche on extreme wave elevations using the long-term Ekofisk LASAR data set.

2.2.2 Extreme waves and wave statistics

Waves much taller than the characteristic height of the surrounding wave field, typically quantified by H_s, are commonly referred to as *extreme waves*. In the scientific literature, the term *rogue wave* is generally applied to waves whose measured crest height C or trough-to-crest height H exceeds some predefined multiple of H_s. The most common rogue crest and rogue wave thresholds are [Dysthe et al., 2008]

$$C = 1.25H_s \quad \text{and} \quad H = 2H_s. \tag{2.12}$$

While the thresholds given in Eq. (2.12) are essentially arbitrary, they represent relatively rare events. For instance, assuming one-dimensional, linear waves distributed according to the Rayleigh distribution (see Section 2.1), a rogue wave twice the height of the significant wave height would occur approximately once for every 10,000 waves [Dysthe et al., 2008]. The statistics of large waves and crests change mainly as a result of two factors: increasing wave steepness (i.e., nonlinearity) and increasing wave-field dimensionality (e.g., extending point time series measurements to space-time) [e.g., Fedele et al., 2013]. Below, the relevant theory of extreme wave statistics is summarized, first in terms of classical point statistics and, subsequently, according to more recent theory on space-time statistics. More detailed reviews of these topics can be found in Paper III, as well as in the references mentioned herein.

Point statistics

At the time of writing, common means of measuring waves include wave buoys, wave staffs or range-measuring devices, all of which provide a one-dimensional time series measurement of a single point in the ocean (see Section 2.3.1). The statistical distribution of 1D random, linear wave and crest heights can be shown to follow the so-called Rayleigh distribution [Longuet-Higgins, 1952]. However, it is widely acknowledged that the linear approach underestimates the heights of the largest wave crests in storm conditions characterized by waves of finite steepness [e.g., Dysthe et al., 2008].

Second-order bound-wave effects have been incorporated into crest height distributions by, notably, Tayfun [1980] and Forristall [2000]. While second-order effects generally

amplify crest elevations, the crest-to-trough wave heights are essentially unaffected by second-order effects [Tayfun and Fedele, 2007]. To second-order, the shapes of crest height distributions are modified from the linear distribution in proportion to the magnitude of the characteristic wave steepness. The Tayfun [1980] model uses the third centralized statistical moment, i.e., the skewness, to represent the wave steepness, while the Forristall [2000] model uses a spectral definition based on Eq. (2.8) together with the Ursell number, which represents the steepening of wave crests due to shallow-water effects. The existing second-order crest height distributions are based on numerical simulations due to the lack of a direct method of deriving the distributions theoretically. However, comparisons with field data generally support the applicability of second-order models in many typical storm sea states [Buchner et al., 2011; Gibson et al., 2014; Lian and Haver, 2015; Tayfun and Fedele, 2007, see also Paper III of this thesis]. It may be noted that crest height models based on third-order approximations have also been formulated in order to explain occasionally observed deviations from second-order theory [Fedele et al., 2017]. Moreover, Gemmrich and Cicon [2022] recently argue that the occurrence of very large waves which considerably exceed the rogue wave thresholds of Eq. (2.12) may be explained through fourth-order Stokes corrections.

Space-time statistics

Because of the short-crested, directionally spread nature of realistic sea-surface wave fields, the one-dimensional statistical approach is limited in its ability to fully describe wave-field characteristics over finite regions such as the areas covered by offshore platforms or large ships. The analysis of the joint spatial and temporal statistical properties of surface waves builds on the works of Adler [1981] and Piterbarg [1996] on multi-dimensional Gaussian fields. Space-time effects are in general believed to enhance the exceedance probabilities of large wave crests in regions of finite area, when compared against point estimates [Baxevani and Rychlik, 2006; Benetazzo et al., 2015, 2017, 2020; Fedele, 2012; Fedele et al., 2013; Krogstad et al., 2004]. This enhancement is due both to the geometric effect of including the often highly focused point of a wave crest maximum in the observable domain, as well as the higher likelihood of capturing an evolving wave group at its moment of spatial and temporal focus [see, e.g., Boccotti, 2000].

Wave and crest height distributions have been extended to account for three-dimensional space-time effects following the extreme value principles of Gumbel [1958] by Fedele [2012], for linear crest heights, and by Benetazzo et al. [2015], for second-order crest heights following Tayfun [1980]. Due to the asymptotic fitting of Gumbel-type distributions, the space-time maximum formulations are generally valid for relatively large (side lengths comparable to the dominant wavelength) areas [Benetazzo et al., 2021]. The the-

oretical space-time formulations are reviewed in more detail in Paper III of this thesis. Paper III also evaluates the validity of the linear and second-order extended crest height distributions using space-time resolving stereo video measurements collected at Ekofisk (see also Sections 2.3.2 and 3.2.2 of this thesis).

2.3 Wave measurement techniques

2.3.1 Time domain measurements

Ocean surface waves are traditionally observed by measuring the time evolution of the sea surface elevation at a fixed point. The most common instruments include wave buoys, wave staffs and range-measuring remote sensing instruments such as platform-mounted laser altimeters and radars [see, e.g., Holthuijsen, 2007]. Time series point measurements are routinely used for estimating bulk parameters such as the significant wave height H_s or the peak period T_p, both for monitoring and model validation purposes. Zero-crossing analysis also allows for the estimation of wave-by-wave metrics such as trough-to-crest wave height and crest height distributions. By choosing a time window that ensures wave-field stationarity, commonly taken as 20–30 minutes, a mean sea level can be estimated from the time series, and individual waves can be defined through the mean-zero crossings of the instantaneous sea-surface elevation. Although commonly used, the zero-crossing method does not provide a measure of the instantaneous wave height, because the wave trough and wave crest elevations are measured approximately one wave period apart in time. The crest height, which is simply the maximum elevation above the mean level recorded between two zero crossings, can in this sense be seen as a more intuitively conceptualized variable.

Different instrumentation may also return differing estimates of the mean sea level and crest elevations [see, e.g., Barstow et al., 2004]. Fixed probes and rangefinders provide so-called *Eulerian* measurements of the exact same point in space, where second-order Stokes nonlinearities materialize as the aforementioned asymmetric wave profiles. Surface-following, *Lagrangian* measurements such as freely drifting (i.e., untethered) wave buoys, on the other hand, spend a relatively longer time near the pointy wave crests and a shorter time at the flatter troughs, which leads to a higher estimate of the mean sea level. Because of this, bound-wave nonlinearities are nearly cancelled out in buoy records [Holthuijsen, 2007]. The sea-surface elevation can also be inferred from sub-surface pressure sensors, but this technique relies on converting the pressure measurements to elevation signals using the linear dispersion relation, which in essence

linearizes the signal [e.g., Forristall, 2000; Holthuijsen, 2007].

Besides providing amplitude estimates, one dimensional temporal wave signals are also frequently used to deduce geometric and kinematic wave properties such as steepness and crest/phase speed [Gemmrich and Thomson, 2017; Toffoli et al., 2010]. A limitation of this approach, discussed at length in Paper III of this thesis, is that the conversion from the time domain to the spatial domain necessitates the application of the dispersion relation (either the linear one or a higher-order approximation). If the wave crests indeed slow down, as predicted and shown by Banner et al. [2014] and others, this approach may introduce biases in the estimates of wave steepness and crest speeds.

2.3.2 Stereoscopic space-time measurements

The point time series representation provided by wave buoys and laser rangefinders provides only a limited description of the directionally spread, short crested nature of real-world surface wave fields. While the bulk directional properties of a wave field can be estimated from the rotational or translational motion of wave buoys [Herbers et al., 2012; Kuik et al., 1988], obtaining a phase-resolved representation of the spatial sea surface profile requires a different approach. In general, the reconstruction of wave fields in high spatial resolution relies on remote sensing techniques such as nautical radars [Støle-Hentschel et al., 2018], scanning LIDAR [Reineman et al., 2009] or polarimetric imaging [Zappa et al., 2008]. In recent years, techniques based on stereoscopic digital photography have increased in popularity thanks to their relatively inexpensive equipment requirements and the publication of open source image processing software aimed at wave imaging applications [Benetazzo, 2006; Benetazzo et al., 2012; Bergamasco et al., 2017; Schwendeman and Thomson, 2017; Vieira et al., 2020]. Stereo-reconstructed sea surface fields obtained from, e.g., offshore platforms or research vessels are typically of high spatial resolution, and therefore allow for the direct measurement of wave characteristics such as the steepness and crest speed without the need to invoke the dispersion relation [e.g., Schwendeman and Thomson, 2017].

Stereoscopic imaging is a well-established technique for reconstructing a three-dimensional structure from a pair of images taken from slightly different vantage points [Klette et al., 1998]. For static objects, a pair of stereo images may be obtained by moving a single camera around an object; however, the constant, rapid movement of the sea surface wave field requires an effectively instantaneous capture of the same scene with two synchronized cameras. Early efforts of applying stereo photography to the measurement of surface wave characteristics include the studies of Holthuijsen [1983] and Banner et al. [1989]. Due to limited image processing capacity at the time, these studies analyzed spa-

tial wave characteristics obtained from single (still) stereo snapshots of the sea surface. Modern digital video cameras and computer processing capacity enable the spatial reconstruction of sequences of stereo images acquired at high frame rate, thus resolving both the spatial and temporal evolution of the wave field in high resolution [Benetazzo, 2006]. Below, we provide a brief overview of the concepts behind space-time wave field reconstructions from digital stereo video images based largely on the textbook by Szeliski [2010].

The basic principle behind stereo reconstruction relies upon matching pixels between two overlapping stereo images, and using triangulation based on the known geometry of the stereo camera setup to infer the three-dimensional positions of the pixels in real-world coordinates. A pair of matched pixels in a stereo image pair are related via their *epipolar geometry*, as illustrated in Figure 2.2. The line segment from the optical center of the left camera $\boldsymbol{c}_L$ to a 3D point $\boldsymbol{p}$ within the field of view of both cameras appears merely as a point from the perspective of the left camera. The same line segment viewed from the right camera appears as the *epipolar line* $\boldsymbol{l}_R$. The same but mirrored geometry applies for the opposite perspective. The line connecting the two optical centers, known as the *baseline*, passes through the *epipoles* $\boldsymbol{e}_L$ and $\boldsymbol{e}_R$. In fact, all possible epipolar lines pass through the epipoles, leading to different *epipolar planes* for the projections of different points $\boldsymbol{p}$. As a consequence, the epipoles can be found by searching for the intersection of all epipolar lines.

Once known, the epipolar geometry of a stereo camera system greatly simplifies the search for matching pixels between a pair of stereo images. In practical applications, stereo image pairs are typically transformed such that the epipolar lines of both images lie parallel to the horizontal axes of the image (pixel) coordinate system (j, i). This transformation, known as image *rectification*, ensures that matching pixels between the two images are found on the same horizontal pixel rows. Formally, the mapping between pixel coordinates on an epipolar plane is given by the *epipolar constraint*,

$$\boldsymbol{x}_R^{\mathrm{T}} \mathbf{E} \boldsymbol{x}_L = 0, \tag{2.13}$$

where the superscript T stands for transpose and $\mathbf{E} = \boldsymbol{t} \times \mathbf{R}$ is the *essential matrix*, which is composed of the cross product of the 3×1 translation vector $\boldsymbol{t}$ and the 3×3 rotation matrix $\mathbf{R}$ relating the geometric composition of the stereo camera setup. This *extrinsic* geometry is generally estimated through an external calibration or feature-matching process (see Section 3.2.2).

The epipolar constraint, as described by Eq. (2.13), assumes that the line segments between the camera optical centers and 3D points $\boldsymbol{p}$ are projected onto the image plane

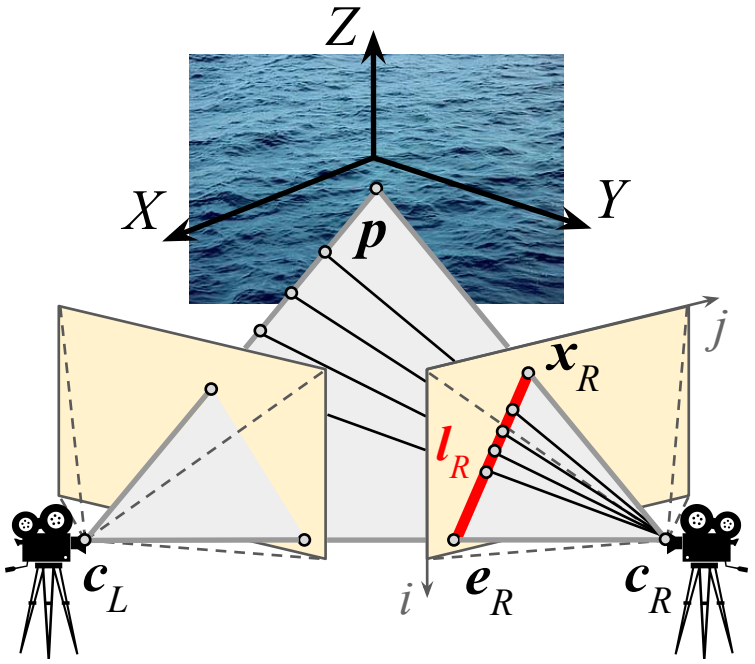

Figure 2.2: Schematic of the epipolar geometry of a stereo camera system. $\boldsymbol{c}_L$ and $\boldsymbol{c}_R$ are the optical centers (i.e., principal points) of the left and right cameras, respectively. (j, i) denote pixel coordinates on the camera image planes (only drawn on the right camera image plane), and (X, Y, Z) denote world coordinates. The line $\boldsymbol{c}_L$–$\boldsymbol{p}$ is seen as a point from the perspective of the left camera; the same line is seen as the epipolar line $\boldsymbol{l}_R$ (traversing between the epipole $\boldsymbol{e}_R$ and the point $\boldsymbol{x}_R$ on the right image plane) from the perspective of the right camera. The gray triangular plane illustrates the epipolar plane.

undistorted through an infinitesimal opening (i.e., aperture). This assumption forms the basis of the *pinhole camera model*. In practice, a modern digital camera consists of a charge-coupled device (CCD) sensor to register the arrangement of incoming photons as well as a lens to focus light rays onto the CCD sensor. In general, the configuration of the CCD sensor (representing the image plane) and lens are not perfectly aligned as assumed by the pinhole model. This configuration is described by the focal length and principal point, also collectively called the *intrinsic parameters*. The intrinsic parameters must be estimated for each separate camera–lens combination through an intrinsic calibration process (see also Section 3.2.2). The intrinsic calibration seeks to estimate the intrinsic matrix $\mathbf{K}$, defined as

$$\mathbf{K} = \begin{bmatrix} f_x & 0 & c_x \\ 0 & f_y & c_y \\ 0 & 0 & 1 \end{bmatrix}, \tag{2.14}$$

where f_x and f_y are measures of the *focal length* (i.e., the distance from the optical center to the image plane) in pixel units normalized by the pixel width and height, respectively, and c_x and c_y are the pixel coordinates of the principal point (i.e., the optical center). In a camera-centric coordinate system, the principal point is typically taken as the origin, while the focal length represents the distance from the optical center to the image plane.

In most real-world applications, the line segments (i.e., light rays) from a scene to the image plane pass through a camera lens instead of an infinitesimal pinhole. The lens introduces distortions to the projection of the pictured scene onto the image plane. One type of lens distortion causes straight lines to appear bent; this is commonly referred to as *radial distortion*. Another type of distortion due to the misalignment of the lens and the image plane is known as *tangential distortion*. Commonly used intrinsic calibration algorithms, therefore, typically also estimate coefficients to correct for the radial and tangential distortion (contained by the vectors $\boldsymbol{k}_\mathrm{r}$ and $\boldsymbol{k}_\mathrm{t}$) in the pixel coordinates [e.g., Heikkilä and Silvén, 1997].

Once the extrinsic geometry of the stereo camera setup is known through the essential matrix $\mathbf{E}$, and the intrinsic parameters of both stereo cameras have been estimated, the mapping between pixel coordinates of the image plane $[j, i]^\mathrm{T}$ (corrected for lens distortion) and world coordinates $\mathbf{X} = [X, Y, Z]^\mathrm{T}$ is given by

$$Z \begin{bmatrix} j \\ i \\ 1 \end{bmatrix} = \begin{bmatrix} f_x & 0 & c_x \\ 0 & f_y & c_y \\ 0 & 0 & 1 \end{bmatrix} \begin{bmatrix} 1 & 0 & 0 & 0 \\ 0 & 1 & 0 & 0 \\ 0 & 0 & 1 & 0 \end{bmatrix} \begin{bmatrix} \mathbf{R} & \mathbf{t} \\ \mathbf{0}_3^\mathrm{T} & 1 \end{bmatrix} \begin{bmatrix} X \\ Y \\ Z \\ 1 \end{bmatrix}. \tag{2.15}$$

Here, the last two terms describe the transformation between camera-centric and world coordinates. Thus, the geometric constraint implied by Eq. (2.15) can be used to triangulate the 3D positions of matching pixels detected in a pair of stereo images. The triangulation process is based on the *disparity* principle, which states that the 3D depth of a point is inversely proportional to the horizontal distance between matching points in pixel space (assuming rectified stereo images where matching pixels are found on horizontally aligned epipolar lines).

The 3D reconstruction of a scene from a pair of stereo images described above returns in essence a cloud of 3D positions for each matched pair of pixels. To infer useful wave-field characteristics from stereo images of the sea surface requires additional knowledge of the mean sea level about which the depicted wave field oscillates. Following Benetazzo [2006], the mean sea level can be estimated as the mean plane of a large number of sequential 3D point clouds (corresponding to at least 10 characteristic wave periods). The orientation of the mean plane can then be used to further rotate the point clouds

into Earth-referenced world coordinates in which the Z axis is aligned with the direction of the gravitational acceleration. This mean-plane estimation concept is also applied in the Waves Acquisition Stereo System (WASS) software [Bergamasco et al., 2017] used for stereo wave field reconstructions in the scientific analysis presented in the current thesis (see Section 3.2.2).

Chapter 3

Data and methods

3.1 Wave observations at the Ekofisk field – a historical perspective

The Ekofisk platform complex is the site of the earliest commercial oil extraction activity on the Norwegian continental shelf [Hanisch and Nerheim, 1992]. Oil exploration activities were launched by Phillips Petroleum (now ConocoPhillips), which was granted oil exploration commission to the area—known in technical terms as block number 2/4 in the Norwegian concession system—by the Norwegian government in the 1960s. The commercial extraction of oil was initiated in 1971 from a mobile platform named Gulftide. The first bottom-mounted platform (fixed to the seabed at approximately 70 m depth), the Ekofisk 2/4 A platform, was built shortly thereafter and began oil production in April 1974. A second fixed platform, Ekofisk 2/4 B, was built in 1972 several kilometers to the north of 2/4 A; production at 2/4 B commenced in October 1974. In 1987, an accompanying water injection and housing platform, 2/4 K, was built next to 2/4 B and connected to it with a footbridge. At the time of writing, the main Ekofisk platform complex is located 2.3 km south of the 2/4 B and 2/4 K platforms, which form the focus of the observational data sets in this thesis.

The exposed location of the Ekofisk field in the central North Sea puts high demands on the monitoring and forecasting of environmental conditions—especially strong winds and high waves—which may pose a danger to personnel and operations at the field. Early monitoring efforts from before the 1980s are poorly documented; however, the Norwegian Meteorological Institute archives contain environmental reports starting in January 1980. A sample wind and wave time series from a March 1980 report is shown in Figure 3.1. The wave measurements were made with a Datawell Waverider non-directional wave

buoy, and the wave model predictions were made with the first-generation NOWAMO numerical wave model, which simulated the energy content of the wave field based on wind information derived from digitized air pressure maps [Haug, 1968].

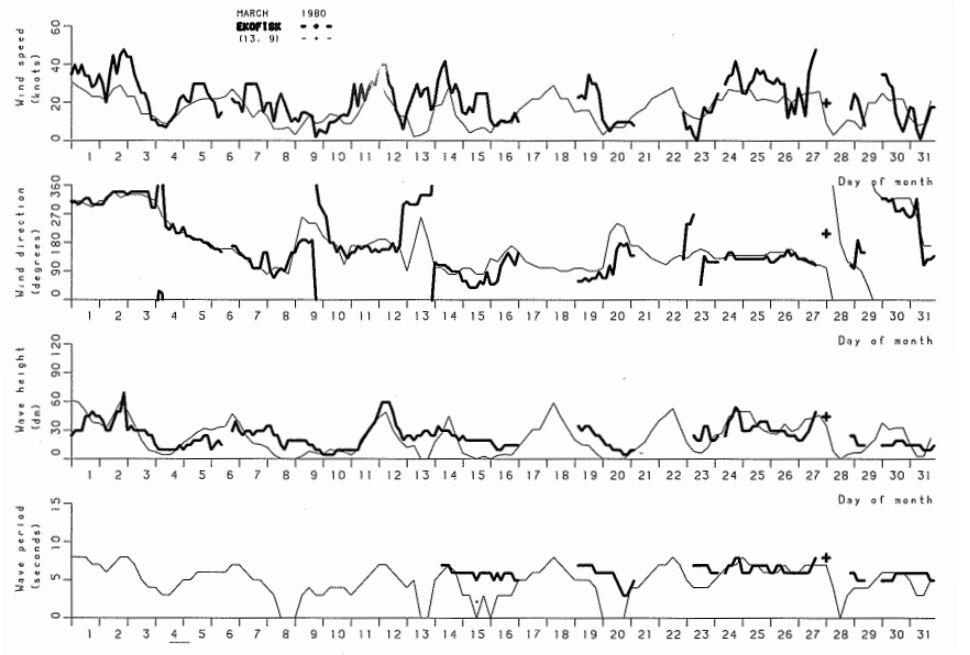

Figure 3.1: Monthly time series from March 1980 of wind speed [knots](top panel), wind direction [degrees, coming from] (second panel), wave height [dm] (third panel) and wave period [s] (bottom panel) at the Ekofisk platform, compiled by the Norwegian Meteorological Institute. The thick lines are observed values from a Datawell Waverider wave buoy, and thin lines are model predictions generated with the NOWAMO numerical wind and wave model.

The earliest archived environmental reports coincide historically with the March 27 1980 accident in which the *Alexander Kielland* housing platform in the Ekofisk field collapsed in heavy seas, resulting in 123 deaths. The platform collapse was determined to be caused by fatigue failure due to a weld defect in the supporting structure [Moan, 1985], and the prevailing 16–20 m/s winds and 6–8 m waves (see Figure 3.1) combined with cold water and air temperatures made the rescue efforts extremely challenging.[1]

In 1984, it was discovered that the seabed on which the platforms were mounted had subsided by as much as 4 m as a result of the oil extraction [Sulak, 1991]. To avoid damage by large waves overtopping the subsided structures, most platform legs were

[1] `https://www.ptil.no/en/technical-competence/explore-technical-subjects/features/2020/worst-that-can-happen/`; accessed on June 10 2022

raised by 6 m in a costly operation in 1986. Elevation of the 2/4 T storage and water treatment platform was deemed too costly and instead it was decided to build a 106-m high protective concrete wall (completed in 1989) around the platform. At the time of writing, the subsidence continues, albeit at a slower rate due to water injection, with the seabed level approximately 7 m below its original level in 1971.[2]

On December 12 1990, a severe storm hit the Ekofisk area. The maximum significant wave height (i.e., the average height of the highest one-third of the waves recorded) was measured by the Waverider buoy as 13.2 m [Magnusson et al., 2008]; to date, this is the highest value ever observed at Ekofisk. In the aftermath of the storm, which did not result in fatalities, the offshore industry expressed increased interest in robust observation systems and accurate forecasts of extreme sea states. In response, the Norwegian Meteorological Institute was commissioned to provide forecasts of the wave height in extreme sea states through the Ekofisk eXtreme Wave Warning (EXWW) project. Updated every 3 hours during storm events, the close-range wave height forecasts were aimed at allowing sufficient time for the evacuation of personnel from the platforms if faced with dangerously high sea states. The observational systems were also updated to allow for more reliable forecast validation, as documented by Magnusson et al. [2008]. Two pre-existing range-measuring altimeters were found to suffer from lee effects from the 2/4 T tank under northerly wave directions, and new Optech laser altimeters were installed in more exposed locations in 1995. An X-band marine radar was also installed on the helideck of the 2/4 K platform in 1995; this instrument has since been used to provide directional wave spectra through the commercial WaMoS systems [Reichert et al., 1999]. More recent instrument additions to the 2/4 K–B complex are described in Section 3.2 below.

3.2 Ekofisk wave data sets

The observational analysis presented in the papers included in this thesis (Papers I–III) is largely focused on two instruments located on the Ekofisk 2/4 K–B complex (Figure 3.2). These two instruments, the infrared laser array (LASAR) and the stereo camera system, are described in detail below. A third instrument, the X-band marine radar providing directional wave spectra through the WaMoS II system, located on the roof of the 2/4 K platform, has also been used for validation purposes, but does not constitute an integral part of the analysis. Paper II [Malila et al., 2022b] uses wind measurements from the 2/4 L platform in the main Ekofisk platform complex 2.3 km south of 2/4 K–B. Moreover, Paper III [Malila et al., under review 2022] uses the recently published NORA3 wave

[2] `https://snl.no/Ekofisk`; accessed on June 10 2022.

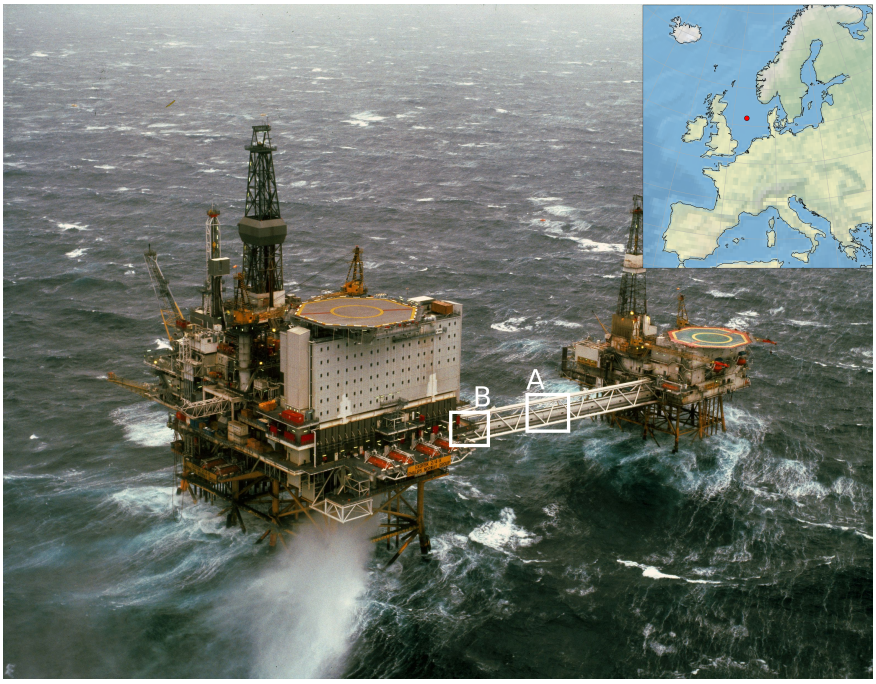

Figure 3.2: Aerial photograph of the Ekofisk 2/4 K (left) and 2/4 B (right) platforms (photo copyright owned by Husmo foto/ConocoPhillips/Norsk oljemuseum; reprinted with permission). The approximate locations of (A) the LASAR array and (B) the stereo camera system are marked by the squares. The inset map shows the location of the Ekofisk field in the central North Sea.

model hindcast covering the North Sea region [Breivik et al., 2022; Haakenstad et al., 2021] to estimate directional wave parameters. Wave height estimates from an earlier, lower-resolution hindcast [NORA10EI; Haakenstad et al., 2020] were also included in Paper I [Malila et al., 2022a]. Descriptions of the hindcast models can be found in the articles referenced herein, and will not be detailed here.

3.2.1 Laser altimeter array (LASAR)

Roughly a decade after the two Optech laser altimeters were installed at the main Ekofisk complex, the decision was made to replace one of them with a new instrument. The platform operator ConocoPhillips Norway ASA (COPNO) consulted Mark Donelan (at the University of Miami) and Anne Karin Magnusson (at the Norwegian Meteorological Institute) for the optimal location and type of instrument to be installed. The consultants recommended installing an array of downward-pointing laser altimeters on the footbridge

Figure 3.3: Housings of the four laser altimeters in the LASAR instrument, located on the footbridge connecting the Ekofisk 2/4 B and 2/4 K platforms. Photo by the author.

between the 2/4 K and B platforms. The array configuration would provide independent sea-surface elevation profiles, and could also be used to estimate the directional properties of the wavefield from the phase differences in the wave profiles recorded by the individual altimeters [Donelan et al., 1996]. The suggestion was accepted, and the final 2.6×2.6 m^2 altimeter array (LASAR) consisting of four Optech (now Teledyne Optech) Sentinel 3100 laser altimeters was made operational in February 2003 (see Figure 3.3).

The LASAR altimeters operate in the infrared band with a signal wavelength of 905 nm, and provide measurements of the instantaneous distance to the sea surface by converting the time of flight of discrete pulses emitted, reflected by the sea surface, and received by the instrument into range distance using the speed of light. The range measurements can be converted to sea-surface elevation by removing the mean level (estimated over a period of stationary wave conditions) from the signal. The operational sampling frequency, after built-in processing of raw signals emitted at 2 kHz, is 5 Hz, and data is acquired continuously throughout day and night. The 5-Hz data from all four altimeters is archived on MET Norway's servers. However, for operational purposes (such as forecasting and model validation), MET Norway has historically used a 2-Hz down-sampled signal from only one of the altimeters. The main reason for this is that the raw 5-Hz signals are often corrupted by artefacts such as spikes (i.e., unphysical range measure-

ments) and dropouts (i.e., missing measurement points), which cause errors that can be difficult to both detect and correct in the observed wave profiles and spectral parameters derived therefrom. Invalid measurements in the LASAR data appear to occur most often in calm sea states, which suggests that increased specular reflection by a smooth sea surface causes errors in the timing of received pulses [Magnusson and Donelan, 2013]. It is also known that infrared pulses at wavelengths used by the LASAR altimeters are sensitive to absorption and reflection by atmospheric aerosols (e.g., sea spray) [Toffoli et al., 2011], which may explain the sporadic occurrence of artefacts also in more strongly forced conditions.

Some studies [Donelan and Magnusson, 2017; Magnusson and Donelan, 2013] have been made of the full 5-Hz LASAR observations for analyses of extreme waves, but those have only focused on storm events of limited duration, which make it feasible to quality control the data manually. Because extreme wave analysis by definition focuses on rare events, the inclusion of undetected spikes in a data set can significantly skew the conclusions drawn from the analysis [Dysthe et al., 2008]. Gramstad et al. [2018], who despiked (using a combination of automated and manual verification) a full year's worth of downsampled 2-Hz LASAR data from 2016, found that only 42% of the included 20-minute records were of adequate quality to be used for statistical extreme wave analysis.

In an effort to exploit the full LASAR time series, the author implemented a number of existing despiking algorithms and applied them on the raw 5-Hz signals. Several of the algorithms implemented were originally designed to be used on turbulent velocity time series [Goring and Nikora, 2002; Mori et al., 2007; Wahl, 2003]. It was concluded that, while some of the algorithms were quite effective in "de-noising" the signals, the spike detection methods were generally unable to distinguish between large spikes and valid high wave crests. Consequently, processing the raw LASAR data in an unsupervised fashion with these algorithms was considered problematic due to the high likelihood of rejecting a large number records containing real extreme wave measurements. Furthermore, the high prevalence of noise corruption in the LASAR signals, especially in low sea states, essentially ruled out the implementation of semi-automated quality control measures aimed at quality controlling long wave measurement time series [Cattrell et al., 2018; Christou and Ewans, 2014; Gramstad et al., 2018].

To address the limitations of existing algorithms, Paper I [Malila et al., 2022a] presents a novel approach to wave record despiking. The new method, which builds on work by Bohlinger et al. [2019], was shown to be highly efficient in distinguishing between spikes and valid extreme waves in the LASAR 5-Hz signals. While the method was validated with measurements from the Ekofisk LASAR instrument, it can in all likelihood be applied successfully to measurements from other similar sensors. For Paper III, the full

5-Hz LASAR time series spanning 2003–2020 was quality controlled with the method introduced in Paper I. Moreover, all four co-located LASAR signals were used to verify the shapes of the most extreme waves and wave crests in the data set. The full quality-controlled LASAR time series will be made publicly available on a MET Norway server during the review process of Paper III.

3.2.2 Stereo video camera system

The stereo camera (SC) wave observation setup on the Ekofisk 2/4 Kilo (EKOK) oil platform located in the central North Sea was installed in December 2017 in a joint effort by the Norwegian Meteorological Institute (MET Norway) and the National University of Ireland, Galway (NUIG). The installation was funded by ConocoPhillips Norway ASA and Equinor ASA through the Joint Industry Project StereoWave. The SC setup was largely designed, built and installed by and under the supervision of Brian Scanlon, who at the time was a postdoctoral researcher at NUIG.

Setup

The EKOK SC setup (Figure 3.4) consists of two PointGrey (at present known as FLIR) PGE Blackfly 50S5C cameras equipped with 2/3" Sony Pregius CMOS sensors. Initially, the cameras were fitted with Computar M1614-MP2 2/3" 16 mm f1.4 lenses, but these were replaced with Edmund Optics 12 mm f1.4 MegaPixel lenses in February 2019. The cameras are contained in custom-made housings mounted 5.11 m apart on a north-northwest-facing railing approximately 28 m above mean sea level. The camera mounts use Delrin ball bearings, which allow for adjustments of the yaw and pitch levels of the camera views. From December 2017 until August 2019 the stereo cameras were inclined 35° from nadir (i.e., the downward-pointing vertical) and pointed 4.625° towards one another in the horizontal plane. The cameras were levelled using levels and inclinometers during installation in 2017, and the yaw values were calibrated using lasers. On August 7 2019, the yaw angle of both cameras was set to zero (so that the cameras point straight forward perpendicular to the railing on which they are mounted) and the viewing angle was raised to approximately 70° from nadir such that the upper edges of the stereo frames lie just below the horizon (to avoid exposure problems due to light from the sky). The yaw angle adjustment was performed in order to simplify the SC rig geometry (minimizing the rotational asymmetry between the cameras), and viewing angle adjustment was performed in order to maximize the sea-surface area covered by the overlapping stereo camera footprints. In the current work, only the latest (i.e., post-August 2019) SC

setup with 12 mm lenses and large field of view has been used. This choice was largely motivated by access to high-quality camera calibration materials for the latest SC setup (described in more detail below).

Figure 3.4: The Ekofisk stereo camera system in February 2019. Note that the stereo camera viewing angles in this photograph are steeper than in the current (post-August 2019) configuration used in this work. The white frame in the background belongs to the footbridge connecting the K and B platforms which houses the LASAR instrument. Photo by the author.

The stereo cameras are controlled by a dedicated PC located on-site at EKOK. The PC is connected via Ethernet cables to the local intranet and the two cameras, and can be accessed via remote login by MET Norway and NUIG. The camera triggering is controlled by an Arduino Uno microcontroller attached to the PC by USB. The PC is fitted with five removable 5 TB hard drives onto which the SC image frames are stored continuously in cyclic fashion. In the current configuration, the stereo frames are acquired and stored at a frame rate of 5 frames per second (fps) and at a resolution of 5 megapixels (MP). Timestamps at microsecond resolution are embedded in the image pixels and also saved in the individual image filenames. The acquisition system is hard-coded with daily updating daylight length, such that stereo frames are only acquired during daylight hours. When one hard drive is full, the system automatically switches to over-writing frames onto the following hard drive in sequence. Depending on the time of year, this system leaves MET Norway and NUIG with between approximately nine days and two weeks (depending on available daylight) to offload selected stereo frames onto

a separate hard drive before the images are overwritten. In a typical scenario, stereo frames are offloaded in continuous batches of approximately 1–10 hours following the passage of a wave event of interest.

The main limitations of the current SC system are twofold. First, the current maximum data offload bandwidth is 100 Mb/s, which makes the offload process slow when the data batches are large. Second, due to the relatively high 5-fps frame rate and 5 MP single-image resolution, the amount of data quickly grows very large, which puts high demands on the storage servers. The SC system also intermittently suffers from minor malfunctions, such as recurring lost stereo frames. During an eight-day test period in January 2020, the daily stereo frame loss was 7–24%. However, subsequent tests have shown lower daily loss rates of around 1 %, suggesting that the issue is time-varying. The exact cause of the missing frames is as of yet unknown; however, it may be related to timing issues due to the physical transfer of image data over approximately 100 m of cable from the cameras to the hard drives. Other potential causes include the mismatch timestamping of individual image pairs due to buffering lag time and variable exposure times between the two stereo cameras due to automatic exposure settings. The stereo frame losses generally occur sporadically, and long gaps (more than 1–2 consecutive missing frames) are uncommon.

The stereo image acquisition is largely controlled with custom C++ code (courtesy of Brian Scanlon) wrapped around FlyCapture, the commercial image acquisition software provided by the camera manufacturer. While the triggering of the stereo cameras occurs simultaneously through the Arduino Uno microcontroller, the image exposure of both stereo cameras is set to automatic mode, in which the shutter time and gain levels are optimized independently by each camera. Due to the close proximity and identical makeup of the stereo cameras, however, the automatic exposure settings generally lead to very similar image quality between the two cameras. Nevertheless, strict synchronization of the exposure settings may in the future help alleviate the intermittent issues regarding frame loss and other sporadic timing errors.

Calibration

The intrinsic calibration of the stereo camera lenses is a crucial step in the successful application of stereo imagery for sea-surface reconstruction [Benetazzo et al., 2012]. However, if performed in an organized manner and in a controlled environment, the intrinsic calibration is a fairly straightforward task thanks to the large number of publicly available tools which can be used to facilitate the process. Traditionally, the estimation of the geometry of the stereo camera setup has also required a separate extrinsic

calibration; however, recent stereo processing software such as the open source Wave Acquisition Stereo System (WASS) pipeline (see below) estimates the extrinsic parameters automatically. For this reason, we focus here on describing the estimation of the intrinsic parameters for the Ekofisk SC setup.

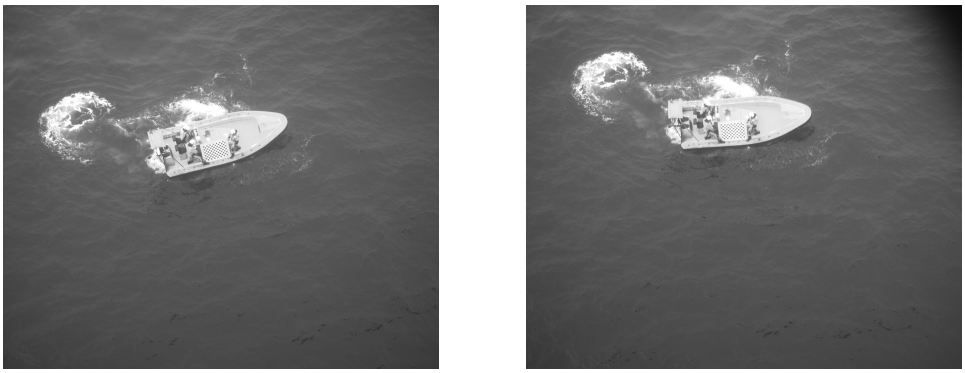

(a) (b)

Figure 3.5: Example stereo frame (left-camera frame in (a), right-camera frame in (b)) from the unsuccessful December 2017 field calibration.

After the initial installation of the SC setup on EKOK in late 2017, a field calibration was conducted on 20 December 2017 by filming a RIB boat with a large checkerboard pattern on board within the field of view of the SC setup (Figure 3.5). These images were planned to be used for both intrinsic and extrinsic calibration of the cameras. In hindsight, it was found that the distance from the cameras to the calibration targets was too large for accurate detection of the checkerboard pattern, leading to highly inconsistent estimates of the intrinsic parameters. The sequence of images acquired during the December 2017 calibration exercise was, therefore, not suited to be used for calibration purposes.

A new calibration exercise was performed on August 7 2019 on the deck of the EKOK platform using a checkerboard pattern consisting of 10×10 squares of 81 mm side length printed on a rigid aluminum board as a calibration target (Figure 3.6). On this occasion, care was taken to hold the calibration target close (within approximately 2–5 m) to the cameras, such that the checkerboard corners could be resolved with high accuracy. The calibration target was also tilted at various angles and positions relative to the cameras in order to allow a robust estimation of all six rotational degrees of freedom. The stereo camera calibration was performed using a subset of images from the August 7 2019 calibration exercise with Jean-Yves Bouguet's Matlab toolbox,[3] which implements the calibration method of Heikkilä and Silvén [1997]. The resulting intrinsic parameters for both stereo cameras, applied to all stereo reconstructions in the current work, are listed

[3] `http://robots.stanford.edu/cs223b04/JeanYvesCalib/index.html`; accessed on June 10 2022.

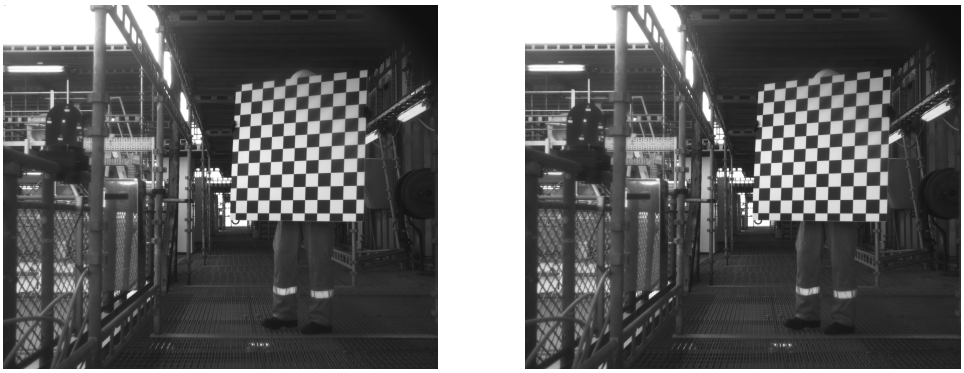

(a) (b)

Figure 3.6: Sample left-camera frame from the successful August 7 2019 on-deck intrinsic calibration at Ekofisk. (a) is the original raw frame, and (b) is the undistorted version of the same frame, in which the distortion correction has been done using the intrinsic parameters listed in Table 3.1.

in Table 3.1.

	Left camera	Right camera
Focal length $[f_x, f_y]$ (px)	[3475, 3472]	[3486, 3481]
Principal point $[c_x, c_y]$ (px)	[1232, 1073]	[1246, 1031]
Radial distortion $\boldsymbol{k}_\mathrm{r}$	[-0.0859, 0.2999, 0.0017]	[-0.0899, 0.3411, -0.0001]
Tangential distortion $\boldsymbol{k}_\mathrm{t}$	[0.0007, 0.0000]	[0.0001, 0.0000]

Table 3.1: Intrinsic parameters of the Ekofisk stereo cameras from the August 2019 calibration.

Processing

The stereo images acquired by the Ekofisk SC system were processed with the open-source Waves Acquisition Stereo System (WASS) software developed by researchers at the Institute of Marine Sciences (ISMAR) and the Ca' Foscari University in Venice, Italy [Benetazzo, 2006; Benetazzo et al., 2012; Bergamasco et al., 2017]. WASS is specifically developed for the purpose of wave field reconstruction from stereo video imagery, and consists of a streamlined pipeline including processes for automated extrinsic calibration, mean sea-plane estimation and dense 3D point cloud reconstruction. The main features of WASS and its application to the Ekofisk stereo video imagery are summarized here; for a more complete description of the processing software, the reader is advised to consult the references herein.

An innovative feature of WASS is its automated algorithm for estimating the extrinsic parameters (i.e., the essential matrix $\mathbf{E}$ in Eq. (2.13)) of a stereo camera setup without

requiring a complex and potentially hazardous field calibration (see Figure 3.5). The automatic extrinsic calibration consists of two subprocesses called *wass-match* and *wass-autocalibrate*. The matching process involves selecting a random subset of stereo frame pairs from the full sequence of stereo frames provided (a typical stereo sequence duration is similar to that of a conventional wave record, i.e., approximately 20 minutes), detecting a set of robust features in each frame pair, and matching the defined features following the approach of Albarelli et al. [2012]. The matched features are then used to estimate the extrinsic parameters for each pair of stereo frames. The subsequent auto-calibration process uses all matched features to optimize the global extrinsic parameters of the SC system.

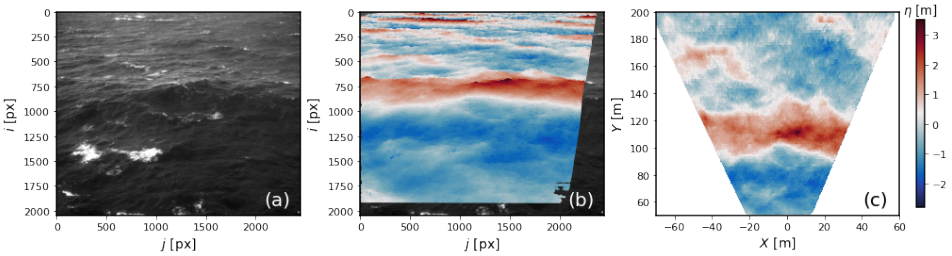

Figure 3.7: (a) Sample left-camera raw stereo frame from a stereo video acquisition on the Ekofisk platform on March 28 2020. (b) The WASS 3D reconstructed point cloud projected over the raw image in (a). (c) The Earth-referenced regular grid corresponding to the point cloud in (b), cropped to a range between 50 and 200 m from the cameras (in the Y direction). The color scale in (b) and (c) represents the sea-surface elevation η.

Once the extrinsic parameters have been estimated (and provided that the intrinsic parameters of the stereo cameras are known), the following subprocess in the WASS pipeline is called *wass-stereo*. In this stage, epipolar geometry is used to reconstruct dense 3D point clouds for each stereo frame pair by matching and triangulating all common pixels in the sequence of stereo frames provided. This process is independent for each stereo frame pair, which makes it straightforward to parallelize the processing. After the stereo reconstruction, a subset of 3D point clouds is chosen randomly for the estimation of the mean sea plane. The mean sea plane was estimated within a limited, close-range sub-region of the reconstructed scene to avoid the influence of potentially erroneously reconstructed 3D positions in the far field. Finally, the orientation of the mean sea plane is used to reproject the point clouds to an Earth-referenced world coordinate system, followed by a gridding operation resulting in regularly spaced (X, Y, Z) sea surface elevation grids at 0.5-m horizontal resolution (Figure 3.7).

The Ekofisk stereo video data set was processed on the computing nodes of the MET

Norway's post-processing infrastructure (PPI). Pre and post-processing routines and technical documentation for the processing of stereo imagery from the Ekofisk SC system have been published by the author at `https://github.com/mikapm/wass-pyfuns`.

Validation

The Ekofisk SC system is central in the analysis of Papers II [Malila et al., 2022b] and III [Malila et al., under review] of the current thesis. These studies use nearly the identical set of stereo video data: in Paper II, 28 20-minute space-time sea-surface reconstructions from 5 separate days in the winter season of 2019–2020 are used; in Paper III, the same data set is used with the addition of one 20-minute segment (starting at 10:40 UTC on February 11 2020) which was processed after Paper II was submitted. Table 3.2 summarizes selected one-dimensional (frequency) spectral parameters estimated for the stereo video acquisition periods from three independent observational instruments (all located on the 2/4 K platform): the quality-controlled LASAR signals (L), virtual wave staffs from the stereo video data (S) and the X-band WaMoS radar spectra (W). Hourly output from the nearest grid point in the NORA3 hindcast (N) is also included in the comparison. The 1D parameters compared are the significant wave height H_s (Eq. (2.6)), the mean wave period $T_\mathrm{m} = m_0/m_1$ and the spectral steepness $\epsilon = \sqrt{2m_0}k_\mathrm{m}$, where $\sqrt{2m_0}$ is taken as an estimate of the wave amplitude (following Serio et al. [2005]) and the mean wavenumber k_m is estimated from T_m using the linear dispersion relationship (2.2). It should be noted that Table 3.2 is a more comprehensive reproduction of Table 1 of Paper III, which only shows daily averages and omits the WaMoS measurements. The stereo video frequency spectra were also validated graphically against LASAR and WaMoS in Fig. 2 of Paper II.

The comparison of 1D spectral parameters displays overall consistency, with some degree of scatter, in the spectral estimates from the different sources. Importantly, none of the instruments is focused on the exact same patch of ocean. Apart from potential systematic differences between the sensors' sampling properties, statistical sampling variability (both spatial and temporal) may therefore explain a large part of the variability in the spectral parameters seen in Table 3.2 [Bitner-Gregersen and Hagen, 1990; Bitner-Gregersen and Magnusson, 2014; Donelan and Pierson, 1983].

The directional spectral properties of the Ekofisk SC system are validated against WaMoS and NORA3 frequency–directional spectra $E(\omega, \theta)$ in Tables 3.3 and 3.4. These two tables are more complete (i.e., not averaged) versions of Table 2 in Paper III. Due to the limited overlapping footprint of the stereo cameras, which prevented resolving the largest spatial scales (i.e., wavelengths) during the majority of the acquisition periods, the

		H_s [m]				T_m [s]				ϵ			
Date	Record	L	N	S	W	L	N	S	W	L	N	S	W
2019-12-09	12:00	6.07	5.96	5.48	5.96	8.01	8.59	8.06	8.37	0.13	0.11	0.12	0.12
2019-12-09	12:20	6.06	5.96	6.71	6.05	8.21	8.59	9.37	8.59	0.13	0.11	0.11	0.12
2019-12-09	12:40	6.38	6.52	6.81	6.63	8.53	9.08	9.02	8.85	0.12	0.11	0.12	0.12
2019-12-09	13:00	7.18	6.52	6.19	7.05	9.03	9.08	8.85	8.97	0.13	0.11	0.11	0.12
2019-12-09	13:20	7.46	6.52	6.46	6.27	9.37	9.08	8.96	8.80	0.12	0.11	0.11	0.12
2019-12-09	13:40	6.32	6.53	7.02	6.07	8.88	9.18	9.26	8.68	0.11	0.11	0.12	0.11
2019-12-09	14:00	6.82	6.53	6.54	6.64	8.98	9.18	8.67	8.78	0.12	0.11	0.12	0.12
2020-01-04	09:00	5.84	5.09	5.57	5.72	9.71	8.70	8.97	8.66	0.09	0.10	0.10	0.11
2020-01-04	09:20	6.40	5.09	5.90	5.27	10.20	8.70	9.35	8.40	0.09	0.10	0.10	0.11
2020-01-04	09:40	5.41	4.98	5.46	5.50	9.46	8.73	9.25	8.34	0.09	0.09	0.09	0.11
2020-01-04	10:00	5.36	4.98	5.77	6.26	9.19	8.73	9.56	8.70	0.09	0.09	0.09	0.12
2020-01-04	10:20	5.77	4.98	5.42	5.70	9.73	8.73	9.11	8.53	0.09	0.09	0.09	0.11
2020-01-04	10:40	5.74	4.81	5.23	5.28	9.22	8.74	8.80	8.26	0.10	0.09	0.10	0.11
2020-01-04	11:00	5.06	4.81	5.99	5.04	9.12	8.74	9.94	8.17	0.09	0.09	0.09	0.11
2020-01-04	11:40	5.76	4.60	5.10	5.60	9.74	8.75	8.93	8.40	0.09	0.09	0.09	0.11
2020-02-11	10:00	5.56	5.11	5.35	5.11	7.99	7.50	7.99	7.98	0.12	0.13	0.12	0.11
2020-02-11	10:40	5.59	5.23	5.57	5.78	8.06	7.45	8.00	8.00	0.12	0.13	0.12	0.13
2020-02-11	12:00	5.08	5.39	5.89	5.31	7.94	7.56	8.04	8.12	0.11	0.13	0.13	0.11
2020-03-28	15:00	2.85	2.98	2.77	3.01	5.82	5.68	5.85	6.26	0.12	0.13	0.12	0.11
2020-03-28	15:20	2.83	2.98	3.11	3.22	5.96	5.68	6.00	6.31	0.11	0.13	0.12	0.12
2020-03-28	16:20	3.25	3.33	3.39	3.28	6.18	6.01	6.10	6.70	0.12	0.13	0.13	0.10
2020-03-28	17:20	3.99	3.71	4.43	4.46	6.73	6.30	6.97	7.11	0.13	0.13	0.13	0.13
2020-03-28	17:40	4.65	4.06	4.40	4.44	7.07	6.59	7.05	7.22	0.13	0.13	0.13	0.12
2020-04-13	08:00	4.44	4.22	4.83	4.47	8.25	8.29	8.66	8.01	0.09	0.09	0.09	0.10
2020-04-13	08:20	4.77	4.22	4.71	4.61	8.55	8.29	8.60	7.96	0.09	0.09	0.09	0.10
2020-04-13	08:40	4.68	4.13	4.61	4.79	8.76	8.30	8.72	7.96	0.09	0.09	0.09	0.11
2020-04-13	09:00	4.50	4.13	5.07	4.87	8.62	8.30	8.96	8.02	0.09	0.09	0.09	0.11
2020-04-13	09:20	5.20	4.13	4.24	4.34	9.08	8.30	8.02	7.80	0.09	0.09	0.09	0.10
2020-04-13	10:00	4.72	4.05	4.27	5.06	8.36	8.27	8.29	8.00	0.10	0.08	0.09	0.11

Table 3.2: Significant wave height H_s, mean wave period T_m and spectral steepness ϵ during the 20-minute stereo video acquisition periods (of which the start times, in UTC, are indicated in the second column) from the hourly output of the NORA3 wave model hindcast (N) and the co-located LASAR (L), WASS stereo video (S) and WaMoS X-band radar (W) observations.

frequency–directional stereo video spectra were estimated using the extended maximum entropy principle (EMEP) method [Hashimoto et al., 1994; Lygre and Krogstad, 1986] from 1D sea-surface elevation time series at different grid points within the reconstructed grid.

		L_x [m]			L_y [m]		
Date	Record	N	S	W	N	S	W
2019-12-09	12:00	80.62	87.20	68.73	99.05	98.37	93.24
2019-12-09	12:20	80.62	92.27	71.05	99.05	98.29	96.34
2019-12-09	12:40	88.32	98.21	67.95	108.71	97.89	99.51
2019-12-09	13:00	88.32	93.49	66.94	108.71	97.16	96.31
2019-12-09	13:20	88.32	102.10	65.15	108.71	96.23	96.70
2019-12-09	13:40	90.14	104.15	65.15	108.75	86.54	91.36
2019-12-09	14:00	90.14	81.09	64.33	108.75	82.84	91.34
2020-01-04	09:00	76.23	92.73	79.08	88.55	104.00	84.58
2020-01-04	09:20	76.23	97.41	77.99	88.55	106.69	82.51
2020-01-04	09:40	77.47	94.11	78.91	88.68	102.92	85.09
2020-01-04	10:00	77.47	104.30	78.01	88.68	121.21	83.32
2020-01-04	10:20	77.47	99.70	75.24	88.68	111.36	80.72
2020-01-04	10:40	76.44	92.38	75.33	86.13	108.52	80.73
2020-01-04	11:00	76.44	112.94	73.99	86.13	127.38	84.15
2020-01-04	11:40	75.08	103.79	73.93	84.25	116.75	79.04
2020-02-11	10:00	65.35	95.24	100.83	76.57	102.85	95.42
2020-02-11	10:40	63.78	86.95	102.80	76.67	93.92	94.10
2020-02-11	12:00	66.26	95.94	104.74	78.59	109.09	99.71
2020-03-28	15:00	40.67	50.17	56.32	50.41	58.40	67.10
2020-03-28	15:20	40.67	52.98	56.32	50.41	64.56	66.47
2020-03-28	16:20	44.93	62.61	53.28	55.48	71.99	67.65
2020-03-28	17:20	48.63	72.31	48.75	60.15	91.01	65.03
2020-03-28	17:40	52.01	68.08	48.44	63.98	81.81	62.17
2020-04-13	08:00	69.50	77.76	52.59	82.50	91.12	71.08
2020-04-13	08:20	69.50	80.22	51.62	82.50	92.32	67.47
2020-04-13	08:40	69.04	82.79	50.36	81.25	95.13	70.46
2020-04-13	09:00	69.04	86.13	48.80	81.25	105.82	71.03
2020-04-13	09:20	69.04	82.59	49.40	81.25	100.25	69.69
2020-04-13	10:00	68.49	77.63	47.45	81.46	91.56	65.65

Table 3.3: Wavelength L_x and crestlength L_y during the stereo video acquisitions estimated from frequency–directional spectra from the NORA3 hindcast (N), WASS stereo video (S) and WaMoS (W).

The wavelength L_x and crestlength L_y were estimated from the spectra rotated such that

the the x axis was aligned with the peak wave direction. The expressions for L_x and L_y are given by $L_x = 2\pi\sqrt{m_{000}/m_{200}}$ and $L_y = 2\pi\sqrt{m_{000}/m_{020}}$, where m_{ijl} represent directional spectral moments, defined as [Fedele, 2012]

$$m_{ijl} = \int_0^{2\pi}\int_0^{\infty} k_x^i k_y^j \omega^l E(\omega,\theta)\,\mathrm{d}\omega\,\mathrm{d}\theta. \tag{3.1}$$

More variability is seen among the different L_x and L_y estimates in Table 3.3 compared to the 1D parameters in Table 3.2, especially in the stereo video estimates. This variability is also apparent in the stereo video estimates of the directional spread σ_θ (Table 3.4), defined following Kuik et al. [1988] as

$$\sigma_\theta^2 = \left(1 - \sqrt{\left(\frac{\int \sin(\theta)E(\omega,\theta)\,\mathrm{d}\omega\,\mathrm{d}\theta}{\int E(\omega,\theta)\,\mathrm{d}\omega\,\mathrm{d}\theta}\right)^2 + \left(\frac{\int \cos(\theta)E(\omega,\theta)\,\mathrm{d}\omega\,\mathrm{d}\theta}{\int E(\omega,\theta)\,\mathrm{d}\omega\,\mathrm{d}\theta}\right)^2}\right). \tag{3.2}$$

The directional spread of the stereo video spectra is in general wider than the other estimates. This contrasts with the findings of Donelan et al. [2015], who found that EMEP generates narrower spectra than other commonly used methods. The mean wave direction θ_m is highly consistent among all three spectral sources.

		θ_m [deg]			σ_θ [deg]		
Date	Record	N	S	W	N	S	W
2019-12-09	12:00	159.67	157.75	158.62	30.41	43.50	32.39
2019-12-09	12:20	159.67	157.80	160.75	30.41	46.91	32.39
2019-12-09	12:40	161.29	161.55	162.58	29.58	48.54	31.94
2019-12-09	13:00	161.29	163.15	163.86	29.58	51.04	30.98
2019-12-09	13:20	161.29	164.05	163.82	29.58	46.81	31.80
2019-12-09	13:40	162.07	163.89	164.71	29.82	52.46	32.37
2019-12-09	14:00	162.07	163.05	166.67	29.82	53.55	31.14
2020-01-04	09:00	143.60	144.66	149.69	37.31	49.85	40.14
2020-01-04	09:20	143.60	141.31	149.27	37.31	47.68	41.06
2020-01-04	09:40	146.55	147.49	147.66	36.67	47.39	40.21
2020-01-04	10:00	146.55	153.95	152.09	36.67	44.45	37.78
2020-01-04	10:20	146.55	150.99	154.00	36.67	45.33	39.14
2020-01-04	10:40	148.40	145.32	153.48	36.08	47.41	40.73
2020-01-04	11:00	148.40	152.16	150.68	36.08	43.70	39.22
2020-01-04	11:40	149.78	146.55	153.16	35.52	45.51	39.83
2020-02-11	10:00	86.45	80.96	73.64	36.06	44.06	31.57
2020-02-11	10:40	88.96	80.46	74.61	36.08	46.42	32.31
2020-02-11	12:00	90.21	85.02	79.67	36.01	43.90	33.44
2020-03-28	15:00	174.39	172.86	177.17	31.98	53.21	28.39
2020-03-28	15:20	174.39	174.85	179.04	31.98	53.37	27.45
2020-03-28	16:20	174.85	168.79	181.35	31.78	50.96	30.63
2020-03-28	17:20	175.80	179.24	181.04	31.59	45.01	30.21
2020-03-28	17:40	176.82	178.23	181.25	31.43	47.39	29.96
2020-04-13	08:00	173.62	168.21	175.08	26.23	45.92	29.17
2020-04-13	08:20	173.62	172.22	175.11	26.23	44.26	29.42
2020-04-13	08:40	174.00	173.36	174.19	26.16	44.69	30.25
2020-04-13	09:00	174.00	172.24	174.29	26.16	40.80	29.68
2020-04-13	09:20	174.00	174.71	173.81	26.16	41.47	29.29
2020-04-13	10:00	174.21	171.53	175.02	25.99	43.71	28.52

Table 3.4: As Table 3.3, but for the mean wave direction θ_m and the directional spread σ_θ.

3.3 North Pacific cruise data set

In addition to the Ekofisk data sets, Paper II [Malila et al., 2022b] is supplemented with whitecap coverage observations made during a December 2019 cruise onboard the R/V

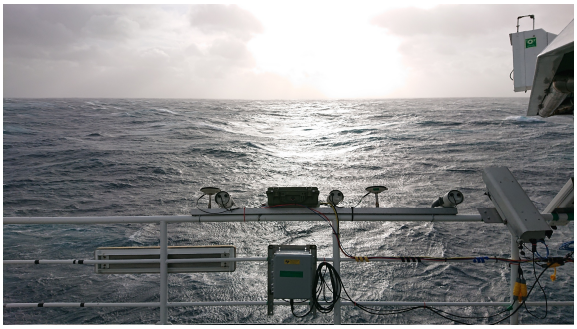

(a)

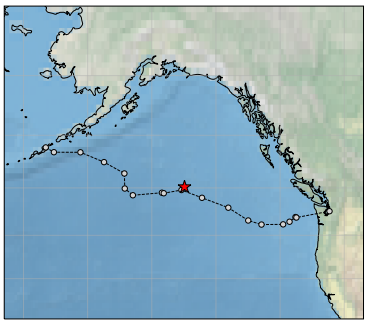

(b)

Figure 3.8: (a) The port-side three-camera system onboard R/V Sikuliaq. The casing between the two leftmost cameras houses the IMU-GNSS system. The instrument to the right of the cameras is an infrared camera system, which was not used in this work. Photo by the author. (b) Daily positions along the cruise track marked with gray circles. The location of Ocean Station Papa is marked with a star.

Sikuliaq in the North Pacific (see Figure 3.8). The cruise departed from Dutch Harbor, Alaska, on December 5, made a stop at Ocean Station Papa in the central Gulf of Alaska for a wave buoy recovery and deployment, and concluded in Seattle, Washington, on December 23. To summarize the instrumentation, of which a more detailed description can be read in Paper II and references therein, two triple-camera systems were mounted on the port and starboard sides on the bridge deck of the vessel, at approximately 16-m height above the water surface. Both camera systems consisted of two PointGrey Flea2 cameras with 9-mm lenses on the sides plus one PointGrey Flea2G camera with a wider-angle 2.8-mm lens in the middle. While all cameras were in use during the experiment, frames were only analyzed from the middle, wide-angle cameras. The two cameras on the sides were used with the aim of performing stereo video reconstructions similar to those reported by Schwendeman and Thomson [2017]. This plan was, however, abandoned due to problems experienced with the alignment of the combined intertial motion unit (IMU)–global navigation satellite (GNS) system required for motion correction, as well as the frequent severe rolling motion of the vessel, which often made the overlapping stereo camera footprints excessively small. Wave measurements during the cruise were made with freely drifting SWIFT buoys [Thomson, 2012] which were deployed and recovered daily during the course of the cruise.

Chapter 4

Summary of the scientific results

The scientific findings of the current thesis are reported in the three academic papers summarized here. The full papers are attached in Chapter 6 of this thesis.

4.1 Paper I: A Nonparametric, Data-Driven Approach to Despiking Ocean Surface Wave Time Series

Mika P. Malila, Patrik Bohlinger, Susanne Støle-Hentschel, Øyvind Breivik, Gaute Hope and Anne Karin Magnusson.

The laser altimeter array (LASAR), located between the Ekofisk 2/4 K and 2/4 B platforms, constitutes a unique, long-term, high-temporal resolution sea-surface elevation data set spanning nearly 20 years at the time of writing. Due to the complicated noise characteristics of the instrument, the data set has previously not been exploited to its full potential, with a handful of prior studies focusing largely on short-term event analyses. In this paper, we develop and validate a novel quality control methodology for wave measurements applicable to laser altimeter and related observations, using sample data from the LASAR instrument. The methodology, which is based on Gaussian Process (GP) regression, is an extension of the recent wave model validation methodology of Bohlinger et al. [2019]. The main findings of Paper I are summarized below.

- A data-based despiking and data replacement methodology aimed at post-processing quality control (QC) of surface wave measurements is developed. The

methodology, based on GP regression, extends the wave model validation methodology of Bohlinger et al. [2019] to high-resolution sea-surface elevation data.

- The probabilistic approach provides an uncertainty estimate around the non-parametric GP regression mean function. This functionality is used for spike detection and subsequent interpolation of missing and discarded erroneous data points.
- Applying the proposed methodology on a sample LASAR data set from a storm in November 2007 (also analyzed by Magnusson and Donelan [2013] and Donelan and Magnusson [2017]), is shown to lead to improved signal correlation among the four effectively co-located laser altimeters as well as improved spectral tail consistency.
- The performance of the proposed methodology is also compared against the recently published phase space-based despiking method of Voermans et al. [2021]. While the phase space method is considerably more efficient computationally, the GP method is found to be more robust with regards to false positive spike detection and removal.
- The relatively high computational cost of the proposed QC methodology makes it, at present, best suited to offline post-processing applications. Lastly, while the proposed methodology is fully automated, it is stressed that thorough quality control of wave measurements aimed at extreme wave analysis should not neglect human verification of the most extreme measurements.

4.2 Paper II: On the groupiness and intermittency of oceanic whitecaps

Mika P. Malila, Jim Thomson, Øyvind Breivik, Alvise Benetazzo, Brian Scanlon and Brian Ward.

First described qualitatively by Donelan et al. [1972], the modulation of deep-water wave breaking activity (i.e., whitecapping) due to the wave-field group structure has been studied extensively in controlled settings and theoretically [e.g., Banner and Peirson, 2007; Perlin et al., 1996; Rapp and Melville, 1990; Saket et al., 2017; Song and Banner, 2002], but relatively few studies have quantified the process with field measurements [Dulov et al., 2002, 2021; Holthuijsen and Herbers, 1986; Smith et al., 1996]. In this paper, we investigate the relationship between wave groups and the instantaneous whitecap coverage within the footprint of the Ekofisk stereo cameras. For this analysis, the WASS

stereo-reconstructed sea surface is used to detect wave groups using a threshold of the instantaneous wave energy, and coherent whitecap coverage W is estimated from the unprocessed raw input frames. In addition, incoherent (i.e., not co-located) measurements of the whitecap coverage from ship-based cameras and wave spectral parameters from nearby drifting wave buoys are used as a supplemental data set for investigating the periodicity and intermittency of whitecapping. The main findings of Paper II are summarized below.

- The coherent wave breaking and wave group measurements from the Ekofisk stereo cameras show that the instantaneous whitecap coverage is significantly enhanced during wave group passage, indicating that wave breaking activity is strongly modulated by wave groups. The result holds both for the total whitecap coverage W, for which we observe a two-to-threefold enhancement during wave groups, and for the actively breaking whitecap coverage W_{A}, for which the enhancement is approximately fivefold.

- The group modulation is also observed in temporally averaged estimates of the whitecap coverage $\overline{W}$ and $\overline{W}_{\mathrm{A}}$.

- An analysis is also performed on the time scales of wave breaking using time series of the instantaneous whitecap coverage from both the Ekofisk and North Sea data sets. It is found that, on average, inter-breaking timescales are aligned with the periodicity of the dominant waves, supporting previous findings regarding the long-wave modulation of short-wave breaking [Dulov et al., 2002, 2021].

- A spectral analysis of the instantaneous whitecap coverage time series shows that the peak spectral density of W is aligned with the peak wave spectral density, providing additional evidence for the importance of the dominant waves in determining the periodicity of wave breaking [see also Donelan et al., 1972].

- Finally, the spectral density of the inter-breaking time scales, estimated using the telegraphic approximation (TA) approach of Sreenivasan and Bershadskii [2006], is found to approximately conform to a theoretical power-law shape for general stochastic processes.

4.3 Paper III: Statistical and dynamical characteristics of extreme wave crests assessed with field measurements from the North Sea

Mika P. Malila, Francesco Barbariol, Alvise Benetazzo, Øyvind Breivik, Anne Karin Magnusson, Jim Thomson and Brian Ward.

Following the publication of the GP regression-based despiking protocol in Paper I, the full 5-Hz, four-laser LASAR time series covering the time period from February 2003 to October 2020 was quality controlled using the methodology described in Paper I. After the automated despiking of the LASAR signals, all remaining rogue wave ($H_{\max} \geq 2H_{\mathrm{s}}$) and rogue crest ($C_{\max} \geq 1.25H_{\mathrm{s}}$) events were visually controlled by comparing the simultaneous wave profiles obtained from the effectively co-located laser altimeters. A number of individual-laser records were thus found to contain spurious rogue events (i.e., undetected spikes); such records were subsequently discarded from the quality controlled data set.

In Paper III, the quality controlled LASAR data set is used to investigate the statistical properties of extreme wave crests in a wide range of sea states categorized by their spectral steepness and directional spread. Furthermore, the Ekofisk stereo video data set from Paper II is reused with the aim of investigating the space-time statistics, crest geometry and crest speed dynamics of extreme wave crests. The main findings of Paper III are summarized below.

- The quality control (QC) procedure reveals that the Ekofisk LASAR instrument returns high-quality sea-surface elevation measurements only when the sea state is sufficiently energetic. A lower bound for acceptable signal quality is found at approximately $H_{\mathrm{s}} = 3$ m. The post-QC LASAR data set covers storm events in the 2003–2020 period, with a total wave count of approximately 7×10^6 zero-crossing waves.

- Extreme individual wave heights in the LASAR data set largely conform to the Stokes–Miche breaking-constrained steepness limit. Bulk wave steepness computed in terms of H_{s} and k_{m} is compared to the empirical limit found by Zippel and Thomson [2017]. While the majority of sea states are constrained by the bulk limit, sea states with steepness in the highest percentile lie above the limit.

- The high-order statistical moments of skewness and kurtosis, computed from sea-

surface elevation time series, are only weakly related to common spectral parameters used to describe the susceptibility of a sea state to increased rogue wave probability.

- Empirical crest height exceedance probabilities estimated from the LASAR data set are classified by sea-state steepness and directional spread, where the directional spread is estimated from NORA3 hindcast spectra. A clear indication is found for a systematic deviation of the empirical distributions from standard linear and second-order distributions with increased sea-state steepness and narrowing directional spread. This result is consistent with prevailing theory on modulational instability, although the directional properties of the sea states in the LASAR data set generally exceed those of laboratory and numerical experiments in which the process has been shown to be active.

- The statistics of space-time extreme (STE) crest heights within the Ekofisk stereo camera footprint conform on average well to second-order theoretical estimates, especially for large relative space-time volumes.

- Geometric STE crest steepness is found to be systematically lower than the crest steepness of the same waves estimated with the linear dispersion relation applied to the maximum crest point time series. The highest directly measured values of the crest steepness conform to the Stokes limit, whereas the maximum steepness inferred from dispersion is found to exceed the Stokes limit by up to 25%.

- Directly measured STE crest speeds are shown, on average, to slow down to approximately 80% of the linear phase speed. The slowdown is highly localized on the moment of wave group focus, supporting previous observations and theory of the phenomenon [Banner et al., 2014; Fedele et al., 2020; Schwendeman and Thomson, 2017]. As opposed to previous studies, both breaking and non-breaking focused wave crests are shown to slow down at a similar rate. The crest speed slowdown is proposed as an explanation for the discrepancy between directly measured crest steepness and crest steepness inferred from dispersion.

Chapter 5

Conclusions

5.1 Main takeaways

Geometric, kinematic and dynamic characteristics of dominant (i.e., the most energetic) ocean-surface gravity waves have been studied using close-range remote sensing field measurements. Stereo imagery-based sea-surface reconstructions from a platform-based stereo camera system at the Ekofisk platform complex in the central North Sea and ship-based single-camera imagery from a cruise in the North Pacific were used to investigate the wave-group influence on the intermittency of the oceanic whitecap coverage. The Ekofisk stereo reconstructions were also used to study the shape and motion characteristics of the largest crests encountered in spatially and temporally resolved sea-surface segments.

Statistical properties of large wave crests were studied with a long-term, high-resolution laser altimeter time series of the sea-surface elevation located on the same Ekofisk platform as the stereo camera system. A novel, data-driven quality control procedure was used to validate extreme wave measurements in the time series. Moreover, space-time statistics were also investigated with the stereo reconstructions. The main takeaways from the research described in this thesis are summarized in brief below, and more thoroughly in the previous chapter.

- Modern data-driven machine learning tools can be successfully applied to quality controlling wave measurements. However, human intervention is still necessary for the verification of extreme observations.
- Spatially and temporally resolved wave-field measurements obtained via stereo camera systems are a valuable complement to traditional point measurement sys-

tems such as wave buoys and laser altimeters. The use of stereo video data has been illustrated here through observations of enhanced wave breaking in wave groups and crest-speed slowdown of extreme wave crests.

- Care should be taken when applying low-order, idealized approximations, such as the linear dispersion relation, to characterize the properties of steep, nonlinear waves in the open ocean.

5.2 Outlook and future perspectives

Observational studies such as those presented in this thesis are especially valuable when their results can be used to improve predictive models of the processes they represent. The representation of incipient wave breaking, for instance, is a notoriously complex problem in commonly used phase-resolving numerical wave models based on high-order spectral (HOS) methods [e.g., Seiffert et al., 2017]. In this regard, observational evidence on the role of group dynamics in the breaking process, such as that presented in the current thesis, helps validate the theoretical frameworks [e.g., Barthelemy et al., 2018] on which many breaking parameterizations are formulated. Dominant (long) wave-induced breaking modulation has also been implemented in a spectral dissipation source term parameterization for phase-averaged wave models by Romero [2019]. In his formulation, the modulation factor is considerably larger than the modulation magnitude observed in the current work (Paper II) and other recent studies [Dulov et al., 2002, 2021], which goes to show that more experiments focused on the phenomenon are needed to reach a consensus on the magnitude, and potential sea-state dependence, of the influence of wave groups on wave breaking.

A limitation inherent in the remote sensing techniques on which the research presented in this thesis is focused is that only surface processes are resolved. Quantifying climatologically relevant variables, such as the energy dissipation or bubble entrainment rates associated with wave breaking events, requires additional subsurface measurements. If combined with coherent surface-sensing measurements acquired via, e.g., stereo imagery, measurements of sub-surface dissipation rates or bubble plume depths can significantly advance the general understanding of the dynamics of wave-driven processes at the air-sea interface [Callaghan et al., 2016]. At the time of writing, the author is aware of such ongoing and upcoming experiments in Italy, Norway (Ekofisk) and California, which indicates that exciting progress will be made on this front in the near future. Moreover, recent advances in image processing software for stereo wave sensing [e.g., Bergamasco et al., 2021] suggest that high-resolution sea surface reconstructions may, also in the near

future, be monitored in real time.

Bibliography

T. A. A. Adcock and P. H. Taylor. The physics of anomalous ('rogue') ocean waves. *Reports on Progress in Physics*, 77(10):105901, 2014.

R. J. Adler. *The Geometry of Random Fields*. John Wiley, 1981.

Y. C. Agrawal, E. A. Terray, M. A. Donelan, P. A. Hwang, A. J. Williams, W. M. Drennan, K. K. Kahma, and S. A. Krtaigorodskii. Enhanced dissipation of kinetic energy beneath surface waves. *Nature*, 359(6392):219–220, 1992.

A. Albarelli, E. Rodolà, and A. Torsello. Imposing semi-local geometric constraints for accurate correspondences selection in structure from motion: A game-theoretic perspective. *International journal of computer vision*, 97(1):36–53, 2012.

A. Ali, K. H. Christensen, Ø. Breivik, M. P. Malila, R. P. Raj, L. Bertino, E. P. Chassignet, and M. Bakhoday-Paskyabi. A comparison of Langmuir turbulence parameterizations and key wave effects in a numerical model of the North Atlantic and Arctic Oceans. *Ocean Modelling*, 137:76–97, 2019.

M. D. Anguelova and F. Webster. Whitecap coverage from satellite measurements: A first step toward modeling the variability of oceanic whitecaps. *Journal of Geophysical Research: Oceans*, 111(C3), 2006.

F. Ardhuin, E. Rogers, A. V. Babanin, J.-F. Filipot, R. Magne, A. Roland, A. Van Der Westhuysen, P. Queffeulou, J.-M. Lefevre, and L. Aouf. Semiempirical dissipation source functions for ocean waves. Part I: Definition, calibration, and validation. *Journal of Physical Oceanography*, 40(9):1917–1941, 2010.

A. V. Babanin. *Breaking and dissipation of ocean surface waves*. Cambridge University Press, 2011.

M. L. Banner. Equilibrium spectra of wind waves. *Journal of Physical Oceanography*, 20(7):966–984, 1990.

M. L. Banner and W. L. Peirson. Wave breaking onset and strength for two-dimensional deep-water wave groups. *Journal of Fluid Mechanics*, 585:93–115, 2007.

M. L. Banner, I. S. F. Jones, and J. C. Trinder. Wavenumber spectra of short gravity waves. *Journal of Fluid Mechanics*, 198:321–344, 1989.

M. L. Banner, X. Barthelemy, F. Fedele, M. Allis, A. Benetazzo, F. Dias, and W. L. Peirson. Linking reduced breaking crest speeds to unsteady nonlinear water wave group behavior. *Physical review letters*, 112(11):114502, 2014.

S. F. Barstow, H. E. Krogstad, L. Lønseth, J. P. Mathisen, G. Mørk, and P. Schjølberg. Intercomparison of sea-state and zero-crossing parameters from the WACSIS field experiment and interpretation using video evidence. *J. Offshore Mech. Arct. Eng.*, 126 (1):35–42, 2004.

X. Barthelemy, M. L. Banner, W. L. Peirson, F. Fedele, M. Allis, and F. Dias. On a unified breaking onset threshold for gravity waves in deep and intermediate depth water. *Journal of Fluid Mechanics*, 841:463–488, 2018.

A. Baxevani and I. Rychlik. Maxima for Gaussian seas. *Ocean Engineering*, 33(7): 895–911, 2006.

S. E. Belcher, A. L. M. Grant, K. E. Hanley, B. Fox-Kemper, L. Van Roekel, P. P. Sullivan, W. G. Large, A. Brown, A. Hines, and D. Calvert. A global perspective on Langmuir turbulence in the ocean surface boundary layer. *Geophysical Research Letters*, 39(18), 2012.

A. Benetazzo. Measurements of short water waves using stereo matched image sequences. *Coastal engineering*, 53(12):1013–1032, 2006.

A. Benetazzo, F. Fedele, G. Gallego, P.-C. Shih, and A. Yezzi. Offshore stereo measurements of gravity waves. *Coastal Engineering*, 64:127–138, 2012.

A. Benetazzo, F. Barbariol, F. Bergamasco, A. Torsello, S. Carniel, and M. Sclavo. Observation of extreme sea waves in a space–time ensemble. *Journal of Physical Oceanography*, 45(9):2261–2275, 2015.

A. Benetazzo, F. Ardhuin, F. Bergamasco, L. Cavaleri, P. V. Guimaraes, M. Schwendeman, M. Sclavo, J. Thomson, and A. Torsello. On the shape and likelihood of oceanic rogue waves. *Scientific Reports*, 7(1):1–11, 2017.

A. Benetazzo, F. Barbariol, and S. Davison. Short-term/range extreme-value probability distributions of upper bounded space-time maximum ocean waves. *Journal of Marine Science and Engineering*, 8(9):679, 2020.

A. Benetazzo, F. Barbariol, F. Bergamasco, L. Bertotti, J. Yoo, J.-S. Shim, and L. Cavaleri. On the extreme value statistics of spatio-temporal maximum sea waves under cyclone winds. *Progress in Oceanography*, 197:102642, 2021.

T. B. Benjamin and J. E. Feir. The disintegration of wave trains on deep water Part 1. Theory. *Journal of Fluid Mechanics*, 27(3):417–430, 1967.

F. Bergamasco, A. Torsello, M. Sclavo, F. Barbariol, and A. Benetazzo. WASS: An open-source pipeline for 3D stereo reconstruction of ocean waves. *Computers & Geosciences*, 107:28–36, 2017.

F. Bergamasco, A. Benetazzo, J. Yoo, A. Torsello, F. Barbariol, J.-Y. Jeong, J.-S. Shim, and L. Cavaleri. Toward real-time optical estimation of ocean waves' space-time fields. *Computers & Geosciences*, 147:104666, 2021.

E. M. Bitner-Gregersen and Ø. Hagen. Uncertainties in data for the offshore environment. *Structural Safety*, 7(1):11–34, 1990.

E. M. Bitner-Gregersen and A. K. Magnusson. Effect of intrinsic and sampling variability on wave parameters and wave statistics. *Ocean Dynamics*, 64(11):1643–1655, 2014.

J.-V. Björkqvist, H. Pettersson, W. M. Drennan, and K. K. Kahma. A new inverse phase speed spectrum of nonlinear gravity wind waves. *Journal of Geophysical Research: Oceans*, 124(8):6097–6119, 2019.

P. Boccotti. *Wave mechanics for ocean engineering*. Elsevier, 2000.

P. Bohlinger, Ø. Breivik, T. Economou, and M. Müller. A novel approach to computing super observations for probabilistic wave model validation. *Ocean Modelling*, 139: 101404, 2019.

Ø. Breivik, A. Carrasco, H. Haakenstad, O. J. Aarnes, A. Behrens, J.-R. Bidlot, J.-V. Björkqvist, P. Bohlinger, B. R. Furevik, and J. Staneva. The Impact of a Reduced High-Wind Charnock Parameter on Wave Growth With Application to the North Sea, the Norwegian Sea, and the Arctic Ocean. *Journal of Geophysical Research: Oceans*, 127(3):e2021JC018196, 2022.

S. E. Brumer, C. J. Zappa, I. M. Brooks, H. Tamura, S. M. Brown, B. W. Blomquist, C. W. Fairall, and A. Cifuentes-Lorenzen. Whitecap coverage dependence on wind and wave statistics as observed during SO GasEx and HiWinGS. *Journal of Physical Oceanography*, 47(9):2211–2235, 2017.

B. Buchner, G. Z. Forristall, K. Ewans, M. Christou, and J. Hennig. New Insights in Extreme Crest Height Distributions: A Summary of the 'CresT'JIP. In *International Conference on Offshore Mechanics and Arctic Engineering*, volume 44342, pages 589–604, 2011.

A. Callaghan, G. de Leeuw, L. Cohen, and C. D. O'Dowd. Relationship of oceanic whitecap coverage to wind speed and wind history. *Geophysical Research Letters*, 35 (23), 2008.

A. H. Callaghan and M. White. Automated processing of sea surface images for the determination of whitecap coverage. *Journal of Atmospheric and Oceanic Technology*, 26(2):383–394, 2009.

A. H. Callaghan, G. B. Deane, and M. D. Stokes. Laboratory air-entraining breaking waves: Imaging visible foam signatures to estimate energy dissipation. *Geophysical Research Letters*, 43(21):11–320, 2016.

A. D. Cattrell, M. Srokosz, B. I. Moat, and R. Marsh. Can rogue waves be predicted using characteristic wave parameters? *Journal of Geophysical Research: Oceans*, 123 (8):5624–5636, 2018.

L. Cavaleri, B. Fox-Kemper, and M. Hemer. Wind waves in the coupled climate system. *Bulletin of the American Meteorological Society*, 93(11):1651–1661, 2012.

M. Christou and K. Ewans. Field measurements of rogue water waves. *Journal of physical oceanography*, 44(9):2317–2335, 2014.

C. C. Craciunescu and M. Christou. Wave breaking energy dissipation in long-crested focused wave groups based on JONSWAP spectra. *Applied Ocean Research*, 99:102144, 2020.

G. De Leeuw, E. L. Andreas, M. D. Anguelova, C. W. Fairall, E. R. Lewis, C. O'Dowd, M. Schulz, and S. E. Schwartz. Production flux of sea spray aerosol. *Reviews of Geophysics*, 49(2), 2011.

L. Deike. Mass transfer at the ocean–atmosphere interface: The role of wave breaking, droplets, and bubbles. *Annual Review of Fluid Mechanics*, 54:191–224, 2022.

L. Deike and W. K. Melville. Gas transfer by breaking waves. *Geophysical Research Letters*, 45(19):10–482, 2018.

M. Derakhti, J. T. Kirby, M. L. Banner, S. T. Grilli, and J. Thomson. A unified breaking onset criterion for surface gravity water waves in arbitrary depth. *Journal of Geophysical Research: Oceans*, 125(7):e2019JC015886, 2020.

M. Donelan and W. J. Pierson. The sampling variability of estimates of spectra of wind-generated gravity waves. *Journal of Geophysical Research: Oceans*, 88(C7):4381–4392, 1983.

M. Donelan, M. S. Longuet-Higgins, and J. S. Turner. Periodicity in whitecaps. *Nature*, 239(5373):449–451, 1972.

M. A. Donelan and A. K. Magnusson. The role of meteorological focusing in generating rogue wave conditions. *A A*, 2(2):2, 2005.

M. A. Donelan and A. K. Magnusson. The making of the Andrea wave and other rogues. *Scientific reports*, 7(1):1–7, 2017.

M. A. Donelan, W. M. Drennan, and A. K. Magnusson. Nonstationary analysis of the directional properties of propagating waves. *Journal of Physical Oceanography*, 26(9): 1901–1914, 1996.

M. A. Donelan, A. V. Babanin, E. Sanina, and D. Chalikov. A comparison of methods for estimating directional spectra of surface waves. *Journal of Geophysical Research: Oceans*, 120(7):5040–5053, 2015.

V. A. Dulov, V. N. Kudryavtsev, and A. Bol'shakov. A field study of whitecap coverage and its modulations by energy containing surface waves. *Gas Transfer at Water Surfaces – Geophysical Monograph*, 127:187–192, 2002.

V. A. Dulov, A. E. Korinenko, V. N. Kudryavtsev, and V. V. Malinovsky. Modulation of wind-wave breaking by long surface waves. *Remote Sensing*, 13(14):2825, 2021.

K. Dysthe, H. E. Krogstad, and P. Müller. Oceanic rogue waves. *Annual Review of Fluid Mechanics*, 40:287–310, 2008.

F. Fedele. Space–time extremes in short-crested storm seas. *Journal of Physical Oceanography*, 42(9):1601–1615, 2012.

F. Fedele, A. Benetazzo, G. Gallego, P.-C. Shih, A. Yezzi, F. Barbariol, and F. Ardhuin. Space–time measurements of oceanic sea states. *Ocean Modelling*, 70:103–115, 2013.

F. Fedele, C. Lugni, and A. Chawla. The sinking of the El Faro: Predicting real world rogue waves during Hurricane Joaquin. *Scientific reports*, 7(1):1–15, 2017.

F. Fedele, M. L. Banner, and X. Barthelemy. Crest speeds of unsteady surface water waves. *Journal of Fluid Mechanics*, 899, 2020.

G. Z. Forristall. Wave crest distributions: Observations and second-order theory. *Journal of physical oceanography*, 30(8):1931–1943, 2000.

G. Z. Forristall, S. F. Barstow, H. E. Krogstad, M. Prevosto, P. H. Taylor, and P. S. Tromans. Wave crest sensor intercomparison study: an overview of WACSIS. *J. Offshore Mech. Arct. Eng.*, 126(1):26–34, 2004.

J. R. Gemmrich and L. Cicon. Generation mechanism and prediction of an observed extreme rogue wave. *Scientific Reports*, 12(1):1–10, 2022.

J. R. Gemmrich and D. M. Farmer. Near-surface turbulence in the presence of breaking waves. *Journal of Physical Oceanography*, 34(5):1067–1086, 2004.

J. R. Gemmrich and J. Thomson. Observations of the shape and group dynamics of rogue waves. *Geophysical Research Letters*, 44(4):1823–1830, 2017.

J. R. Gemmrich, M. L. Banner, and C. Garrett. Spectrally resolved energy dissipation rate and momentum flux of breaking waves. *Journal of Physical Oceanography*, 38(6): 1296–1312, 2008.

R. Gibson, M. Christou, and G. Feld. The statistics of wave height and crest elevation during the December 2012 storm in the North Sea. *Ocean Dynamics*, 64(9):1305–1317, 2014.

Y. Goda. The observed joint distribution of periods and heights of sea waves. *Coastal Engineering Proceedings*, (16):11–11, 1978.

D. G. Goring and V. I. Nikora. Despiking acoustic Doppler velocimeter data. *Journal of hydraulic engineering*, 128(1):117–126, 2002.

O. Gramstad, E. Bitner-Gregersen, Ø. Breivik, A. K. Magnusson, M. Reistad, and O. J. Aarnes. Analysis of rogue waves in North-Sea in-situ surface wave data. In *International Conference on Offshore Mechanics and Arctic Engineering*, volume 51227, page V003T02A005. American Society of Mechanical Engineers, 2018.

E. J. Gumbel. Statistics of Extremes. *Columbia University Press*, 1958.

H. Haakenstad, Ø. Breivik, M. Reistad, and O. J. Aarnes. NORA10EI: A revised regional atmosphere-wave hindcast for the North Sea, the Norwegian Sea and the Barents Sea. *International Journal of Climatology*, 40(10):4347–4373, 2020.

H. Haakenstad, Ø. Breivik, B. R. Furevik, M. Reistad, P. Bohlinger, and O. J. Aarnes. NORA3: A nonhydrostatic high-resolution hindcast of the North Sea, the Norwegian Sea, and the Barents Sea. *Journal of Applied Meteorology and Climatology*, 60(10): 1443–1464, 2021.

D. Häfner, J. R. Gemmrich, and M. Jochum. FOWD: A free ocean wave dataset for data mining and machine learning. *Journal of Atmospheric and Oceanic Technology*, 38(7):1305–1322, 2021a.

D. Häfner, J. R. Gemmrich, and M. Jochum. Real-world rogue wave probabilities. *Scientific Reports*, 11(1):1–11, 2021b.

T. J. Hanisch and G. Nerheim. *Norsk oljehistorie: fra vantro til overmot?* Leseselskapet, 1992.

N. Hashimoto, T. Nagai, and T. Asai. Extension of the maximum entropy principle method for directional wave spectrum estimation. *Coastal Engineering Proceedings*, (24), 1994.

K. Hasselmann. On the non-linear energy transfer in a gravity-wave spectrum Part 1. General theory. *Journal of Fluid Mechanics*, 12(4):481–500, 1962.

K. Hasselmann, T. P. Barnett, E. Bouws, H. Carlson, D. E. Cartwright, K. Enke, J. A. Ewing, A. Gienapp, D. E. Hasselmann, and P. Kruseman. Measurements of wind-wave growth and swell decay during the Joint North Sea Wave Project (JONSWAP). *Ergaenzungsheft zur Deutschen Hydrographischen Zeitschrift, Reihe A*, 1973.

O. Haug. *A numerical model for prediction of sea and swell.* Norske Meteorologiske Institutt, 1968.

S. Haver. A possible freak wave event measured at the Draupner Jacket January 1 1995. In *Rogue waves*, volume 2004, pages 1–8, 2004.

J. Heikkilä and O. Silvén. A four-step camera calibration procedure with implicit image correction. In *Proceedings of IEEE computer society conference on computer vision and pattern recognition*, pages 1106–1112. IEEE, 1997.

T. H. C. Herbers, P. F. Jessen, T. T. Janssen, D. B. Colbert, and J. H. MacMahan. Observing ocean surface waves with GPS-tracked buoys. *Journal of Atmospheric and Oceanic Technology*, 29(7):944–959, 2012.

L. H. Holthuijsen. Observations of the directional distribution of ocean-wave energy in fetch-limited conditions. *Journal of Physical Oceanography*, 13(2):191–207, 1983.

L. H. Holthuijsen. *Waves in oceanic and coastal waters.* Cambridge university press, 2007.

L. H. Holthuijsen and T. H. C. Herbers. Statistics of breaking waves observed as whitecaps in the open sea. *Journal of Physical Oceanography*, 16(2):290–297, 1986.

P. A. E. M. Janssen. Nonlinear four-wave interactions and freak waves. *Journal of Physical Oceanography*, 33(4):863–884, 2003.

A. T. Jessup, C. J. Zappa, and H. Yeh. Defining and quantifying microscale wave breaking with infrared imagery. *Journal of Geophysical Research: Oceans*, 102(C10): 23145–23153, 1997.

K. K. Kahma and C. J. Calkoen. Reconciling discrepancies in the observed growth of wind-generated waves. *Journal of Physical Oceanography*, 22(12):1389–1405, 1992.

I. Karmpadakis, C. Swan, and M. Christou. Laboratory investigation of crest height statistics in intermediate water depths. *Proceedings of the Royal Society A*, 475(2229): 20190183, 2019.

A. Kimura. Statistical properties of random wave groups. *Coastal Engineering Proceedings*, (17):175–175, 1980.

B. Kinsman. *Wind waves: their generation and propagation on the ocean surface*. Prentice-Hall, 1965.

S. A. Kitaigordskii, V. P. Krasitskii, and M. M. Zaslavskii. On Phillips' theory of equilibrium range in the spectra of wind-generated gravity waves. *Journal of Physical Oceanography*, 5(3):410–420, 1975.

J. M. Kleiss and W. K. Melville. Observations of wave breaking kinematics in fetch-limited seas. *Journal of Physical Oceanography*, 40(12):2575–2604, 2010.

J. M. Kleiss and W. K. Melville. The analysis of sea surface imagery for whitecap kinematics. *Journal of Atmospheric and Oceanic Technology*, 28(2):219–243, 2011.

R. Klette, A. Koschan, and K. Schluns. Three-dimensional data from images. *Springer-Verlag Singapore Pte. Ltd., Singapore*, 1998.

G. J. Komen, L. Cavaleri, M. A. Donelan, K. Hasselmann, S. Hasselmann, and P. A. E. M. Janssen. *Dynamics and modelling of ocean waves*. 1994.

H. E. Krogstad, J. Liu, H. Socquet-Juglard, K. B. Dysthe, and K. Trulsen. Spatial extreme value analysis of nonlinear simulations of random surface waves. In *International Conference on Offshore Mechanics and Arctic Engineering*, volume 37440, pages 285–295, 2004.

A. J. Kuik, G. P. Van Vledder, and L. H. Holthuijsen. A method for the routine analysis of pitch-and-roll buoy wave data. *Journal of physical oceanography*, 18(7):1020–1034, 1988.

H. Lamb. *Hydrodynamics*. Cambridge university press, 1932.

M. Latheef and C. Swan. A laboratory study of wave crest statistics and the role of directional spreading. *Proceedings of the Royal Society A: Mathematical, Physical and Engineering Sciences*, 469(2152):20120696, 2013.

L. Lenain and W. K. Melville. Measurements of the directional spectrum across the equilibrium saturation ranges of wind-generated surface waves. *Journal of Physical Oceanography*, 47(8):2123–2138, 2017.

Q. Li, B. G. Reichl, B. Fox-Kemper, A. J. Adcroft, S. E. Belcher, G. Danabasoglu, A. L. M. Grant, S. M. Griffies, R. Hallberg, and T. Hara. Comparing ocean surface boundary vertical mixing schemes including Langmuir turbulence. *Journal of Advances in Modeling Earth Systems*, 11(11):3545–3592, 2019.

G. Lian and S. K. Haver. Measured crest height distribution compared to second order distribution. In *Proceedings of the 14th International Workshop on Wave Hindcasting and Forecasting, Key West, Florida, USA*, 2015.

M. J. Lighthill. Contributions to the theory of waves in non-linear dispersive systems. *IMA Journal of Applied Mathematics*, 1(3):269–306, 1965.

M. S. Longuet-Higgins. On the statistical distribution of the heights of sea waves. *Journal of Marine Research*, 11:245–266, 1952.

M. S. Longuet-Higgins. The effect of non-linearities on statistical distributions in the theory of sea waves. *Journal of fluid mechanics*, 17(3):459–480, 1963.

M. S. Longuet-Higgins. On the joint distribution of the periods and amplitudes of sea waves. *Journal of Geophysical Research*, 80(18):2688–2694, 1975.

M. S. Longuet-Higgins. On the distribution of the heights of sea waves: Some effects of nonlinearity and finite band width. *Journal of Geophysical Research: Oceans*, 85(C3): 1519–1523, 1980.

M. S. Longuet-Higgins and R. W. Stewart. Changes in the form of short gravity waves on long waves and tidal currents. *Journal of Fluid Mechanics*, 8(4):565–583, 1960.

A. Lygre and H. E. Krogstad. Maximum entropy estimation of the directional distribution in ocean wave spectra. *Journal of Physical Oceanography*, 16(12):2052–2060, 1986.

A. K. Magnusson and M. A. Donelan. The Andrea wave characteristics of a measured North Sea rogue wave. *Journal of Offshore Mechanics and Arctic Engineering*, 135(3), 2013.

A. K. Magnusson, M. Olagnon, and M. Prevosto. Forecasting extreme waves in practice. In *Proceedings of the Rogue Waves 2008 Workshop, edited by: Olagnon, M. and Prevosto, M., Brest, France*, pages 1–15, 2008.

M. P. Malila, P. Bohlinger, S. Støle-Hentschel, Ø. Breivik, G. Hope, and A. K. Magnusson. A Nonparametric, Data-Driven Approach to Despiking Ocean Surface Wave Time Series. *Journal of Atmospheric and Oceanic Technology*, 39(1):71–90, 2022a. doi: 10.1175/JTECH-D-21-0067.1.

M. P. Malila, J. Thomson, Ø. Breivik, A. Benetazzo, B. Scanlon, and B. Ward. On the groupiness and intermittency of oceanic whitecaps. *Journal of Geophysical Research: Oceans*, 127(1):e2021JC017938, 2022b. doi: 10.1029/2021JC017938.

M. P. Malila, F. Barbariol, A. Benetazzo, Ø. Breivik, A. K. Magnusson, J. Thomson, and B. Ward. Statistical and dynamical characteristics of extreme wave crests assessed with field measurements from the North Sea. *Submitted to Journal of Physical Oceanography*, under review 2022.

W. K. Melville. The instability and breaking of deep-water waves. *Journal of Fluid Mechanics*, 115:165–185, 1982.

W. K. Melville. The role of surface-wave breaking in air-sea interaction. *Annual Review of Fluid Mechanics*, 28:279–321, 1996.

M. Miche. Mouvements ondulatoires de la mer en profondeur constante ou décroissante. *Annales de Ponts et Chaussées, 1944, pp (1) 26-78,(2) 270-292,(3) 369-406*, 1944.

J. H. Michell. On the highest waves in water. *The London, Edinburgh, and Dublin Philosophical Magazine and Journal of Science*, 36(222):430–437, 1893.

J. W. Miles. On the generation of surface waves by shear flows. *Journal of Fluid Mechanics*, 3(2):185–204, 1957.

T. Moan. The progressive structural failure of the Alexander L. Kielland platform. In *Case Histories in Offshore Engineering*, pages 1–42. Springer, 1985.

E. C. Monahan. Oceanic whitecaps. *Journal of Physical Oceanography*, 1(2):139–144, 1971.

E. C. Monahan and I. Muircheartaigh. Optimal power-law description of oceanic whitecap coverage dependence on wind speed. *Journal of Physical Oceanography*, 10(12): 2094–2099, 1980.

N. Mori and P. A. E. M. Janssen. On kurtosis and occurrence probability of freak waves. *Journal of Physical Oceanography*, 36(7):1471–1483, 2006.

N. Mori, T. Suzuki, and S. Kakuno. Noise of acoustic Doppler velocimeter data in bubbly flows. *Journal of engineering mechanics*, 133(1):122–125, 2007.

M. Olagnon. *Rogue waves: anatomy of a monster*. Bloomsbury Publishing, 2017.

M. Perlin, J. He, and L. P. Bernal. An experimental study of deep water plunging breakers. *Physics of fluids*, 8(9):2365–2374, 1996.

M. Perlin, W. Choi, and Z. Tian. Breaking waves in deep and intermediate waters. *Annual review of fluid mechanics*, 45:115–145, 2013.

O. M. Phillips. On the generation of waves by turbulent wind. *Journal of fluid mechanics*, 2(5):417–445, 1957.

O. M. Phillips. The equilibrium range in the spectrum of wind-generated waves. *Journal of Fluid Mechanics*, 4(4):426–434, 1958.

O. M. Phillips. *The Dynamics of the Upper Ocean*. Cambridge UP, 1977.

O. M. Phillips. Spectral and statistical properties of the equilibrium range in wind-generated gravity waves. *Journal of Fluid Mechanics*, 156:505–531, 1985.

W. J. Pierson and L. Moskowitz. A proposed spectral form for fully developed wind seas based on the similarity theory of SA Kitaigorodskii. *Journal of geophysical research*, 69(24):5181–5190, 1964.

V. I. Piterbarg. *Asymptotic methods in the theory of Gaussian processes and fields*, volume 148. American Mathematical Soc., 1996.

N. Pizzo and W. K. Melville. Focusing deep-water surface gravity wave packets: wave breaking criterion in a simplified model. *Journal of Fluid Mechanics*, 873:238–259, 2019.

R. J. Rapp and W. K. Melville. Laboratory measurements of deep-water breaking waves. *Philosophical Transactions of the Royal Society of London. Series A, Mathematical and Physical Sciences*, 331(1622):735–800, 1990.

L. Rayleigh. On the resultant of a large number of vibrations of the same pitch and of arbitrary phase. *The London, Edinburgh, and Dublin Philosophical Magazine and Journal of Science*, 10(60):73–78, 1880.

K. Reichert, K. Hessner, J. C. Nieto Borge, and J. Dittmer. WaMoS II: A radar based wave and current monitoring system. In *The Ninth International Offshore and Polar Engineering Conference*. OnePetro, 1999.

B. D. Reineman, L. Lenain, D. Castel, and W. K. Melville. A portable airborne scanning lidar system for ocean and coastal applications. *Journal of Atmospheric and oceanic technology*, 26(12):2626–2641, 2009.

L. Romero. Distribution of surface wave breaking fronts. *Geophysical Research Letters*, 46(17-18):10463–10474, 2019.

A. Saket, W. L. Peirson, M. L. Banner, X. Barthelemy, and M. J. Allis. On the threshold for wave breaking of two-dimensional deep water wave groups in the absence and presence of wind. *Journal of Fluid Mechanics*, 811:642–658, 2017.

B. Scanlon and B. Ward. Oceanic wave breaking coverage separation techniques for active and maturing whitecaps. *Methods in Oceanography*, 8:1–12, 2013.

B. Scanlon and B. Ward. The influence of environmental parameters on active and maturing oceanic whitecaps. *Journal of Geophysical Research: Oceans*, 121(5):3325–3336, 2016.

M. Schwendeman and J. Thomson. Observations of whitecap coverage and the relation to wind stress, wave slope, and turbulent dissipation. *Journal of Geophysical Research: Oceans*, 120(12):8346–8363, 2015.

M. Schwendeman, J. Thomson, and J. R. Gemmrich. Wave breaking dissipation in a young wind sea. *Journal of Physical Oceanography*, 44(1):104–127, 2014.

M. S. Schwendeman and J. Thomson. Sharp-crested breaking surface waves observed from a ship-based stereo video system. *Journal of Physical Oceanography*, 47(4):775–792, 2017.

B. R. Seiffert, G. Ducrozet, and F. Bonnefoy. Simulation of breaking waves using the high-order spectral method with laboratory experiments: Wave-breaking onset. *Ocean Modelling*, 119:94–104, 2017.

M. Serio, M. Onorato, A. R. Osborne, and P. A. E. M. Janssen. On the computation of the Benjamin-Feir Index. *Il nuovo cimento C*, 28(6):893–903, 2005.

J. N. Sharma and R. G. Dean. Second-order directional seas and associated wave forces. *Society of Petroleum Engineers Journal*, 21(01):129–140, 1981.

M. J. Smith, E. M. Poulter, and J. A. McGregor. Doppler radar measurements of wave groups and breaking waves. *Journal of Geophysical Research: Oceans*, 101(C6):14269–14282, 1996.

J.-B. Song and M. L. Banner. On determining the onset and strength of breaking for deep water waves. Part I: Unforced irrotational wave groups. *Journal of Physical Oceanography*, 32(9):2541–2558, 2002.

K. R. Sreenivasan and A. Bershadskii. Clustering properties in turbulent signals. *Journal of statistical physics*, 125(5):1141–1153, 2006.

G. G. Stokes. On the theory of oscillatory waves. *Trans. Camb. Phil. Soc.*, 8:411–455, 1847.

G. G. Stokes. Considerations relative to the greatest height of oscillatory irrotational waves which can be propagated without change of form. *Mathematical and physical papers*, 1:225–228, 1880.

S. Støle-Hentschel, J. Seemann, J. C. Nieto Borge, and K. Trulsen. Consistency between sea surface reconstructions from nautical X-band radar Doppler and amplitude measurements. *Journal of Atmospheric and Oceanic Technology*, 35(6):1201–1220, 2018.

C. E. Stringari, M. Prevosto, J.-F. Filipot, F. Leckler, and P. V. Guimarães. A New Probabilistic Wave Breaking Model for Dominant Wind-Sea Waves Based on the Gaussian Field Theory. *Journal of Geophysical Research: Oceans*, 126(4):e2020JC016943, 2021.

R. M. Sulak. Ekofisk field: the first 20 years. *Journal of Petroleum Technology*, 43(10): 1265–1271, 1991.

P. P. Sullivan and J. C. McWilliams. Dynamics of winds and currents coupled to surface waves. *Annual Review of Fluid Mechanics*, 42:19–42, 2010.

P. Sutherland and W. K. Melville. Field measurements and scaling of ocean surface wave-breaking statistics. *Geophysical Research Letters*, 40(12):3074–3079, 2013.

R. Szeliski. *Computer vision: algorithms and applications*. Springer Science & Business Media, 2010.

M. A. Tayfun. Narrow-band nonlinear sea waves. *Journal of Geophysical Research: Oceans*, 85(C3):1548–1552, 1980.

M. A. Tayfun and F. Fedele. Wave-height distributions and nonlinear effects. *Ocean engineering*, 34(11-12):1631–1649, 2007.

J. Thomson. Wave breaking dissipation observed with "SWIFT" drifters. *Journal of Atmospheric and Oceanic Technology*, 29(12):1866–1882, 2012.

J. Thomson, M. S. Schwendeman, S. F. Zippel, S. Moghimi, J. Gemmrich, and W. E. Rogers. Wave-breaking turbulence in the ocean surface layer. *Journal of Physical Oceanography*, 46(6):1857–1870, 2016.

A. Toffoli, A. Babanin, M. Onorato, and T. Waseda. Maximum steepness of oceanic waves: Field and laboratory experiments. *Geophysical Research Letters*, 37(5), 2010.

A. Toffoli, A. V. Babanin, M. A. Donelan, B. K. Haus, and D. Jeong. Estimating sea spray volume with a laser altimeter. *Journal of atmospheric and oceanic technology*, 28(9):1177–1183, 2011.

K. Trulsen. Weakly nonlinear and stochastic properties of ocean wave fields. Application to an extreme wave event. In *Waves in Geophysical Fluids*, pages 49–106. Springer, 2006.

K. Trulsen and K. B. Dysthe. A modified nonlinear Schrödinger equation for broader bandwidth gravity waves on deep water. *Wave motion*, 24(3):281–289, 1996.

M. Vieira, P. V. Guimarães, N. Violante-Carvalho, A. Benetazzo, F. Bergamasco, and H. Pereira. A low-cost stereo video system for measuring directional wind waves. *Journal of Marine Science and Engineering*, 8(11):831, 2020.

C. L. Vincent, J. Thomson, H. C. Graber, and C. O. Collins III. Impact of swell on the wind-sea and resulting modulation of stress. *Progress in oceanography*, 178:102164, 2019.

J. J. Voermans, A. V. Babanin, C. Kirezci, J. T. Carvalho, M. F. Santini, B. F. Pavani, and L. P. Pezzi. Wave anomaly detection in wave measurements. *Journal of Atmospheric and Oceanic Technology*, 38(3):525–536, 2021.

T. L. Wahl. Discussion of "Despiking acoustic doppler velocimeter data" by Derek G. Goring and Vladimir I. Nikora. *Journal of Hydraulic Engineering*, 129(6):484–487, 2003.

P. Welch. The use of fast Fourier transform for the estimation of power spectra: a method based on time averaging over short, modified periodograms. *IEEE Transactions on audio and electroacoustics*, 15(2):70–73, 1967.

D. K. Woolf. Bubbles and their role in gas exchange. In *The sea surface and global change*, pages 173–206. Cambridge University Press, 1997.

V. E. Zakharov and L. A. Ostrovsky. Modulation instability: the beginning. *Physica D: Nonlinear Phenomena*, 238(5):540–548, 2009.

C. J. Zappa, M. L. Banner, H. Schultz, A. Corrada-Emmanuel, L. B. Wolff, and J. Yalcin. Retrieval of short ocean wave slope using polarimetric imaging. *Measurement Science and Technology*, 19(5):055503, 2008.

S. Zippel and J. Thomson. Surface wave breaking over sheared currents: Observations from the Mouth of the Columbia River. *Journal of Geophysical Research: Oceans*, 122 (4):3311–3328, 2017.

Chapter 6

Scientific results

Article I

6.1 A Nonparametric, Data-Driven Approach to Despiking Ocean Surface Wave Time Series

Mika P. Malila, Patrik Bohlinger, Susanne Støle-Hentschel, Øyvind Breivik, Gaute Hope and Anne Karin Magnusson.

Journal of Atmospheric and Oceanic Technology, **39**(1), 71–90, doi:10.1175/JTECH-D-21-0067.1 (2022)

A Nonparametric, Data-Driven Approach to Despiking Ocean Surface Wave Time Series

MIKA P. MALILA,[a,b] PATRIK BOHLINGER,[a] SUSANNE STØLE-HENTSCHEL,[c] ØYVIND BREIVIK,[a,b] GAUTE HOPE,[a] AND ANNE KARIN MAGNUSSON[a]

[a] *Norwegian Meteorological Institute, Bergen, Norway*
[b] *Geophysical Institute, University of Bergen, Bergen, Norway*
[c] *School of Mechanical Engineering, Tel Aviv University, Tel Aviv, Israel*

(Manuscript received 21 May 2021, in final form 21 September 2021)

ABSTRACT: We propose a methodology for despiking ocean surface wave time series based on a Bayesian approach to data-driven learning known as Gaussian process (GP) regression. We show that GP regression can be used for both robust detection of erroneous measurements and interpolation over missing values, while also obtaining a measure of the uncertainty associated with these operations. In comparison with a recent dynamical phase space–based despiking method, our data-driven approach is here shown to lead to improved wave signal correlation and spectral tail consistency, although at a significant increase in computational cost. Our results suggest that GP regression is thus especially suited for offline quality control requiring robust noise detection and replacement, where the subsequent analysis of the despiked data is sensitive to the accidental removal of extreme or rare events such as abnormal or rogue waves. We assess our methodology on measurements from an array of four collocated 5-Hz laser altimeters during a much-studied storm event in the North Sea covering a wide range of sea states.

KEYWORDS: In situ oceanic observations; Instrumentation/sensors; Quality assurance/control; Bayesian methods; Uncertainty

1. Introduction

In situ instruments capable of measuring time series of the instantaneous sea surface displacement, such as wave buoys, wave staffs, and laser altimeters, are routinely used for validating and assessing the performance of spectral wave model forecasts and hindcasts (e.g., Cox and Swail 2001; Chawla et al. 2013; Haakenstad et al. 2020). Such *phase-resolving* wave measurements are also often used for investigating the statistical distributions of extreme wave heights, the understanding of which is vital to conducting safe offshore operations (e.g., Dysthe et al. 2008; Christou and Ewans 2014). Unless filtered by built-in software, raw sea surface displacement time series are often corrupted by noise in the form of spikes, dropouts, lock-ins, and other artifacts due to, e.g., instrument malfunction or environmental effects (see, e.g., Voermans et al. 2021). It is known that noise-corrupted measurements may lead to spurious effects on estimated energy spectra, which in turn may skew integrated wave-field parameters used for model validation (Magnusson et al. 2021; Thomson et al. 2021). *Despiking*, the process of detecting, removing, and replacing measurement errors, is therefore an essential step in the initial quality control of wave measurement time series. However, especially if the phenomena of interest are extreme or rare events (e.g., exceptionally steep or high waves relative to the prevailing sea state), care must be taken not to remove valid measurements which often get flagged as outliers by automated despiking algorithms (Dysthe et al. 2008; Starkenburg et al. 2016; Häfner et al. 2021).

A basic despiking method detects erroneous measurements on the basis of a global threshold derived from the raw time series. For surface wave records, a commonly applied global threshold [see, e.g., Thomas 2016; Integrated Ocean Observing System (IOOS); IOOS 2019] is some multiple of the significant wave height

$$H_s = 4\sigma, \tag{1}$$

where σ is the standard deviation of the wave signal. However, if one is interested in the extreme wave or crest height statistics of the wave records, the global threshold must be set higher than the highest physically possible wave crest for the prevailing sea state to avoid the accidental removal of valid measurement points (e.g., Dysthe et al. 2008). Consequently, the utility of the global threshold method is limited to removing only large-amplitude spikes, and has restricted applicability for automated despiking of surface wave records. For this reason, the global threshold method is commonly combined with manual inspection of suspicious measurements (Makri et al. 2016; Cattrell et al. 2018; IOOS 2019). However, as the amount of data to control grows large, and especially if the noise corruption is extensive, manual inspection becomes labor-intensive and susceptible to human error. The subjectivity of manual inspection also raises the issue of reproducibility. Thus, while it is unlikely that manual inspection can be fully replaced by automated methods, it can be argued that quality control measures such as despiking can be made more objective and consistent by minimizing the need for human intervention (Thomas 2016).

A conventional premise for automated despiking of fluid mechanical time series builds on the assumption that the

Corresponding author: Mika P. Malila, mikapm@met.no

DOI: 10.1175/JTECH-D-21-0067.1

dynamical properties of the flow, such as fluid particle speed and acceleration, form a predictable pattern in phase space. Goring and Nikora (2002) originally introduced a despiking algorithm for acoustic Doppler velocimeter (ADV) measurements of turbulent flow in a channel, in which the phase space was defined in terms of the fluid velocity and its first and second derivatives. Spikes were defined as measurement points whose phase space properties placed them on the outside of two-dimensional ellipses, the shapes of which were determined by the theoretical maxima of normally distributed flow properties. The stepwise phase space thresholding procedure of Goring and Nikora (2002) was streamlined into a single three-dimensional thresholding operation by Wahl (2003), who also emphasized the issue of the nonrobustness of applying thresholds based on the normal distribution (typically defined in terms of, e.g., the mean and standard deviation of the flow variables) to measurement error-contaminated, possibly highly non-Gaussian time series. As Wahl (2003) points out, the sample mean and standard deviation are extremely sensitive to outliers, and therefore any despiking threshold based on these estimators is likely to be influenced by the presence of undesired, faulty measurements in the dataset. Wahl (2003) thus suggests replacing the sample mean and standard deviation with robust estimators that are comparatively insensitive to outliers, such as the sample median and median of the absolute deviations (MAD).

Recently, Voermans et al. (2021) reformulated the phase space despiking framework to apply to surface wave time series by defining the phase space in terms of wave physics. In their formulation, Voermans et al. (2021) argue that the relevant phase space parameters for surface waves are the instantaneous surface displacement $\eta(t)$ and its acceleration $\partial^2\eta/\partial t^2$. They define the phase space ellipse that encloses valid measurements in terms of key sea state properties, namely, the wave period and the bandwidth of the wave energy spectrum. Voermans et al. (2021) also highlight the important distinction between despiking and anomaly detection, where the former refers to the identification (and, commonly, replacement) of spikes that contaminate the high-frequency tail of the energy spectrum, and the latter involves identifying longer-duration erroneous events in the time series that typically affect the low-frequency region of the spectrum. While spikes lasting from one to a few consecutive sampling intervals can be relatively straightforward to replace by interpolation, the removal of larger chunks of wave records due to anomalous, long-duration events requires careful consideration of whether to repair or discard the data. Wave record error characteristics tend to vary with instrument type, with single or multipoint spikes commonly produced by range-measuring instruments such as laser altimeters, while wave buoy records more typically exhibit complex anomalous events attributable to, e.g., mooring line interference (Dysthe et al. 2008; Thomas 2016; IOOS 2019; Voermans et al. 2021).

In this paper, we present a robust approach to both detecting and replacing spikes and dropouts in point-measurement time series of surface wave elevation. Our approach is based on Gaussian process (GP) regression, which, in contrast to the dynamically based phase space methods described earlier, is a data-driven, nonparametric, and probabilistic method designed for optimized functional fitting conditional on empirical input data (Rasmussen and Williams 2006). GP regression has in the last decade grown in popularity within marine and geophysical applications. Bohlinger et al. (2019) recently introduced a GP-based approach to the alignment of satellite altimeter observations of the sea state with numerical wave model output, taking advantage of the intrinsic uncertainty quantification of the GP framework to both detect erroneous data points and provide probabilistic model validation statistics. In another recent effort, Smith et al. (2014) coupled GP regression with extreme value theory to produce a robust dynamical model for the automatic detection of anomalous ship GPS tracks.

The remainder of this paper is structured as follows. We describe the test dataset, a 36-h record of 5-Hz laser altimeter surface wave measurements from the Ekofisk field in the central North Sea, in section 2. In section 3 we introduce the basics behind standard GP regression and motivate our application of the method for despiking surface wave time series with the use of examples from the Ekofisk laser altimeter dataset. In section 4 we demonstrate the performance of the GP-based despiking method outlined in section 3 on the full Ekofisk dataset. Section 5 discusses the advantages and limitations of the method in broader terms, and section 6 summarizes the work presented herein. Finally, a sample algorithm is provided in the appendix which outlines our implementation of the GP framework for spike detection.

2. The field dataset

We demonstrate and validate our proposed despiking method with real field measurements of surface waves from an array of laser altimeters placed on the ConocoPhillips Norway–operated Ekofisk oil and gas field in the central North Sea, the approximate location of which is shown in Fig. 1a. The laser altimeter array consists of four Optech Sentinel 3100 laser altimeters arranged in a 2.6-m square array inside a footbridge connecting two bottom-mounted platforms approximately 20 m above mean sea level (see Krogstad et al. 2006, 2008; Magnusson and Donelan 2013; Donelan and Magnusson 2017). The footbridge on which the laser altimeters are situated, depicted in Fig. 1c, is oriented approximately east-northeast–west-southwest, with a 69° compass heading between the axis of the footbridge and north, allowing waves approaching from the northwest to be measured free from platform interference.

The laser altimeters measure the distance to the instantaneous sea surface by emitting and receiving reflected infrared pulses at 2-kHz temporal resolution. To avoid interference, the four laser altimeters are designed to fire pulses in a staggered sequence at 45-ms intervals. Herein we label the laser altimeters with numbers from 1 to 4 according to the order in which they sample. While important to consider if using the laser array to investigate, e.g., wave-field directionality (e.g., Donelan et al. 1996), for this work the ordering has no practical implications. The reflected and received pulses are averaged by built-in processing into range readings at 0.2-s

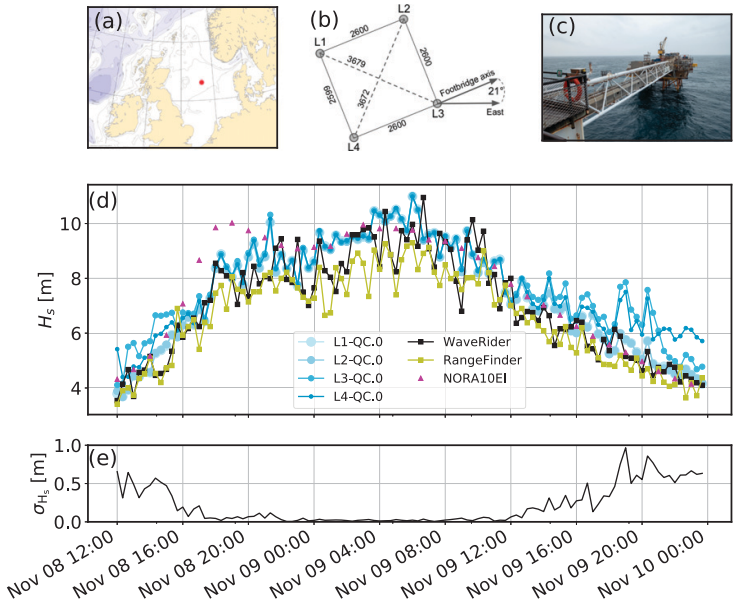

FIG. 1. (a) The location of the Ekofisk field in the central North Sea marked with a red dot. (b) Sketch of the dimensions and orientation of the four-laser altimeter array located on the footbridge connecting the Ekofisk K and B platforms. The distances between the lasers (L1–L4) are given in mm, based on measurements reported by Krogstad (2006). (c) Photo from 2019 of the footbridge that houses the laser altimeter array, looking southwest toward the B platform. (d) Time series of significant wave height H_s over the duration of the 8–9 Nov 2007 storm at the Ekofisk field. The connected blue-hued circles represent H_s computed from the standard deviations of the four QC.0-level laser altimeter time series. The connected squares are bulk H_s values recorded by two separate wave sensors at Ekofisk, namely, a Datawell Waverider buoy (black) and a Miros range finder radar (green). The disconnected purple triangles are hourly NORA10EI hindcast estimates of H_s at the model grid point nearest to the Ekofisk field. (e) The time series of standard deviations of the four concurrent H_s estimates from the QC.0-level laser altimeter records.

intervals, leading to an end product in the form of raw range time series at 5-Hz temporal resolution. These range time series z_i can be converted to sea surface displacement measurements η_i by

$$\eta_i = \overline{z} - z_i, \tag{2}$$

where $\overline{z}$ is the time average of z_i over a representative time window (taken here as 20 min to ensure stationary wave conditions). The intrinsic laser altimeter processing has a threshold on the number of good (i.e., high signal intensity) return pulses received within each sampling interval, and unless this threshold is exceeded the range reading is set to zero in final 5-Hz product. In our experience, such *dropouts* typically occur in relatively calm sea states during which the laser pulses may be more prone to specular reflections from the sea surface than during more energetic sea states, which tend to produce a rougher sea surface and enhanced reflected pulse intensity. However, the short wavelength of the infrared pulses (on the order of 1 μm) makes signal attenuation by the presence of sea spray aerosols of comparable size to the laser pulses another factor that may negatively impact the return intensity, occasionally leading to considerable numbers of dropouts also in rough seas (see, e.g., Toffoli et al. 2011).

The laser altimeter signals are also regularly corrupted by apparently erroneous range measurements, which manifest as spikes in the η_i signals. The spikes in the Ekofisk laser altimeter signals are generally high-frequency artifacts that persist for one to several consecutive sampling intervals; more prolonged anomalous measurements, such as the anomalous waves reported by Voermans et al. (2021) in their wave buoy records, are in our experience uncommon in the Ekofisk laser altimeter measurements. As discussed in section 1, spikes that indisputably result from instrumentation error, i.e., unphysically high or low η_i measurements, can be safely removed from the dataset with a constant global threshold, so long as the applied threshold is sufficiently conservative. For surface wave time series it is commonplace to define the global threshold as a multiple of the significant wave height H_s, defined in terms of the signal standard deviation (e.g., IOOS 2019). However, the sample mean and standard deviation are

known to be unstable estimates of location and scale of noise-corrupted time series, as one single anomalous measurement (e.g., a high-amplitude spike) can result in considerable biases in these estimates (e.g., Donoho and Huber 1983). A more robust approach involves replacing the mean and standard deviation with the sample median med$\{\eta_i\}$ and the MAD, defined as

$$\mathrm{MAD}(\eta_i) = 1.483\ \mathrm{med}\{|\eta_i - \mathrm{med}\{\eta_i\}|\}, \tag{3}$$

where the scale factor 1.483 stems from the reciprocal of the cumulative distribution of the Gaussian distribution, and ensures that the MAD estimate asymptotically converges to the Gaussian standard deviation (see, e.g., Huber 1981, p. 108).

The test dataset in this paper covers a 36-h storm event on 8–9 November 2007, during which each of the four Ekofisk laser altimeters was recording continuously at a 5-Hz sampling rate. This event was chosen because it comprises a wide range of sea states, with young, rapidly developing seas in the first 6 h, followed by a roughly 14-h period of consistently high waves during the peak of the storm, and finally a 16-h gradually aging sea state. The winds during the storm event were northwesterly and sustained at approximately 20 m s^{-1} from 1200 UTC 8 November until 0600 UTC 9 November (see Magnusson and Donelan 2013). The evolution of the significant wave height H_s, estimated independently from sequential 20-min segments of each of the four 5-Hz laser altimeter time series, is shown in Fig. 1c alongside H_s estimates from nearby wave buoy and radar rangefinder measurements as well as wave model hindcast results. The laser altimeter H_s estimates in Fig. 1c were computed using Eq. (1) from the raw laser altimeter records after prominent spikes had been removed with a 10MAD(η_i) global threshold above and below the record median. The 10MAD(η_i) threshold corresponds to a robust estimate of 2.5H_s, and we argue that this relatively conservative threshold is unlikely to lead to the removal of physically realistic wave crests or troughs—after all, the height of surface wave crests is known to be limited by wave geometry (viz., the wave steepness), and we are unaware of reliable field measurements containing individual crest heights exceeding approximately 1.7H_s (see, e.g., Toffoli et al. 2010; Donelan and Magnusson 2017). Hereinafter, we refer to raw laser altimeter records that have undergone this global threshold–based quality control as QC.0-level wave records. The spread in H_s estimates derived from the four QC.0-level laser records, shown in Fig. 1d, is relatively high both during the beginning and end phases of the storm, whereas the H_s estimates converge during the peak of the storm between approximately 0000 and 1200 UTC 9 November. This indicates that the laser altimeter signals were more likely to be corrupted by noise such as spikes during the comparatively low sea states in the developing and decaying phases of the storm, whereas noise corruption was greatly reduced during the highly energetic peak phase of the storm.

The difference between filtering out prominent spikes with MAD-based thresholds versus the more common σ-based thresholds is illustrated in Fig. 2: while the value of the 10σ threshold increases with increasing magnitude of the noise

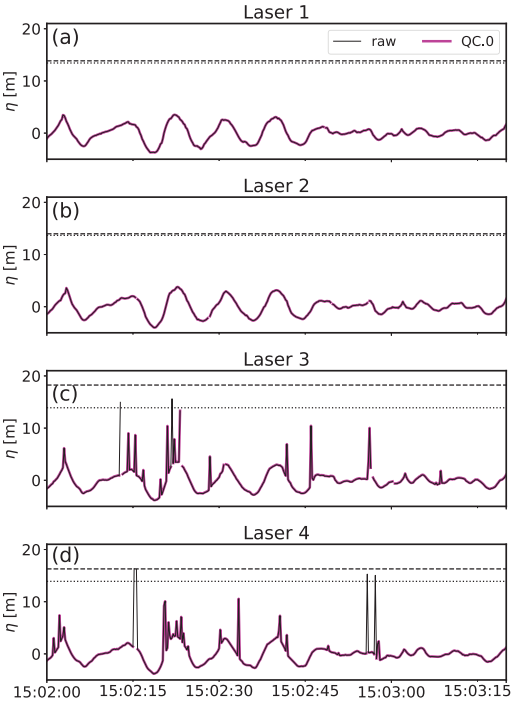

FIG. 2. Example segments of four concurrent laser records (laser 1–laser 4) from 8 Nov. The thin black lines are the raw laser measurements, and the thick magenta lines are the QC.0-level raw signals in which individual measurements above and below 10 MAD from the median (dotted line) have been removed. The 10σ threshold (dashed line) has been included for reference.

(Figs. 2c,d), leading to a failure of the threshold to detect the largest-amplitude spikes, the value of the 10MAD threshold is comparatively unaffected by the noise and manages to remove the highest-amplitude spikes in Figs. 2c and 2d. Figure 2 also clearly displays the varying noise characteristics between the four laser altimeters, with the signals from lasers 1 and 2 often relatively free of contamination by spikes and dropouts, while the signals of lasers 3 and 4 typically contain more frequent moderate and high-amplitude spikes and more numerous dropouts.

Notably, the 8–9 November 2007 storm at Ekofisk produced one of the most extreme individual waves on record—the approximately 22-m-high Andrea wave, named after its namesake storm (Magnusson and Donelan 2013; Donelan and Magnusson 2017). The Andrea wave occurred shortly after midnight on 9 November, and was measured with virtually identical shape by all four lasers, making it a rare occurrence of a verified *rogue* wave. The Andrea wave is included in our test dataset (see Figs. 8a and 12e), and its inclusion provides an appropriate sanity test for our proposed despiking method: while our aim is to develop a method that is able to robustly remove and replace

undesired spikes from the wave records (i.e., improve the laser array signal correlations at the beginning and end stages of the test dataset), we also require that real, verified extreme events such as the Andrea wave should be left untouched.

3. Despiking model description

a. GP regression

In this section we briefly summarize the basics of standard GP regression as applied to one-dimensional time series data, following Rasmussen and Williams (2006). GP regression is based on Bayesian formalism, in which *prior* assumptions of a system are combined with observations to infer a *posterior* probability of the state of the system in a predictive sense. In our case we seek to model the noisy output $y(t)$ of an underlying process measured at times t with a function $f(t)$ such that

$$y(t) = f(t) + \varepsilon_y, \tag{4}$$

where $\varepsilon_y \sim \mathcal{N}\left(0, \sigma_y^2\right)$ represents independent, normally distributed measurement noise with variance σ_y^2. Instead of providing one single function as the optimal model for the measurements, as in a polynomial fit, the GP framework considers a probability distribution of possible functions, not constrained by polynomial order, such that any finite collection of possible function values at a time t has a joint Gaussian distribution. A process with this property is by definition a Gaussian process, and is fully determined by its mean and covariance functions $\mu[f(t)]$ and $\mathrm{cov}[f(t)]$. We further assume that the covariation between function values is uniquely determined by their separation in time $s = |t_i - t_j|$, so that $\mathrm{cov}[f(t)] = k(s)$.

We choose to parameterize the *stationary* covariance function $k(s)$ in the form of a squared exponential

$$k_{\mathrm{SE}}(s) = \sigma_f^2 \exp\left(-\frac{s^2}{2l^2}\right), \tag{5}$$

where σ_f^2 is the signal variance and l is the so-called length scale parameter that controls the smoothness of the covariance function. The squared exponential covariance function is infinitely differentiable, which leads to smoothly varying regression functions in which the length scale parameter l determines the input-space distance over which subsequent function values are correlated. The covariance matrix can also be parameterized by various other functions with different characteristics from the squared exponential; see, e.g., Rasmussen and Williams (2006) for an overview of popular options. Common to all stationary covariance functions is, however, that they decrease monotonically with increasing input separation s, reflecting the physically consistent decrease in covariability between measurements with increasing temporal separation.

To account for imperfect, noisy measurements as in (4), it is customary to add a noise term to the covariance function. Assuming independent, Gaussian measurement noise, the GP prior covariance matrix can be written as (Rasmussen and Williams 2006)

$$\mathbf{cov}(y) = \mathbf{K} + \sigma_y^2 \mathbf{I}, \tag{6}$$

where $\mathbf{K} = k(t_i, t_j)$ is the prior covariance function matrix (5) evaluated at all possible combinations of training inputs in $t = \{t_1, \ldots, t_n\}$; σ_y^2 is the assumed measurement noise variance and $\mathbf{I}$ is the identity matrix. The diagonal entries of $\mathbf{cov}(y)$ are given by $\sigma_f^2 + \sigma_y^2$, while the off-diagonals are given by (5). The parameters σ_f^2, l, and σ_y^2 are known as *hyperparameters*, and can be varied to best suit the purpose of the GP regression.

We apply GP regression to predict the posterior probability of the model function $f_* = f(t_*)$ at prediction times $t_* = \{t_{*,1}, \ldots, t_{*,n_*}\}$, from the marginal likelihood of the measurements $p[y(t)] \sim \mathcal{N}\left(0, \mathbf{K} + \sigma_y^2 \mathbf{I}\right)$ and a zero-mean Gaussian prior assumption on $f(t)$. In practice, most observational data can be made to fit the zero-mean assumption by normalization. The predictive equations for $\mu(f_*)$ and $\mathrm{cov}(f_*)$, the posterior mean and covariance at the prediction times t_*, are given by, e.g., Rasmussen and Williams (2006) as

$$\mu(f_*) = \mathbf{K}_*^{\mathrm{T}} \left[\mathbf{K} + \sigma_y^2 \mathbf{I}\right]^{-1} \mathbf{y}, \tag{7}$$

$$\mathrm{cov}(f_*) = \mathbf{K}_{**} - \mathbf{K}_*^{\mathrm{T}} \left[\mathbf{K} + \sigma_y^2 \mathbf{I}\right]^{-1} \mathbf{K}_* . \tag{8}$$

In (7) and (8), the $n_* \times n$ matrix $\mathbf{K}_* = \mathbf{K}(t_{*,i}, t_j)$ is the covariance between prediction times t_* and training times t, and $\mathbf{K}_{**} = \mathbf{K}(t_{*,i}, t_{*,j})$, an $n_* \times n_*$ matrix, is the covariance function evaluated for combinations of all n_* prediction times t_*. As (7) reveals, the posterior mean function at any prediction point $t_{*,i}$ is a weighted sum of the observations $\mathbf{y}$, with the weights determined by the parameterization of the covariance function and the measurement noise parameter σ_y. Since the inversion of the $n \times n$ matrix $(\mathbf{K} + \sigma_y \mathbf{I})$ is an $O(n^3)$ operation, it is also apparent that standard GP regression becomes exceedingly computationally expensive as the number of training points X increases. However, the computational complexity is unaffected by the number of prediction points X_*.

The posterior predictive Eqs. (7) and (8) include the hyperparameters l, σ_f, and σ_y from our covariance parameterization (5), and their values are as of yet unknown. To find the GP regression that best models the observations, the hyperparameters are optimized by maximizing the log marginal likelihood of the observations, the form of which is given by, e.g., Rasmussen and Williams (2006) in their Eq. (2.30). In our numerical implementation of GP regression, we use the scikit-learn Python package (Pedregosa et al. 2011), and we perform the optimization with its default limited-memory Broyden–Fletcher–Goldfarb–Shanno (BFGS) gradient descent method (Byrd et al. 1995). The details of our numerical implementation can be seen in the public code that accompanies this paper (see acknowledgments).

Figure 3 demonstrates the application of GP regression on a sample of 100 laser altimeter measurements from the Ekofisk dataset. In Fig. 3a, the 5-Hz range signal z has been

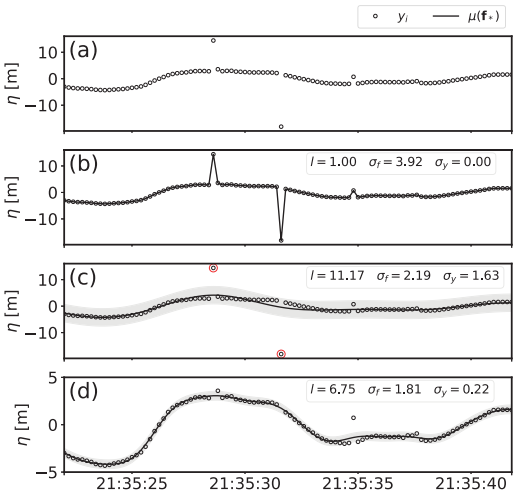

FIG. 3. (a) Sample segment of a raw laser altimeter wave record (laser 4 from 8 Nov 2007). Two large-amplitude spikes are visible just before and after the 2135:30 UTC time stamp, and one potential low-amplitude spike at approximately 2135:35 UTC. (b) The optimized mean prediction of a GP regression $\mu(f_*)$ trained on the raw measurements, where the measurements are assumed to be noise-free (i.e., prior $\sigma_y = 0$). The inset lists the values of the optimized posterior hyperparameters l, σ_f, and σ_y. (c) As in (b), but with prior measurement noise set to $\sigma_y = 1.0$, leading to σ_y being optimized alongside l and σ_f. The shaded contours enclose the 95% confidence interval around the mean function $\mu(f_*)$. (d) The two measurements circled in red that lie outside the 95% confidence interval in (c) have been removed, after which a new GP prediction has been made on the remaining data points.

inverted to a sea surface height signal $\eta = \overline{z} - z$; to be consistent with the notation used for observations above, we refer to the individual η measurements as y_i. In Fig. 3b, we have trained a GP regression on the observations y_i assuming that the observations are noise-free, i.e., $\sigma_y = 0$. In other words, the only free parameters in this case are the length scale parameter l and the signal variance σ_f. Here, and henceforth in this text, we generally use the GP model to give predictions of the mean function and its related uncertainty at the measurement times, i.e., $t = t_*$. More specifically, the prediction time vector $t_* = \{t_{*,1},\ldots,t_{*,n}\}$ is always defined as a set of equidistant measurement times, where the sampling interval $\Delta t_* = 0.2$s in accordance with the 5-Hz sampling rate of the Ekofisk laser altimeters. The sampling interval of the measurements is, however, not always necessarily equidistant due to occasional dropouts caused by instrument malfunction. The initial removal of high-amplitude spikes with a 10MAD(y_i) threshold (see section 2) also occasionally results in individual missing measurement points.

Figure 3b illustrates the effect of neglecting the measurement noise σ_y in the training of the GP model. In this case, the GP model regards the observations as the ground truth, which results in the GP posterior mean function $\mu(f_*)$ following the observations exactly. We also notice that the length scale parameter has been optimized as $l = 1$, meaning that the correlation time scale between the posterior prediction points is equal to the observation sampling interval Δt, resulting in nearly uncorrelated prediction points. This illustrates a phenomenon known as *overfitting*, where the posterior GP model may exhibit a good fit to the training data, but lacks the ability to perform predictions from the posterior. The first point is problematic with respect to our goal of using the GP prediction to differentiate valid measurements from measurement errors (e.g., the two obvious large-amplitude spikes in the example training data in Fig. 3), whereas the latter point is especially problematic if the prediction times are different from the training times (such as when interpolating over long intervals of missing data). Furthermore, setting $\sigma_y = 0$ and $t_* = t$ in (8) gives $\mathrm{cov}(f_*) = 0$, meaning that the GP posterior prediction in Fig. 3b has zero uncertainty.

In the example shown in Fig. 3c, we have performed a second pass through the data by training another GP model on the same training data points, with the difference that the measurement noise parameter σ_y has been optimized alongside l and σ_f. Compared to the previous, noise-free prediction, the noisy prediction has a more smoothly varying mean function $\mu(f_*)$ owing to the longer correlation time scale $l \approx 11\Delta t_*$. The nonzero covariance has here been used to construct a 95% confidence interval around the mean function as 1.96Σ, where

$$\Sigma = \sqrt{\mathrm{diag}[\mathbf{cov}(y)]}. \tag{9}$$

We can see that the two obvious, large-amplitude spikes in the raw measurements fall outside the 95% confidence interval around the mean function. This example illustrates our proposed methodology for spike detection using the GP regression uncertainty estimate Σ; a similar approach was recently taken by Bohlinger et al. (2019) for detecting erroneous wave height measurements derived from satellite altimetry.

Finally, in Fig. 3d the two spikes that were detected in Fig. 3c were removed from the training data, and a new GP regression was trained on the remaining observations. We see that the 95% confidence interval around the new posterior mean function is markedly narrower than in the previous example, leading to at least one new measurement (at 2135:35 UTC) being placed outside the confidence interval. Depending on the purpose of the despiking process, the newly detected spike may be removed and a third pass can be performed with a GP model trained on the further-reduced set of observations, or the measurement may be considered valid and the removed measurements can be interpolated using the posterior mean function in Fig. 3d. While one could argue for the removal of this fairly obvious moderate-amplitude spike, one should also keep in mind that the resulting uncertainty (represented by Σ) of a third consecutive GP regression in this case is likely to narrow down even further. At a certain point, therefore, even very slight deviations from the posterior mean function may end up outside the confidence interval

and become flagged as spikes, potentially leading to an undesired amount of intervention on the raw measurements (e.g., smoothing of the wave profiles). As a potential solution for avoiding this issue, we define a threshold on the coefficient of determination R^2,

$$R^2 = 1 - \frac{\sum_i (y_i - \mu_{*,i})^2}{\sum_i (y_i - \bar{y})^2}, \tag{10}$$

between the observations y_i and the corresponding GP posterior mean function values $\mu_{*,i}$. The maximum value R^2 can attain is 1, which implies a perfect match between the model prediction and the observations. The R^2 scores for the examples presented herein were $R^2 = 0.624$ and $R^2 = 0.990$ for the cases in Figs. 3c and 3d, respectively. Although not shown, a third GP regression with the moderate spike at 2135:35 UTC removed from the training observations returns a posterior mean function that closely follows the remaining, seemingly valid, observations, with $R^2 = 0.999$. For this example wave record, a threshold of $R^2 = 0.990$ would, consequently, end the spike detection iterations at the second GP regression iteration, leaving the moderate-amplitude spike at 2135:35 UTC in the dataset, while a higher threshold would lead at minimum to a third spike detection iteration. Note that in the example described here we have only used the final posterior mean function to interpolate over detected spikes; all other measurements (i.e., those considered valid) have been left intact to minimize unnecessary altering of the original observations. This principle of minimizing the intervention on raw measurements (as advocated by, e.g., Press et al. 1992) is followed throughout this paper.

b. *Optimizing the performance of the GP model on clean wave records*

In this section we seek to optimize the fitting performance while minimizing the computational expense of the GP model by performing regressions on a subset of clean, or spike-free, 20-min wave records from the Ekofisk laser altimeter dataset. The clean records were inspected manually for lack of obvious spikes by visually comparing the four instantaneous laser signals. The clean records were also required to be fully sampled; i.e., no dropouts were allowed within the 20-min records. In addition, only one laser signal was used in the case of two or more records fulfilling these criteria during the same 20-min period. In total, 32 independent records between 1620 UTC 8 November and 1440 UTC 9 November, measured by either laser 1 or laser 2, fulfilled all of the aforementioned criteria and were chosen as clean test records. All computational tests in this section were performed with a standard laptop computer running Ubuntu 18.04.5 LTS (processor: Intel Core i7-8650U CPU, 1.90 GHz × 8; RAM: 31.2 Gb).

We initially focus on the effect of the number of prediction points on GP model performance and computational cost. This effect was investigated by splitting the 6000-sample (20 min sampled at 5 Hz) test records into successively smaller,

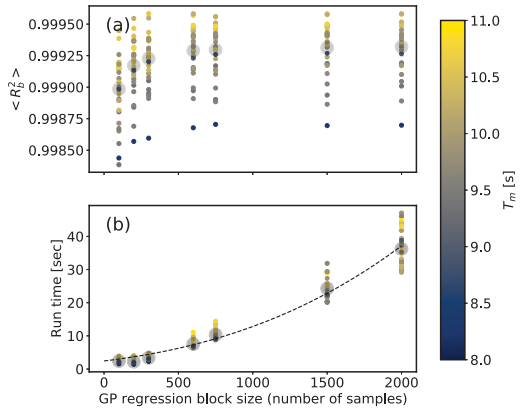

FIG. 4. Performance evaluation of GP regressions performed on the 32 clean 5-Hz laser altimeter test records. (a) Regression score per test record averaged over nonoverlapping blocks ($\langle R_b^2 \rangle$) as a function of block size (number of samples). The small circles represent $\langle R_b^2 \rangle$ for individual test records, and the large circles are ensemble averages for each block size. (b) Total GP regression run time as a function of block size. The small circles represent the run times for each individual GP regression, and the large circles are ensemble averages. The dashed line is a cubic fit to the ensemble average run times. The color scale represents the energy-weighted mean wave period T_m of each test record.

nonoverlapping "blocks" of data, over which regressions were run independently. For this test, the prior hyperparameters (i.e., the first guess) were set to $\sigma_f = 1.0$, $\sigma_y = 1.0$, and $l = 1.0$, and were allowed to be optimized freely in the posterior prediction (i.e., without lower or upper bounds). Since the test records were required to be fully sampled, the prediction inputs $t_* = \{t_{*,1}, ..., t_{*,n_*}\}$ were set equal to the training inputs $t = \{t_1, \ldots, t_n\}$.

To assess the fit of the blockwise GP regressions to the noise-free sample records, we use the block-average coefficient of determination $\langle R_b^2 \rangle$, following the definition in Eq. (10). A perfect match between model and observations gives $\langle R_b^2 \rangle = 1$, and due to the noise-free training datasets and high sampling rate relative to the characteristic motion of the wave field, our test regressions on the noise-free sample records predictably return high values of $\langle R_b^2 \rangle$ ranging between approximately 0.9980 and 0.9999, as shown in Fig. 4a. While the ensemble mean $\langle R_b^2 \rangle$ values are relatively insensitive to regression block size, the scatter in $\langle R_b^2 \rangle$ between the test records appears to be at least in part explained by the mean period of the wave field T_m, with longer-period wave fields scoring high and shorter-period wave fields generally scoring somewhat lower. While a modest improvement in $\langle R_b^2 \rangle$ is achieved by using a GP regression block size of 600 samples or higher, Fig. 4b shows that this comes at a cost of rapidly decreasing time efficiency owing to the $O(n^3)$ computational complexity of the matrix inversions performed during GP model training and optimization.

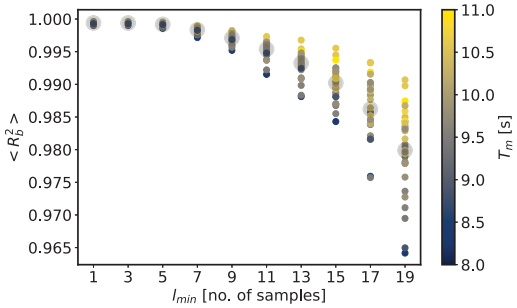

FIG. 5. Block-average regression score $\langle R_b^2 \rangle$ as a function of minimum length scale $l_{\min}$ of GP regressions performed on the clean test records. The small circles represent each test record, and the large circles are ensemble averages. The GP regression block size has been held constant at 200 samples, i.e., 40 s, and the color scaling represents the mean period T_m.

c. *Avoiding overfitting to noise-corrupted measurements*

Unsurprisingly, the test regressions performed on the clean wave records in the previous section produced very close model fits even with extremely short correlation length scales l. However, as shown earlier in Fig. 3b, when the measurements are corrupted by noise (e.g., spikes), a posterior length scale that is approximately equal to the time scale of the noise can lead to overfitting issues, where the posterior mean function cannot distinguish between valid and corrupted measurements. To avoid overfitting, it is therefore advisable to prevent the length scale from being optimized too low (i.e., close to the time scale of the noise). We do this by setting a lower bound $l_{\min}$ on the posterior length scale. Based on the noise characteristics of the Ekofisk laser altimeter signals, we find that $l_{\min} = 5\Delta t_*$ is long enough to generally avoid overfitting to spikes of lengths between Δt and $3\Delta t$. However, because setting $l_{\min}$ too high may also negatively impact the model fit to valid measurements, Fig. 5 shows the block-averaged coefficient of determination $\langle R_b^2 \rangle$ as a function of $l_{\min}$ based on GP regressions on the same subset of clean wave records used in Fig. 4. We see that $\langle R_b^2 \rangle$ is more or less insensitive to the choice of minimum length scale up to $l_{\min} = 5$, after which the model fit begins to deteriorate, with accelerated deterioration in sea states with lower mean period T_m. This further supports our choice of using $l_{\min} = 5$ to avoid overfitting to noise while simultaneously obtaining a good model fit to apparently valid training data points.

Figure 3 exposes another concern related to the overfitting issue, namely, the fact that the uncertainty estimate of the GP regression, Σ, may become excessively low if the training data are very smooth. This typically happens when training the GP model on comparatively noise-free data, and if Σ is used to construct a confidence interval for detecting invalid measurements, the low uncertainty can lead to valid data being erroneously flagged as invalid. Based on our experience with the Ekofisk laser altimeter dataset, such *false positive* spike detection is especially likely to occur in segments of steep gradients in the sea surface displacement time series, such as the front faces of steep, nonlinear waves. A possible solution for avoiding this undesired effect would be to inflate the posterior covariance in the regions of steep gradients. In fact, McHutchon and Rasmussen (2011) address this issue by assuming that noise is present in the input locations t in addition to the common assumption that the measurements $y(t)$ are corrupted by noise (represented by σ_y). McHutchon and Rasmussen (2011) parameterize the input noise σ_t by scaling the posterior covariance with the square of the slope of an initial, standard GP posterior mean function trained on the observations. A second, noisy-input GP (NIGP) regression is then performed with the altered covariance, and the log marginal likelihood is maximized by optimizing the four hyperparameters l, σ_f, σ_y, and σ_t. We applied the input-noise parameterization of McHutchon and Rasmussen (2011) on the laser altimeter dataset, and found that we were indeed able to avoid certain false positive detections by using the inflated covariance to determine the confidence interval around the posterior mean function. However, we also found that the increased model complexity resulting from optimizing four instead of three hyperparameters resulted in an increased tendency for overfitting to the noise. The NIGP approach was hence not pursued further. Instead, we use the approach described in section 3a, where a threshold on the blockwise model fit score R_b^2 is used to determine whether to use the blockwise GP posterior uncertainty $\mathbf{\Sigma}_b$ to flag outliers or, if R_b^2 exceeds the threshold, to assume that the block is composed of valid measurements, and spike detection is unnecessary and likely to lead to false positives. In other words, we use R_b^2 as a proxy for the *signal-to-noise ratio* of the raw measurements.

d. *Signal reconstruction*

In this section we demonstrate how GP regression can be used to replace (i.e., interpolate over) missing values in the wave record, whether they are dropouts due to instrument failure or spikes removed after being flagged by the despiking process. In Fig. 6, we compare the errors generated by replacing missing values with the GP posterior mean function against two standard techniques, linear and cubic spline interpolation, as well as a recent method developed by Støle-Hentschel et al. (2021) based on the convolution theorem. This novel method is included here because of its previously demonstrated potential for improved accuracy in signal reconstruction over traditional interpolation methods for large gap sizes. The deconvolution method for signal reconstruction is based on the observation that the operation of masking a wave signal due to, e.g., the removal of spikes or other faulty measurements is equivalent to a convolution in spectral space. Supposing that the underlying wave signal is sufficiently narrow banded, Støle-Hentschel et al. (2021) showed that the full signal can be reliably reconstructed by deconvolving a reduced system that covers a limited range of frequencies $[f_1, f_2]$ containing the majority of the energy of the underlying wave signal. Støle-Hentschel et al. (2021) showed that, for the optimal choice of frequency range, their method was able to

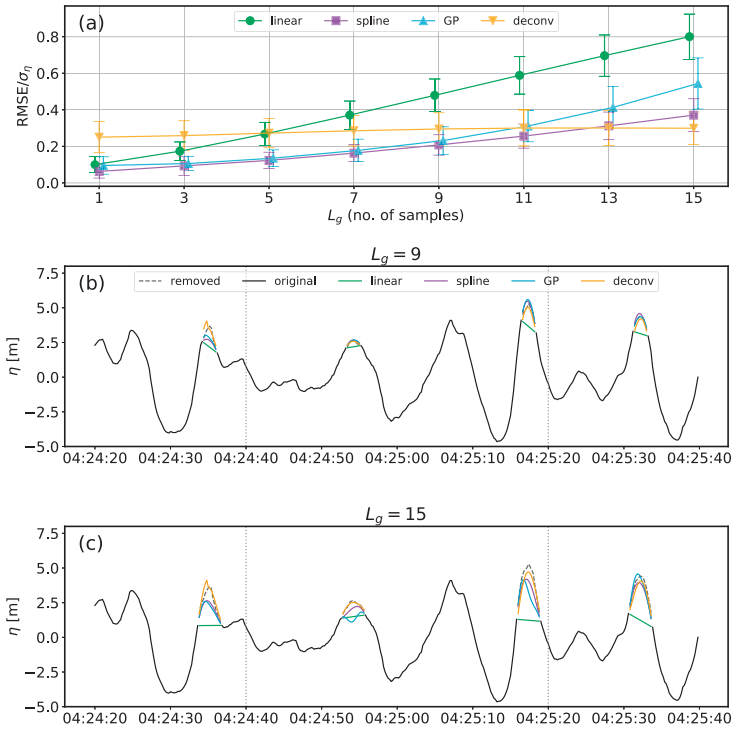

FIG. 6. Interpolation tests performed on the test dataset of 32 clean 20-min wave records used in Figs. 4 and 5. The interpolation methods included are linear interpolation ("linear"), cubic spline interpolation ("spline"), GP regression ("GP"), and deconvolution ("deconv"). (a) The root-mean-square error (RMSE) of the interpolated measurements vs the raw QC.0-level observations normalized by the observation standard deviation σ_η as a function of artificially inserted holes of varying size L_g. The artificial holes have been centered at wave crests (i.e., local maxima in η) separated temporally by a minimum of one peak wave period T_p. Note that only the interpolated gap regions of the wave records were included in the RMSE calculations. (b),(c) Example segments of test records in which crests have been replaced with holes of 9-sample and 15-sample lengths, respectively. The dashed curves show the original measurements, and the colored curves show the interpolation results by the four tested methods. The 200-sample blocks of the GP interpolations are represented by the vertical dotted lines in (b) and (c).

reproduce both real and synthetic sea surface displacement records corrupted with artificial gaps up to one-half peak wave periods in length with exceptionally high accuracy. For our test data, we have applied a frequency range constrained by $f_1 = 0.05$ Hz and $f_2 = 0.3$ Hz, which we expect to capture the majority of the energy within the wave field in the sea states encountered on 8–9 November 2007. For more details on the method and the optimal choice of frequency range, the reader is advised to refer to the original study by Støle-Hentschel et al. (2021).

The interpolation tests here have been performed on the sample dataset of 32 clean wave records used in Figs. 4 and 5 by introducing successively longer gaps L_g centered on the crests of the wave signals η, and comparing the root-mean-square errors (RMSE) normalized by the full-signal standard deviations σ_η resulting from interpolating over the gaps with the different methods. We have chosen to focus the interpolation tests on the wave crest regions because of the negative impact that the accidental removal and improper replacement of high crests may have on, e.g., high-order statistical moments derived from the wave signals. It has also been shown that interpolation over wave crests produces the largest differences in performance between interpolation methods (e.g., Støle-Hentschel et al. 2021).

For the interpolation with GP regression, we employ the approach described in section 3b, where the full 6000-sample test records are split into 200-sample blocks for more efficient computing. The gaps are then interpolated with corresponding values of the posterior mean functions of the GP fits to the test records with the crests removed. The linear and cubic

spline interpolations were performed on the full 20-min signals, while the deconvolution tests were performed with blocks of 500-sample length for computational efficiency.

Figure 6a indicates that cubic spline interpolation performs comparably to interpolation with the GP posterior mean function until the gaps reach a length of more than 9 consecutive data points, while both the GP and spline methods consistently outperform linear interpolation which, by definition, simply cuts down the wave crests, as shown in Figs. 6b and 6c. For gaps shorter than $3\Delta t$ in length, the deconvolution method leads to the highest average errors of the methods included in the comparison; however, the mean error magnitude resulting from the deconvolution interpolation displays very little variation over the range of gap lengths. As the gap lengths exceed $9\Delta t$, or approximately 2 s, the errors induced by interpolation with the GP posterior mean function begin to grow faster than the errors induced by cubic spline interpolation. This is most likely because the GP prediction is optimized with regard to the correlation length scale parameter l which, for the training data used here, generally lies in the range $5\Delta t$–$10\Delta t$. One cannot, therefore, expect the GP posterior to deliver robust replacements for gaps whose length exceeds the optimized correlation scale of the prediction. The cubic spline, on the other hand, produces a smooth interpolation which, for the gap sizes included herein, is well behaved and fairly accurately approximates the removed wave crests. Care should however be taken if gaps grow much longer, as the behavior of the cubic spline interpolator over long sections of missing data may become more erratic (see, e.g., Liu et al. 2014). If extended gaps resulting from, e.g., the removal of multipoint spikes or long periods of missing data are encountered, Fig. 6 suggests that the deconvolution method of Støle-Hentschel et al. (2021) may give improved robustness over the GP-based or the more conventional linear or cubic spline interpolation methods. However, the limited results presented herein are insufficient to justify recommending one specific method for multipoint sea surface reconstruction over another, as this topic is outside of the scope of quality control and demands a dedicated, in-depth study of its own.

e. *Full despiking pipeline*

Here we propose a full stepwise despiking methodology for surface wave time series based on the optimized GP regression settings and parameters determined in the preceding sections. The despiking process involves both spike detection and replacement (i.e., interpolation), and the results of applying the methodology on the Ekofisk laser altimeter test dataset are presented in section 4. To highlight different stages in the despiking methodology, we break up the processing into quality control (QC) steps QC.0–QC.4, in which QC.0 refers to the crudest level of despiking (by a constant global threshold), and QC.4 is the final, highest level of quality control.

- QC.0: To decrease the potential for overfitting in the spike detection stage (QC.1), we remove prominent, unphysical spikes with a global threshold of 10MAD above and below the record median from the raw wave record.
- QC.1: We detect potential remaining spikes that evaded the QC.0-level thresholding by training a GP regression to the QC.0-level record divided into blocks of $n_{*,b} = 200$ training data points. In addition to improving the computational efficiency, the division of the QC.0 records into blocks of $O(100)$ samples in length for despiking also focuses the spike detection and replacement operations on the segments of the records that are most contaminated with intermittent noise. In this way the GP posterior uncertainty is correctly inflated during signal sequences with elevated noise corruption, reducing the probability of overfitting the model to the noise, while noise-free segments can be passed over without intervention. We use the diagonal entries of the GP covariance matrix $\mathbf{\Sigma}_b$ to flag and remove training data points that lie outside a specified confidence interval around the GP posterior mean function $\mu(f_*)$ within each block. We define the confidence interval as $1.96\mathbf{\Sigma}_b$ (i.e., 95%). To determine whether to remove the detected spikes or proceed without intervention, we use a threshold on the blockwise coefficient of determination R_b^2, which acts as a proxy for the signal-to-noise ratio of the GP fit to the training data. This spike detection step for a block is repeated until the R_b^2 threshold is exceeded, or until a specified number of spike detection iterations has been performed (to speed up the processing and avoid underfitting). In our implementation of the method, we choose to use a signal-to-noise threshold of $R_b^2 = 0.995$ and a cap of three consecutive spike detection iterations per block of training data. The maximum limit on iterations per block is set both for reasons of computational efficiency as well as to avoid issues related to underfitting. The latter issue may arise if sufficiently many measurements within a block are flagged as spikes and subsequently removed, leaving an insufficient number of measurements to perform a robust interpolation over the resulting gaps.
- QC.2: We replace initial missing measurements (dropouts) and detected spikes in the QC.1-level product by fitting a final GP regression to the QC.1-level record (with both dropouts and spikes removed), and replace them using the values of the posterior mean function. Alternatively, e.g., if computational efficiency is required, the missing and removed measurements can be interpolated with another method of choice. Based on Fig. 6, the cubic spline method is both efficient and reliable for short to moderate gap sizes (0.2–3 s), whereas the recent deconvolution-based method of Støle-Hentschel et al. (2021) may be used for increased robustness for gaps longer than approximately 3 s. Regardless of the interpolation method of choice, we advocate (in accordance with, e.g., Press et al. 1992) only replacing the missing and removed data points in order to minimize intervention on the raw measurements.
- QC.3: This quality control stage applies only if the signal reconstruction in stage 2 was performed using a GP model. To gauge the quality of the despiked and interpolated QC.2 product, the block-averaged model fit score $\langle R_b^2 \rangle$ of the final, replacement-step posterior mean function can be used to evaluate the quality of the despiked signal. This is

especially advisable if, as in most field measurement datasets, only one measurement record is available such that the despiked signal cannot be compared with one or more collocated signals, as in the Ekofisk laser altimeter test dataset. For example, a threshold can be defined on $\langle R_b^2 \rangle$, over which the signal-to-noise ratio of the QC.2-level record is assumed to be sufficiently low, and the record passes the automated quality control. This may be beneficial, because setting a limit on the number of spike-detection iterations (in the QC.2 step) means that highly noise-corrupted signal blocks may end up with an R_b^2 score significantly below the blockwise R_b^2 threshold.

- QC.4: To validate the results of the automated despiking described in the previous steps, a final manual quality control is recommended for QC.2- or QC.3-level records that contain anomalous measurements. This final quality check may be implemented by following standard guidelines, as described in, e.g., IOOS (2019).

f. The phase space despiking method

Here we give a brief summary of the recent phase space–based despiking method of Voermans et al. (2021), as we will apply it in section 4 in order to evaluate the performance of our proposed GP-based despiking methodology. Following Voermans et al. (2021), we define the phase space in terms of the normalized QC.0-level raw measurements y_i/σ_{y_i} and their standardized acceleration (i.e., the second derivative) $a_i/\sigma_a = y_i''/\sigma_a$, where σ_{y_i} and σ_a are the standard deviations of y_i and a_i, respectively. We compute the sea surface acceleration a_i using a nine-point central difference scheme on the QC.0-level sea surface displacement measurements, following the recommendation of Voermans et al. (2021) for 5-Hz laser altimeter data. The radius of the semimajor axis x_1 of the normalized phase space ellipse is defined, following Voermans et al. (2021), as

$$x_1 = \sqrt{2}p, \tag{11}$$

where p is a multiple that defines the expected fraction of measurements that would fall inside the normalized ellipse if the measurements were drawn from a normal distribution. In line with Voermans et al. (2021), we choose $p = 6$ for our despiking purposes, corresponding to a Gaussian confidence interval of 6σ. The radius of the semiminor axis was defined by Voermans et al. (2021) as

$$x_2 = C\sqrt{\frac{\nu\sigma_a}{\sigma_{y_i}}}T_{m02}, \tag{12}$$

where $C = 0.2$ is an empirical constant, and the spectral parameters $\nu = \left(m_0 m_2/m_1^2 - 1\right)^{1/2}$—the spectral bandwidth of Longuet-Higgins (1975)—and the mean wave period $T_{m02} = (m_0/m_2)^{1/2}$ are computed from the truncated spectral moments

$$m_n = \int_{f_1}^{f_2} f^n E(f)\, df\,. \tag{13}$$

Voermans et al. (2021) compute the wave energy spectrum for (13) from a subset of raw displacement measurements from which individual measurements whose magnitude exceeds $4\sigma_{y_i}$ from the mean have been iteratively removed until no measurements exceed the threshold. This iterative filtering procedure is performed in order to obtain representative estimates of ν and T_{m02}, which, due to their dependence on spectral moments up to second order, are sensitive to the potential presence of high-frequency spikes. While such a low threshold is bound to also remove legitimate wave crests, this is deemed acceptable due to the comparatively minor impact this has on the higher-order spectral moments. Instead of following the iterative filtering process of Voermans et al. (2021), we apply a more robust 4MAD threshold only once to remove high-amplitude measurements for the spectral estimation. We then estimate the spectra for (12) after the removed measurements (and potential initial dropouts) have been interpolated over with a cubic spline function. To account for the effects of this crude filtering process on both the low- and high-frequency range of the spectra, we truncate the spectra at a lower bound of $f_1 = 0.05$ and a maximum frequency $f_2 = 1.0$.

In our implementation of the phase space despiking method, we perform the replacement of flagged spikes and dropouts with cubic spline interpolation. In the original description of the method, Voermans et al. (2021) do not address the issue of spike replacement. Prior studies on phase space methods applied on ADV data, including Goring and Nikora (2002) and Jesson et al. (2013), recommend cubic polynomial interpolation for replacing moderate-length spikes. Our Fig. 6 indicates that the cubic spline interpolation method is able to reasonably reconstruct wave crests cut by artificial holes up to approximately 1–2 s (or 5–10Δt) in length. For this range of gap lengths, the cubic spline also performs very similarly to the GP mean function–based interpolation. We therefore argue that using a cubic spline to replace spikes detected with the phase space method of Voermans et al. (2021) provides a fair comparison to the interpolation with the GP posterior mean function employed in our GP-based despiking methodology. For gaps exceeding 3 s the deconvolution method of Støle-Hentschel et al. (2021) may provide added robustness, as suggested by section 3d; however, in our test dataset we very rarely encounter gaps of such extent due to the high-frequency nature of the spikes in the laser altimeter data (see section 4). For the sake of simplicity, we therefore only perform interpolation with the cubic spline method when despiking with the phase space method.

4. Results

In Figs. 7 and 8, we apply the despiking pipeline outlined in section 3, and summarized in Table 1, on representative segments from the 8–9 November 2007 Ekofisk laser altimeter test dataset. Two separate 20-min segments were selected, for which each of the four laser altimeter wave records were despiked independently. The first sample segment, 1500–1520 UTC 8 November, was characterized by high noise levels, apparent especially in the time series of lasers 3 and 4, as shown in Fig. 7a and as implied by the relatively low QC.

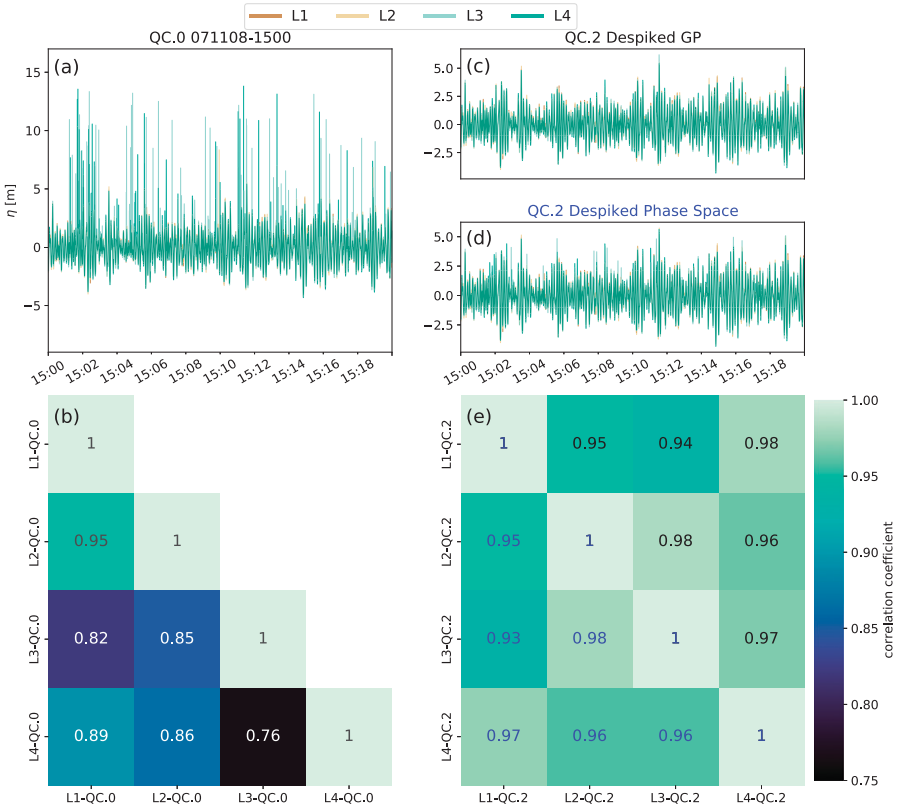

FIG. 7. (a) Simultaneous, spike-contaminated 20-min QC.0-level raw wave records measured by the four nearly collocated laser altimeters during 1500–1520 UTC 8 Nov 2007. (b) The correlation matrix of the QC.0 wave time series in (a). (c) The wave records from (a) despiked with the GP regression–based despiking method outlined in section 3. (d) As in (c), but despiked following the Voermans et al. (2021) phase space despiking method. (e) Correlation coefficients between the despiked wave records; the correlations between the GP despiked records are displayed above the diagonal in black font, while the phase space despiked correlations are displayed beneath the diagonal and colored blue.

0-level signal correlations displayed in Fig. 7b. Conversely, the second sample segment, 0040–0100 UTC 9 November, had highly correlated time series from all four lasers, suggesting low initial noise levels (Figs. 8a,b). It should be noted, however, that a perfect correlation between any two of the four laser signals is extremely unlikely due to both the finite spatial distance between the laser altimeters (array side length of 2.6 m) and their staggered sampling sequences (45-ms time staggering). Regardless, the four despiked wave records in Fig. 7c and the corresponding signal correlations (above the diagonal) in Fig. 7d show that significant improvements in signal correlations were achieved after despiking the noise-contaminated laser signals with the GP-based method. For instance, the signal correlation between lasers 3 and 4 increased from 0.76 to 0.97 before versus after despiking with the GP method. The GP method also performed favorably on the comparatively clean test signals, as shown in Figs. 8c and 8d, with the signal correlations remaining effectively unaltered.

The phase space despiking algorithm of Voermans et al. (2021) was included in the tests shown in Figs. 7 and 8 to allow for comparison against our proposed GP-based despiking algorithm. Because the empirical constant $C = 0.2$ in Eq. (12) was originally determined on the basis of field observations collected in relatively calm sea states ($H_s < 3$ m), Voermans et al. (2021) mention that the functional form of x_2 may have to be changed if their method is to be applied in more energetic situations or to measurements obtained with a different sampling frequency. Furthermore, the value of $C = 0.2$ was originally defined for $p = 2$, which theoretically requires a scaling of x_2 by a factor of 3 if $p = 6$ is chosen, as in our application of the method. We found, however, by despiking the

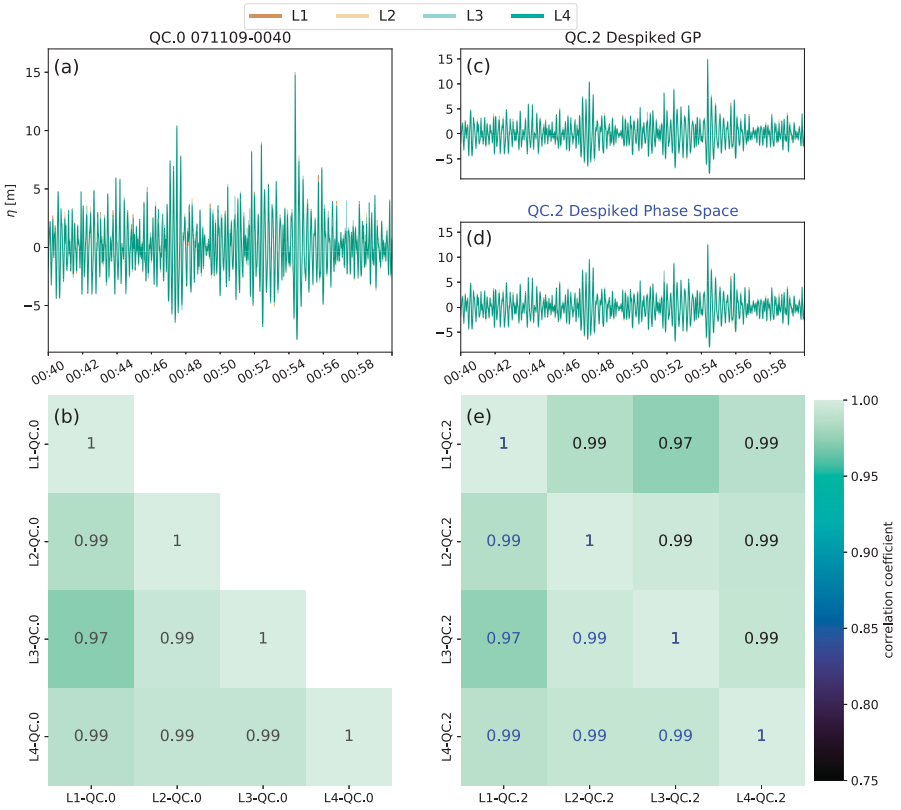

FIG. 8. As in Fig. 7, but for a set of comparatively clean QC.0-level wave records from 0040 to 0100 UTC 9 Nov 2007.

test case shown in Fig. 7d with a range of values of the constant C (other variables unchanged), that for this case, in which $H_s \approx 5.5$ m, using the default value of $C = 0.2$ in (12) resulted in the highest correlations between the despiked wave records. We therefore applied (12) exactly as defined by Voermans et al. (2021) in our implementation of their method.

While the signal correlations resulting from applying the phase space despiking method on the noisy test records (see the blue-colored correlation matrix entries in Fig. 7e) largely increase to similar levels as with the GP method, a close inspection of the phase space despiked time series (Fig. 7d) reveals that several moderate-amplitude spikes pass the control undetected, especially for lasers 3 and 4. Therefore, despite producing comparable improvements in signal correlations, as shown in Fig. 7c the GP-based despiking method appears to more consistently recover the wave signal from behind the noise than the phase space method. In the comparatively clean test case of Fig. 8, neither the GP nor phase space method results in appreciable changes in signal correlation. It is, however, worth noting that the extreme wave recorded just after 0054 UTC (i.e., the Andrea wave), whose maximum crest registered at 14.97, 14.89, 14.92, and 14.73 m above the record mean levels in the QC.0-level raw records of the four lasers, passed through the GP despiking process unaltered, while the phase space method combined with cubic spline interpolation flagged and cut the crest heights down to 11.85, 12.42, 11.73, and 12.27 m, respectively.

A complementary presentation of the results in Figs. 7 and 8 is shown in Fig. 9, where we compare the scalar wave energy spectra $E(f)$ of the two test cases before and after despiking with the GP and phase space methods. The impact of the

TABLE 1. Summary of the GP regression parameters used in the despiking of the North Sea laser altimeter test dataset.

Parameter description	Fixed value(s)
GP regression block size $n_{*,b}$	200
R_b^2 threshold	0.995
Max number of GP iterations	3
Prior l, σ_f, σ_y	5.0, 1.0, 1.0
Posterior l bounds ($l_{\min}$, $l_{\max}$)	(5.0, 30.0)
Spike detection confidence interval	$1.96\boldsymbol{\Sigma}_b$

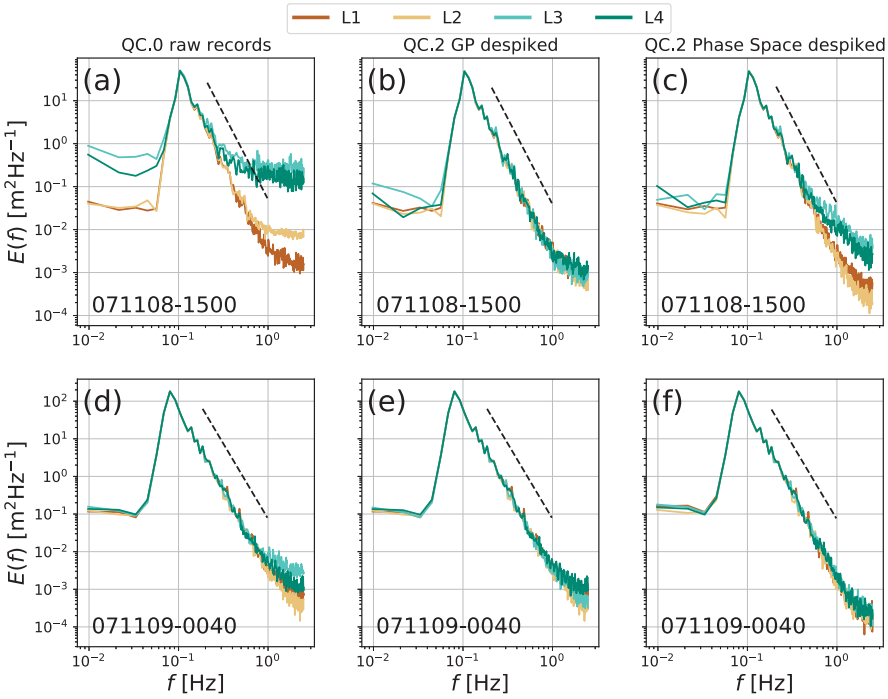

FIG. 9. Comparisons of wave spectra estimated from the sample wave records in Figs. 7 and 8. (a)–(c) Spectra of the raw QC.0 and despiked QC.2-level records from 1500 to 1520 UTC 8 Nov 2007, and (d)–(f) corresponding spectra for the records from 0040 to 0100 UTC 9 Nov 2007. The dashed lines illustrate the theoretical f^{-4} slope of the spectral tail.

presence of spikes on the high-frequency tails of the spectra is evident in the QC.0-level raw records from 1500 to 1520 UTC 8 November (Fig. 9a), especially for lasers 3 and 4, in the deviations of the spectral tails from the theoretical f^{-4} slope of the spectral equilibrium range (e.g., Kitaigorodskii 1983; Phillips 1985). As Fig. 9b shows, the GP-based despiking method proposed herein leads to highly coherent spectra from all four lasers up to approximately 1 Hz. The phase space method, shown in Fig. 9c, also improves on the spectral tail convergence, although the spectra of lasers 3 and 4 begin diverging from the f^{-4} slope at a somewhat lower frequency of approximately 0.5 Hz. This lower divergence frequency is most likely due to the moderate-amplitude spikes that evaded the spike detection, as seen in Fig. 7d. For the comparatively clean test case from 0040 to 0100 UTC 9 November, the QC.0 spectra (Fig. 9d) display strong coherence up to nearly 1 Hz. In this case the GP-based despiking method removes one moderate-amplitude spike from the laser 3 time series (Fig. 8c), improving the overlap slightly in the 1-Hz range, as shown in Fig. 9e. The phase space method, on the other hand, appears to improve the spectral coherence even marginally beyond 1 Hz (Fig. 9f). The smoothing of the highest wave crest induced by the phase space method has, however, little noticeable effect on the spectral estimates.

To verify that the GP method performs consistently also on a larger dataset than the test cases assessed above, we have processed all QC.0-level wave records from the 8–9 November storm dataset using the GP regression parameters summarized in Table 1. Figure 10 shows a clear improvement in the agreement between the QC.2-level significant wave height estimates between the four lasers compared to the QC.0-level estimates presented in Fig. 1. Here we have estimated the significant wave height according to Eq. (1), i.e., in terms of σ_{y_i}, in order to be able to directly compare the QC.0 and QC.2 estimates. H_s can also be estimated from the zeroth-order spectral moment m_0, which for normally distributed surface displacements $\eta(t)$ can be shown (see, e.g., Holthuijsen 2010) to relate to σ_{y_i} by

$$H_s = 4\sigma_{y_i} \approx 4\sqrt{m_0}. \tag{14}$$

Due to its sole dependence on m_0, the significant wave height is therefore comparatively insensitive to the high-frequency effects of typical spikes in the laser altimeter measurements. However, Fig. 11 shows that the higher-order moments (up to m_4) of the QC.2-level despiked wave records also remain well constrained throughout the entire 36-h dataset. The only exception occurs in the 1000–1020 UTC record on 9 November, during which a high-amplitude spike in the laser 3 signal has

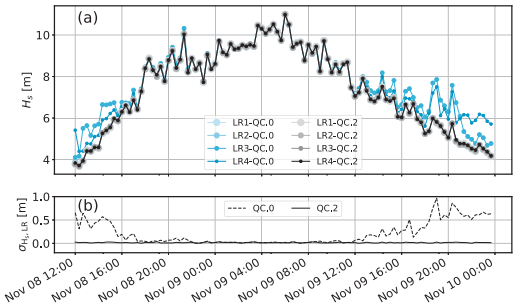

FIG. 10. (a) Time series of significant wave height H_s over the duration of the 8–9 Nov 2007 storm at the Ekofisk field, estimated from both the QC.0-level raw records (blue circles; the same as in Fig. 1c) and the QC.2-level despiked wave records (gray/black circles). (b) The standard deviation of concurrent H_s estimates from the QC.2-level laser altimeter records (solid line). The dashed line shows the initial spread of the concurrent QC.0-level H_s estimates from Fig. 1d.

escaped detection, leading to prominent spikes in the corresponding m_3 and m_4 time series (see also Fig. 12f). This example demonstrates that a close examination of the high-order spectral moments can be used as an additional quality check of despiked wave records.

For extreme value statistical analysis, a more thorough quality control of the despiked wave records involves a visual examination of the highest wave crests in the QC.2-level wave signals. Figure 12 shows close-ups of all QC.2-level despiked wave crests η_c in the Ekofisk laser altimeter test dataset whose

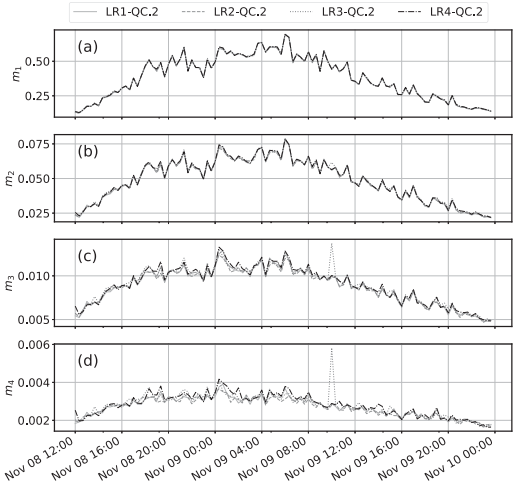

FIG. 11. (a)–(d) Time series of the high-order spectral moments m_1–m_4, respectively, over the duration of the 8–9 Nov 2007 storm at the Ekofisk field, estimated from the QC.2-level despiked wave records.

heights in at least one of the laser signals exceed the commonly used rogue wave threshold of $\eta_c \geq 1.25H_s$ (e.g., Dysthe et al. 2008). It is apparent from Figs. 12f, 12g, and 12i that three moderate to large-amplitude spikes have passed through the despiking stage undetected. While the spikes in the 1000–1020 and 1900–1920 UTC records (Figs. 12f,g) are obvious enough to be detectable visually even if only one wave signal were available, the validity of the QC.2 wave crest of laser 4 in the 2040–2100 UTC record (Fig. 12i) may be more difficult to ascertain from one signal only. Furthermore, Fig. 12b includes a potential case of a false positive spike detection, where the highest crest of the laser 4 signal may have been erroneously cut off.

In Fig. 13 we plot the crest height exceedance probabilities from the three distinct stages of the Andrea storm test dataset. Based on the various H_s estimates shown in Fig. 1, we can identify a buildup stage with rapid wave growth lasting from the start of the test dataset until approximately 1800 UTC 8 November. After this, there is a peak stage of comparatively stable, high seas lasting until approximately 0800 UTC 9 November, followed by a decay stage during which the waves gradually decrease in height. Two standard theoretical exceedance probability distributions are included in Fig. 13 for reference, namely, the Rayleigh distribution of linear, narrowband wave crests, and the second-order, narrowband Tayfun (1980) distribution. As expected, the theoretical distributions underestimate the probability of encountering high wave crests during all stages of the storm, most markedly during the peak stage. However, the relatively small number of wave crests included—approximately 3100, 5200, and 6900 in the buildup, peak, and decay stages, respectively—may lead to somewhat overestimated exceedance probabilities for the highest wave crests (e.g., Støle-Hentschel et al. 2018). Notably, at least one of the four laser altimeters recorded two arguably valid rogue wave crests in both the buildup and peak stages of the storm. During the decay stage, however, three out of the four possible rogue waves turned out to be attributable to undetected spikes, and the remaining extreme crest only exceeds the rogue wave threshold in one of the wave signals.

5. Discussion

The results presented in Figs. 7–13 indicate that our proposed despiking method based on GP regression is able to both reliably filter out most spikes and leave seemingly valid measurements unaltered. In terms of improving wave signal correlations and spectral tail consistency, our method outperforms another state-of-the-art despiking method, the wave physics–based phase space method of Voermans et al. (2021). However, it should be noted that the sea states included in our test dataset are significantly more energetic than those which were used by Voermans et al. (2021) to validate the phase space method, and the phase space coefficients applied herein may require further adjustment for optimal performance. By using the coefficient of determination of the final GP fit to the despiked measurements as a proxy for the signal-to-noise ratio, our methodology was also able to pass the exceptionally high Andrea wave unaltered through the spike

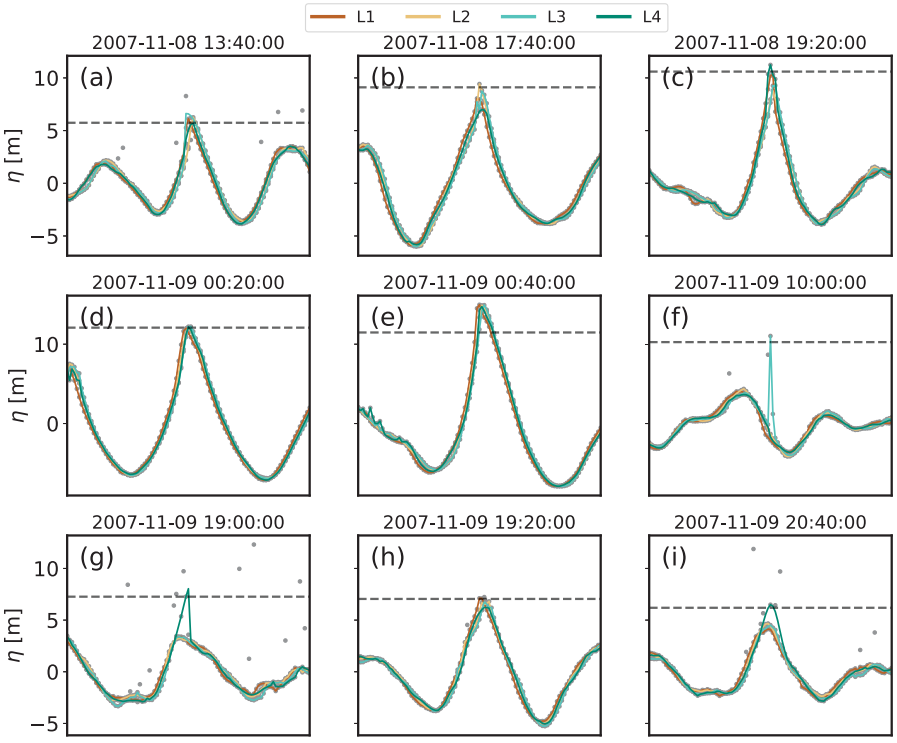

FIG. 12. Close-ups of all QC.2-level despiked waves in the 8–9 Nov 2007 Andrea storm dataset whose crest heights η_c in at least one of the four laser altimeter signals exceed the rogue wave threshold of $\eta_c \geq 1.25H_s$, the level of which is marked in each subplot with a dashed horizontal line. The QC.2 wave signals are color coded, while the raw QC.0-level measurements are plotted with gray dots. The subplot titles indicate the start times of the 20-min wave records during which the waves occurred.

detection stage, while the phase space method erroneously removed the top 2–3 m of the wave from each of the four separate laser signals. However, these improvements come at the expense of significantly increased computational cost compared to the phase space method.

Arguably the most significant limitation of using GP regression for despiking purposes is its high computational complexity. For example, to sequentially perform one GP regression on one 20-min, 5-Hz laser altimeter record split up into 200-sample blocks, the GP method requires roughly 50 times more wall time than the phase space method of Voermans et al. (2021) (which, additionally, does not require splitting up the signal into blocks). Additionally, our proposed GP-despiking pipeline involves potentially rerunning GP regressions on individual blocks up to a user-defined number of iterations, further increasing the computational requirements. Finally, we propose using a final GP posterior mean function, trained on observations from which all detected noise has been removed, to fill in the gaps generated by initial dropouts and detected, and subsequently removed, spikes. While improvements in computational efficiency may be achieved by parallelizing the processing of each independent block, the high computational requirements make the GP method (as presented herein) unlikely to be applicable with current technology to, e.g., real-time despiking of wave measurements. However, if the application is less time constrained (e.g., post-processing of wave records for statistical analysis), the convincing improvements in signal correlation and spectral consistency achieved by the GP method (Figs. 7–11) support its utility as a robust quality control tool. Additionally, continued increases in computational power and cost efficiency may make the GP method viable for real-time processing in the near future.

Being a data-driven method instead of a physically motivated framework such as, e.g., the phase space method of Voermans et al. (2021), the GP method proposed herein may also be vulnerable to mistaking more complex measurement errors than spikes as valid wave phenomena. The buoy measurements analyzed by Thomas (2016) and Voermans et al. (2021), for instance, include large-scale anomalous wave features possibly induced by mooring interference or other external influence on the wave buoys. If the time scales of such anomalous events are comparable to the characteristic time

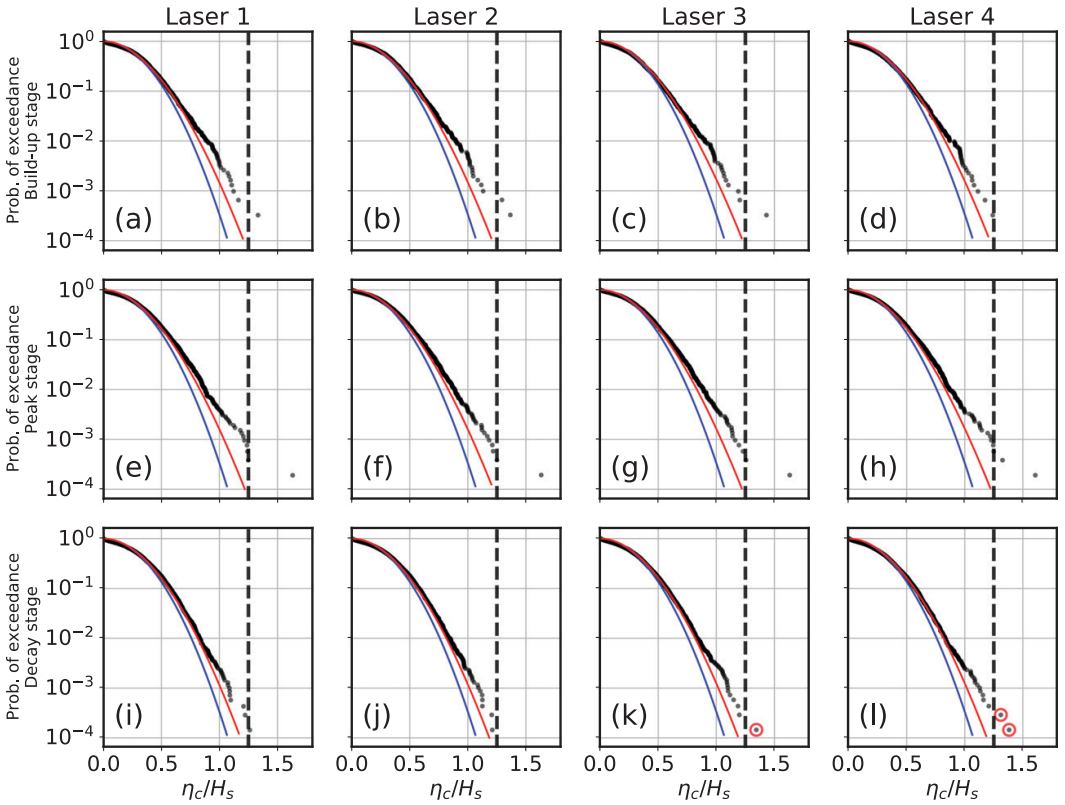

FIG. 13. Exceedance probabilities of QC.2-level crest heights η_c normalized by the 20-min significant wave heights H_s during the (a)–(d) buildup (1200–1800 UTC 8 Nov), (e)–(h) peak (1800 UTC 8 Nov–0800 UTC 9 Nov), and (i)–(l) decay (0800 UTC 9 Nov–0000 UTC 10 Nov) stages of the Andrea storm. The dashed vertical line indicates the rogue wave threshold $\eta_c/H_s \geq 1.25$, and the red circles in (k) and (l) are around the rogue wave crests mark the erroneous crests (i.e., undetected spikes) identified in Figs. 12f, 12g, and 12i. The blue curve is the theoretical Rayleigh distribution for linear crest heights, and the red curve is the second-order Tayfun (1980) distribution.

scales of the wave field (and within the bounds set on the GP correlation length scale hyperparameter l), the standard GP method described herein may lack information on which to reject the events as erroneous, whereas a phase space method, for instance, can potentially be used to differentiate between physically realistic and unrealistic sea surface displacements and accelerations from such complex erroneous phenomena. Consequently, given the superior spike-detection performance of the GP method on highly noise-corrupted wave records (see Fig. 9), and the superior computational efficiency of the phase space method, a hybrid method may be contemplated in which GP regression is used for despiking, coupled with anomaly detection with a phase space method. Also, spectral and time-domain quality control criteria (e.g., Tucker 1993; Thomson and Emery 2014; IOOS 2019) should always be employed to manually verify anomalous measurements, especially if the wave records are to be used for extreme value statistical analysis where undetected measurement errors may bias the high-order statistical moments of empirical distributions. Future studies may focus on extending the GP methodology presented herein with more physically motivated premises. Following the phase space philosophy, a potential extension may for example involve applying GP regression on time series of the raw signal accelerations.

6. Summary

Wave height measurements recorded by an array of four vertically oriented laser altimeter rangefinders during a storm in the North Sea have been used to demonstrate and evaluate a despiking methodology based on Gaussian process (GP) regression. The probabilistic and nonparametric nature of GP regression allows for flexible spike detection performance by using the intrinsic uncertainty of the GP regression, and the method is also suited for replacing flagged or missing measurements. The performance of the method was validated by despiking the four nearly collocated and simultaneously sampled wave records independently of one another. We showed

that the method significantly improved the signal correlation and spectral shape consistency of noise-corrupted wave records, while clean raw wave records that lacked obvious measurement errors were passed through the processing unaltered. An extensive, 36-h dataset covering the entire North Sea storm event was later used to convincingly demonstrate the consistency of the method in despiking laser altimeter records in a wide range of sea states and various levels of noise corruption. The GP-based despiking method was also compared against a state-of-the art phase space method (Voermans et al. 2021). While the GP method performed favorably in comparison to the phase space method in improving the spectral consistency of a noise-corrupted test dataset, the GP method also comes at the price of significantly higher computational complexity, reducing its appeal for real-time despiking applications. Furthermore, it is uncertain whether the phase space parameters applied herein, based on validations performed with limited field data by Voermans et al. (2021), are optimal for the energetic sea states encountered in our North Sea test dataset. The interpolation capability of GP regression was shown to be comparable to standard cubic spline interpolation for short to moderate data gaps up to approximately 2 s in length, and our results also support the applicability of a recent interpolation method based on deconvolution (Støle-Hentschel et al. 2021) for cases in which the data gaps exceed 3 s. However, the topic of multipoint spike replacement is outside of the main scope of the current study and warrants further dedicated investigation. The results presented herein suggest that the GP-based despiking methodology is most suited to offline postprocessing of surface wave records. Last, although our proposed methodology was shown to lead to significant improvements in terms of spectral coherence and signal correlation, a visual examination of the highest wave crests in the despiked wave records revealed that manual quality control procedures remain essential for studies concerned with extreme wave and crest height statistics.

Acknowledgments. The authors are thankful for the support from ConocoPhillips and Equinor through the StereoWave joint industry project. The code, including test data sets, for our implementation of the despiking methodology described in this article is publicly available at https://github.com/mikapm/np-despike.

APPENDIX

Stepwise Example GP Despiking Algorithm

Algorithm 1 is a step-by-step example of our spike detection algorithm based on GP regression. Since our implementation is based on the scikit-learn Python package, the syntax in algorithm 1 mimics the actual Python syntax. GP regression packages with similar syntax can at the time of writing also be found for most other popular data analysis languages, such as MATLAB or R. We recommend using preexisting packages for performing the GP regression because of their optimal computational performance; however, a stepwise sample GP algorithm is also provided in, e.g., Rasmussen and Williams (2006, their algorithm 2.1).

The function outlined in algorithm 1 takes as input 1D arrays with the raw data y and the corresponding inputs array x. It is assumed that missing data points, including large-amplitude spikes detected, e.g., with a MAD threshold, have been assigned a recognizable value (e.g., NaN in Python or MATLAB). Algorithm 1 returns a Boolean mask which indicates the indices of detected spikes in the input raw data array y. While the algorithm does not show the spike replacement step, it can readily be modified to do so by adding a line of code that replaces the detected spikes in y with corresponding values of the posterior mean function μ. The coefficient of determination R^2, which we use to determine whether or not to replace detected spikes, is commonly available as an optional output from the GP regression packages; if not, it can be computed as in Eq. (10).

Algorithm 1 GP-based spike detection algorithm

1: **procedure** DetectSpikesGP (x, y) ▷ Input: x(inputs), y(raw data) ▷ Output: mask (spike indices)

Initialize training data y_t and corresponding training inputs x_t.

2: y_t:= mean(y) − y ▷ Zero-mean training data y_t

3: x_t:= x(isnan(y)) ▷ Valid training inputs x_t

Construct covariance kernel by combining a squared exponential function [Eq. (5)] with length scale bounded from below by $l_{\min}$ with Gaussian (white) noise with initial noise level $\sigma_y = 1$, and use the kernel to initialize the GP regression (GPR).

4: kernel:= SquaredExponential(l_min = $l_{\min}$) + WhiteNoise(σ_y = 1)

5: gp:= GPR(kernel)

Fit a GP model to the training inputs x_t and training data y_t by optimizing the hyperparameters by maximizing the log-marginal likelihood.

6: gp.fit(x_t, y_t)

Predict the posterior mean function μ and standard deviation Σ (the square root of the diagonals of the covariance matrix) for the prediction inputs x based on the optimized GP fit to the training data.

7: μ, **cov** = gp.predict(x)

8: $\Sigma = \sqrt{\text{diag}(\textbf{cov})}$

Flag raw data points that fall outside the 95% confidence interval around the posterior mean.

9: mask:= ($y < \mu - 1.96\Sigma$) & ($y > \mu + 1.96\Sigma$)

10: **return** mask

REFERENCES

Bohlinger, P., Ø. Breivik, T. Economou, and M. Müller, 2019: A novel approach to computing super observations for probabilistic wave model validation. *Ocean Modell.*, **139**, 101404, https://doi.org/10.1016/j.ocemod.2019.101404.

Byrd, R. H., P. Lu, J. Nocedal, and C. Zhu, 1995: A limited memory algorithm for bound constrained optimization. *SIAM J. Sci. Comput.*, **16**, 1190–1208, https://doi.org/10.1137/0916069.

Cattrell, A., M. Srokosz, B. Moat, and R. Marsh, 2018: Can rogue waves be predicted using characteristic wave parameters? *J.*

Geophys. Res. Oceans, **123**, 5624–5636, https://doi.org/10.1029/2018JC013958.

Chawla, A., D. M. Spindler, and H. L. Tolman, 2013: Validation of a thirty year wave hindcast using the Climate Forecast System Reanalysis winds. *Ocean Modell.*, **70**, 189–206, https://doi.org/10.1016/j.ocemod.2012.07.005.

Christou, M., and K. Ewans, 2014: Field measurements of rogue water waves. *J. Phys. Oceanogr.*, **44**, 2317–2335, https://doi.org/10.1175/JPO-D-13-0199.1.

Cox, A. T., and V. R. Swail, 2001: A global wave hindcast over the period 1958–1997: Validation and climate assessment. *J. Geophys. Res.*, **106**, 2313–2329, https://doi.org/10.1029/2001JC000301.

Donelan, M. A., and A. K. Magnusson, 2017: The making of the Andrea wave and other rogues. *Sci. Rep.*, **7**, 44124, https://doi.org/10.1038/srep44124.

——, W. M. Drennan, and A. K. Magnusson, 1996: Nonstationary analysis of the directional properties of propagating waves. *J. Phys. Oceanogr.*, **26**, 1901–1914, https://doi.org/10.1175/1520-0485(1996)026<1901:NAOTDP>2.0.CO;2.

Donoho, D. L., and P. J. Huber, 1983: The notion of breakdown point. *A festschrift for Erich L. Lehmann*, Wadsworth, 157–184.

Dysthe, K., H. E. Krogstad, and P. Müller, 2008: Oceanic rogue waves. *Annu. Rev. Fluid Mech.*, **40**, 287–310, https://doi.org/10.1146/annurev.fluid.40.111406.102203.

Goring, D. G., and V. I. Nikora, 2002: Despiking acoustic Doppler velocimeter data. *J. Hydraul. Eng.*, **128**, 117–126, https://doi.org/10.1061/(ASCE)0733-9429(2002)128:1(117).

Haakenstad, H., Ø. Breivik, M. Reistad, and O. J. Aarnes, 2020: NORA10EI: A revised regional atmosphere-wave hindcast for the North Sea, the Norwegian Sea and the Barents Sea. *Int. J. Climatol.*, **40**, 4347–4373, https://doi.org/10.1002/joc.6458.

Häfner, D., J. Gemmrich, and M. Jochum, 2021: FOWD: A Free Ocean Wave Dataset for data mining and machine learning. *J. Atmos. Oceanic Technol.*, **38**, 1305–1322, https://doi.org/10.1175/JTECH-D-20-0185.1.

Holthuijsen, L. H., 2010: *Waves in Oceanic and Coastal Waters.* Cambridge University Press, 404 pp.

Huber, P. J., 1981: *Robust Statistics.* Probability and Mathematical Statistics Series, Wiley, 308 pp.

IOOS, 2019: Manual for real-time quality control of in-situ surface wave data: A guide to quality control and quality assurance of in-situ surface wave observations version 2.1. IOOS Tech. Rep., 69 pp.

Jesson, M., M. Sterling, and J. Bridgeman, 2013: Despiking velocity time-series—Optimisation through the combination of spike detection and replacement methods. *Flow Meas. Instrum.*, **30**, 45–51, https://doi.org/10.1016/j.flowmeasinst.2013.01.007.

Kitaigorodskii, S. A., 1983: On the theory of the equilibrium range in the spectrum of wind-generated gravity waves. *J. Phys. Oceanogr.*, **13**, 816–827, https://doi.org/10.1175/1520-0485(1983)013<0816:OTTOTE>2.0.CO;2.

Krogstad, H. E., 2006: The Ekofisk laser array: Analysis and data intercomparisons. NTNU Tech. Rep., 47 pp.

——, A. K. Magnusson, and M. A. Donelan, 2006: Wavelet and local directional analysis of ocean waves. *16th Int. Offshore and Polar Engineering Conf.*, San Francisco, CA, International Society of Offshore and Polar Engineers, ISOPE-I-06-204, https://onepetro.org/ISOPEIOPEC/proceedings-abstract/ISOPE06/All-ISOPE06/ISOPE-I-06-204/9962.

——, S. F. Barstow, L. P. Mathiesen, L. Lønseth, A. K. Magnusson, and M. A. Donelan, 2008: Extreme waves in the long-term wave measurements at Ekofisk. *Proc. Rogue Waves 2008 Workshop*, Brest, France, Ifremer, 13–15.

Liu, X., J. C. Xia, J. Gunson, G. Wright, and L. Arnold, 2014: Comparison of wave height interpolation with wavelet refined cubic spline and fractal methods. *Ocean Eng.*, **87**, 136–150, https://doi.org/10.1016/j.oceaneng.2014.05.013.

Longuet-Higgins, M. S., 1975: On the joint distribution of the periods and amplitudes of sea waves. *J. Geophys. Res.*, **80**, 2688–2694, https://doi.org/10.1029/JC080i018p02688.

Magnusson, A. K., and M. A. Donelan, 2013: The Andrea wave characteristics of a measured North Sea rogue wave. *J. Offshore Mech. Arct. Eng.*, **135**, 031108, https://doi.org/10.1115/1.4023800.

——, R. Jensen, and V. Swail, 2021: Spectral shapes and parameters from three different wave sensors. *Ocean Dyn.*, **71**, 893–909, https://doi.org/10.1007/s10236-021-01468-7.

Makri, I. M., S. M. Rose, M. Christou, R. Gibson, and G. Feld, 2016: Examining field measurements of deep-water crest statistics. *ASME 2016 35th Int. Conf. on Ocean, Offshore and Arctic Engineering*, New York, NY, American Society of Mechanical Engineers, OMAE2016-54363, https://doi.org/10.1115/OMAE2016-54363.

McHutchon, A., and C. E. Rasmussen, 2011: Gaussian process training with input noise. *Advances in Neural Information Processing Systems*, MIT Press, 1341–1349.

Pedregosa, F., and Coauthors, 2011: Scikit-learn: Machine learning in Python. *J. Mach. Learn. Res.*, **12**, 2825–2830, https://www.jmlr.org/papers/v12/pedregosa11a.html.

Phillips, O., 1985: Spectral and statistical properties of the equilibrium range in wind-generated gravity waves. *J. Fluid Mech.*, **156**, 505–531, https://doi.org/10.1017/S0022112085002221.

Press, W. H., S. A. Teukolsky, W. T. Vetterling, B. P. Flannery, and M. Metcalf, 1992: *Numerical Recipes in Fortran 90: The Art of Scientific Computing*. Cambridge University Press, 963 pp.

Rasmussen, C. E., and C. K. I. Williams, 2006: *Gaussian Processes for Machine Learning.* Adaptive Computation and Machine Learning, MIT Press, 248 pp.

Smith, M., S. Reece, S. Roberts, I. Psorakis, and I. Rezek, 2014: Maritime abnormality detection using Gaussian processes. *Knowl. Inf. Syst.*, **38**, 717–741, https://doi.org/10.1007/s10115-013-0685-z.

Starkenburg, D., S. Metzger, G. J. Fochesatto, J. G. Alfieri, R. Gens, A. Prakash, and J. Cristóbal, 2016: Assessment of despiking methods for turbulence data in micrometeorology. *J. Atmos. Oceanic Technol.*, **33**, 2001–2013, https://doi.org/10.1175/JTECH-D-15-0154.1.

Støle-Hentschel, S., K. Trulsen, L. B. Rye, and A. Raustøl, 2018: Extreme wave statistics of counter-propagating, irregular, long-crested sea states. *Phys. Fluids*, **30**, 067102, https://doi.org/10.1063/1.5034212.

——, J. C. N. Borge, and K. Trulsen, 2021: The deconvolution as a method to deal with gaps in ocean wave measurements. *Ocean Eng.*, **219**, 108373, https://doi.org/10.1016/j.oceaneng.2020.108373.

Tayfun, M. A., 1980: Narrow-band nonlinear sea waves. *J. Geophys. Res.*, **85**, 1548–1552, https://doi.org/10.1029/JC085iC03p01548.

Thomas, J., 2016: Wave data analysis and quality control challenges. *OCEANS 2016 MTS/IEEE Monterey*, Monterey, CA, Institute of Electrical and Electronics Engineers, https://doi.org/10.1109/OCEANS.2016.7761054.

Thomson, J., L. Hošeková, M. H. Meylan, A. L. Kohout, and N. Kumar, 2021: Spurious rollover of wave attenuation rates in sea ice caused by noise in field measurements. *J. Geophys. Res. Oceans*, **126**, e2020JC016606, https://doi.org/10.1029/2020JC016606.

Thomson, R. E., and W. J. Emery, 2014: *Data Analysis Methods in Physical Oceanography*. Newnes, 728 pp.

Toffoli, A., A. Babanin, M. Onorato, and T. Waseda, 2010: Maximum steepness of oceanic waves: Field and laboratory experiments. *Geophys. Res. Lett.*, **37**, L05603, https://doi.org/10.1029/2009GL041771.

——, ——, M. A. Donelan, B. K. Haus, and D. Jeong, 2011: Estimating sea spray volume with a laser altimeter. *J. Atmos. Oceanic Technol.*, **28**, 1177–1183, https://doi.org/10.1175/2011JTECHO827.1.

Tucker, M., 1993: Recommended standard for wave data sampling and near-real-time processing. *Ocean Eng.*, **20**, 459–474, https://doi.org/10.1016/0029-8018(93)90015-A.

Voermans, J. J., A. V. Babanin, C. Kirezci, J. T. Carvalho, M. F. Santini, B. F. Pavani, and L. P. Pezzi, 2021: Wave anomaly detection in wave measurements. *J. Atmos. Oceanic Technol.*, **38**, 525–536, https://doi.org/10.1175/JTECH-D-20-0090.1.

Wahl, T. L., 2003: Discussion of "Despiking acoustic Doppler velocimeter data" by Derek G. Goring and Vladimir I. Nikora. *J. Hydraul. Eng.*, **129**, 484–487, https://doi.org/10.1061/(ASCE)0733-9429(2003)129:6(484).

Article II

6.2 On the groupiness and intermittency of oceanic whitecaps

Mika P. Malila, Jim Thomson, Øyvind Breivik, Alvise Benetazzo, Brian Scanlon and Brian Ward.

Journal of Geophysical Research: Oceans, **127**(1), e2021JC017938, doi:10.1029/2021JC017938 (2022)

JGR Oceans

RESEARCH ARTICLE
10.1029/2021JC017938

On the Groupiness and Intermittency of Oceanic Whitecaps

M. P. Malila[1,2,3], J. Thomson[3,4], Ø. Breivik[1,2], A. Benetazzo[5], B. Scanlon[6], and B. Ward[6]

[1]Norwegian Meteorological Institute, Bergen, Norway, [2]Geophysical Institute, University of Bergen, Bergen, Norway, [3]Department of Civil and Environmental Engineering, University of Washington, Seattle, WA, USA, [4]Applied Physics Laboratory, University of Washington, Seattle, WA, USA, [5]Institute of Marine Sciences (ISMAR), National Research Council (CNR), Venice, Italy, [6]AirSea Laboratory, Centre for Ocean Research and Exploration, Ryan Institute, National University of Ireland, Galway, Ireland

Abstract The enhancement of wave breaking activity during wave group passage is investigated using coherent field observations of the instantaneous sea surface elevation and whitecap coverage from platform-based stereo video measurements in the central North Sea. Passing wave groups are shown to be associated with a two to threefold enhancement in the probability distribution of total whitecap coverage W whereas the enhancement of active whitecap coverage W_A is approximately fivefold. Breaking time scales and intermittency characteristics are also investigated with the inclusion of a secondary data set of W and W_A observations collected during a research cruise in the North Pacific. The time scale analysis suggests a universal periodicity in wave breaking activity within a representative sea-surface area encompassing approximately one dominant wave crest. The breaking periodicity is shown to be closely linked to the peak period of the dominant wave components, suggesting that long-wave modulation of wave breaking is a predominant mechanism controlling the intermittency of wave breaking across scales.

Plain Language Summary In the open ocean, wind waves of similar wavelength, period and direction combine to form wave groups, also known as sets to surfers and other beachgoers. In deep water, the individual waves in groups travel twice as fast as the groups themselves, and momentarily grow in height and steepness in the wave group center, making them theoretically more likely to break. We show, using field observations of wave breaking taken with digital video cameras, that waves in deep water are up to five times more likely to break in large wave groups than during lulls in the wave field. We also show that the large, dominant wave groups regularly initiate wave breaking at a wide range of scales. Our findings can be used to produce more accurate predictions of when individual waves will break, an active and relatively poorly understood area of current wave research.

Key Points:

- Wave breaking activity and extent is significantly enhanced in wave groups
- The periodicity of the oceanic whitecap coverage is closely linked to the periodicity of dominant wave components
- The intermittency characteristics of whitecap coverage approximately follow similarity scaling laws of other general stochastic processes

Correspondence to:
M. P. Malila,
mikapm@met.no

Citation:
Malila, M. P., Thomson, J., Breivik, Ø., Benetazzo, A., Scanlon, B., & Ward, B. (2022). On the groupiness and intermittency of oceanic whitecaps. *Journal of Geophysical Research: Oceans*, *127*, e2021JC017938. https://doi.org/10.1029/2021JC017938

Received 25 AUG 2021
Accepted 6 JAN 2022

The copyright line for this article was changed on 24 FEB 2022 after original online publication.

Author Contributions:
Conceptualization: M. P. Malila, J. Thomson, Ø. Breivik
Data curation: M. P. Malila
Formal analysis: M. P. Malila
Funding acquisition: Ø. Breivik, B. Ward
Investigation: M. P. Malila
Methodology: M. P. Malila, A. Benetazzo, B. Scanlon
Resources: J. Thomson, B. Scanlon, B. Ward
Software: M. P. Malila, A. Benetazzo
Supervision: J. Thomson, Ø. Breivik
Validation: M. P. Malila
Visualization: M. P. Malila
Writing – original draft: M. P. Malila
Writing – review & editing: J. Thomson, Ø. Breivik, A. Benetazzo, B. Scanlon, B. Ward

1. Introduction

The breaking in deep water of wind-generated ocean surface waves is an intermittent process, scattered unevenly in space and time and occurring over a variety of scales. Breaking waves dissipate wave energy as turbulence and entrain air in bubbles just below the surface (Thorpe, 1982). Turbulent dissipation rates immediately beneath breaking waves are orders of magnitude above values encountered in non-breaking regions (Agrawal et al., 1992; Derakhti, Thomson, & Kirby, 2020; Gemmrich & Farmer, 1999; Sutherland & Melville, 2015; Terray et al., 1996; Thomson et al., 2016). The bubbles generated during wave breaking are a dominant mechanism driving air-sea gas exchange (Melville, 1996; Zappa et al., 2007). In engineering applications, large-scale breaking can cause critical loading on offshore structures (Chella et al., 2012). The energy dissipation due to wave breaking limits wave growth, and balances the energy input by wind and wave-wave energy transfer in the spectral equilibrium range (Komen et al., 1994; Phillips, 1985). The steep forward faces of breaking waves also induce airflow separation, which may significantly enhance the local momentum transfer between air and sea (Banner & Melville, 1976; Buckley & Veron, 2016; Reul et al., 2008). Wave breaking also affects the roughness and emissivity of the sea surface, and is therefore important to account for in remote sensing applications (Anguelova & Webster, 2006; Monahan & O'Muircheartaigh, 1986; Salisbury et al., 2013).

Considerable effort has been directed in recent decades into formulating a framework that successfully describes and predicts the evolution of wave crests toward the onset of breaking (Babanin et al., 2007; Banner et al., 2000; Banner & Peirson, 2007; Barthelemy et al., 2018; Derakhti & Kirby, 2016; Derakhti, Kirby, et al., 2020; Saket et al., 2017; Song & Banner, 2002). The onset is closely linked to wave geometry, which for simple plane waves

is described by the wave steepness H/λ, where H is the wave height and λ is the wavelength. The classical Stokes irrotational water wave profile (Stokes, 1880) can be shown to be unable to maintain its shape, leading to an uncontrolled collapse of the surface, when $H/\lambda > 1/7$, or equivalently, $ak > 0.443$, where $a = H/2$ is the wave amplitude and $k = 2\pi/\lambda$ is the wavenumber (Michell, 1893). Kinematically, the collapse of the wave profile during breaking is due to the particle velocity at the wave crest exceeding the phase speed c of the wave, whereas in a dynamic sense breaking occurs when the downward acceleration of the water surface on the forward face of a wave surpasses a limiting threshold (Babanin, 2011; Perlin et al., 2013). Recently, Barthelemy et al. (2018) introduced a novel dynamic breaking threshold formalism based on the flux convergence of mechanical wave group energy focused on the crest region of the highest wave of a group.

The focusing of wave components, whether as a result of linear superposition or nonlinear interactions, related to the group structure of directional wave fields has long been thought to influence the onset of wave breaking in deep water. Early observations by Donelan et al. (1972) and Holthuijsen and Herbers (1986) reported recurring breaking patterns at periods linked to the periodicity of the dominant wave field, with breaking apparently occurring preferentially near the central apex of the wave group envelope. Similarly, wave group-related periodic recurrence in wave breaking was found by Smith et al. (1996) in an analysis of "sea spikes" in grazing-angle S-band marine radar records. Terrill and Melville (1997) likewise observed low-frequency modulations in near-surface oceanic sound speed, which they attributed to bubble entrainment due to large-scale breaking occurring at wave-group time scales.

In general, the characteristic steepness of the long, dominant wave components in the open ocean is on the order of $ak_p \approx 0.1$, where k_p is the wavenumber at the peak of the wave spectrum—significantly lower than the critical steepness of $ak \approx 0.443$. Therefore, group focusing mechanisms are quite unlikely to cause their bulk steepness to exceed the critical breaking steepness (Babanin et al., 2011; Holthuijsen & Herbers, 1986; Schwendeman & Thomson, 2017). However, regardless of the underlying focusing mechanism, the group-induced variations in amplitude and steepness experienced by the dominant waves affect the stretching and compression of the shorter, wind-forced wave components in the spectral equilibrium range that ride on the backs of long waves. These modulations affect the breaking probability of the short waves thanks to their higher intrinsic steepness (Guimaraes, 2018). Theoretically, the effect of long wave motions on the short wave steepness can be explained by the straining of the long-wave orbital motions against the excess momentum flux due the short waves, also known as the wave radiation stress (Longuet-Higgins & Stewart, 1960, 1964). Conversely, the long-wave modulations of the breaking characteristics of the short waves have also been shown to impact the growth rate of the long waves due to changes in the form drag over the wave field induced by air flow separation in the breaking regions (Donelan et al., 2010; Kudryavtsev & Chapron, 2016).

Dulov et al. (2002, 2021) investigated the impact of long-wave modulations on the breaking characteristics of short waves using a combination of optical video imagery for breaker detection and an array of wave staffs for measuring the instantaneous sea-surface elevation within the camera footprint. They found strong modulation of the phase and amplitude of the instantaneous *whitecap coverage*, W, by dominant waves, with short-wave breaking most likely to occur at the crests of the long waves. Similarly, Yurovsky et al. (2017) compared the instantaneous W to the instantaneous sea-surface elevation estimated from synchronous K_a-band Doppler radar and optical video recordings, and found that high values of W, indicative of active, large scale wave breaking, coincided with the passage of large wave groups. The group-enhanced breaking was found to be significant in young, growing sea states with marked group structure, while the breaking in old, decaying sea states was generally smaller in scale and more random in character, with a smaller degree of coincidence with the group structure of the wave field. In another recent study, Schwendeman and Thomson (2017) used high-resolution sea surface reconstructions from stereo video measurements coupled with conventional whitecap identification methods to verify the validity of the Stokes limiting wave profile in the crest regions of breaking directional waves.

Inspired by the approaches of Dulov et al. (2002), Yurovsky et al. (2017), and Dulov et al. (2021), the current study investigates the modulation of wave breaking by dominant wave groups in terms of the time variability of the whitecap coverage W. We employ coherent (i.e., simultaneous and co-located) observations of W and the sea surface elevation, acquired with an optical stereo video camera system installed on a platform in the North Sea, to study the coincidence of elevated wave breaking activity and wave group passage. We also analyze the temporal intermittency and clustering tendencies of the whitecap coverage with the *telegraph approximation* (TA), a methodology that isolates the time variability of a time series from its amplitude variations. The TA formalism has

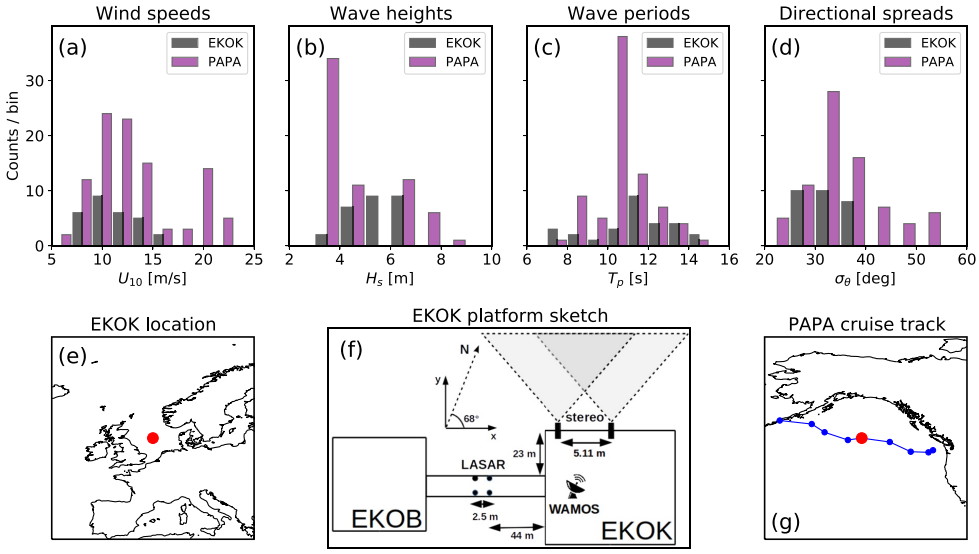

Figure 1. (a)–(d) Histograms summarizing the wind and wave conditions during the acquisition periods of the EKOK and PAPA data sets. The bin heights represent the number of observational records per bin in each data set. (e) The location of the Ekofisk platform (EKOK) at approximately (56.5°N, 003.2°E). (f) Sketch of the Ekofisk K and B platforms, showing the approximate locations of the stereo video cameras, laser altimeter array (LASAR) and WAMOS radar. (g) The cruise track of the December 2019 North Pacific cruise (PAPA) on R/V Sikuliaq. The location of Ocean Station P (50°N, 145°W) is marked with a red dot.

previously been used to uncover similarity structures in other intermittent stochastic processes such as turbulent velocity and temperature fluctuations (Cava et al., 2012; Huang et al., 2021; Sreenivasan & Bershadskii, 2006). However, to our knowledge this is the first application of the TA to the study of the intermittency of wave breaking. For the investigation of the time scales of breaking, we introduce an additional field data set of W measurements collected during a recent cruise in the North Pacific.

The remainder of this text is structured as follows. The field data sets are introduced in Section 2. The data processing methods are described in Section 3 and the analysis methods in Section 4. Our results are presented and discussed in Section 5 and concluding remarks are delivered in Section 6.

2. Data

2.1. North Sea Stereo Video Measurements

A dual camera stereo video system was installed in 2017 on the Ekofisk K platform, located in the central North Sea within the extensive Ekofisk oil and gas field. The stereo video footprint faces open waters toward the northwest (see Figures 1e and 1f), and the closest platforms to the south are ∼2 km away. The stereo video system consists of two PointGrey Blackfly GiGE CCD digital cameras fitted with Edmund Optics 12 mm fixed-focal length lenses. The cameras are separated by a 5.11 m baseline distance, and sit approximately 28 m above mean sea level. The cameras are oriented with parallel lines of sight and oblique viewing angles approximately 70° from nadir. The camera viewing angles were set by aligning the fields of view so that the horizon lies just out of frame above the upper edge of the image frames. This maximizes the sea surface area covered by the stereo images while avoiding potentially abrupt pixel intensity gradients at the horizon line which may negatively interfere with the cameras' automatic exposure adjustment.

The northwest-facing orientation of the stereo video system was chosen to ensure exposure to the longest unobstructed fetch associated with weather systems approaching from the north, as well as to minimize unwanted sun glare in the stereo video images. Minimizing sun glare is important from an image processing perspective, as the stereo reconstruction of the wave field assumes a near-Lambertian sea surface for which the reflecting properties

are independent of viewing angle (Jähne et al., 1994). The stereo video image acquisition is controlled using an Arduino Uno microcontroller, which is programed to synchronize the hardware triggering of the cameras and control the frame rate. All of the stereo video sequences analyzed in this study were obtained at a frame rate of five frames per second (fps) and at a resolution of five megapixels (2,048 × 2,448 pixels).

In this study, the images acquired by the stereo cameras will be used to both reconstruct the sea surface elevation at high temporal and spatial resolution (see Section 3.1) as well as to estimate the fractional whitecap coverage W (see Section 3.2). The Ekofisk stereo video data set (hereafter EKOK) consists of 28 20-min stereo video sequences spread over five separate days during the 2019–2020 winter and spring season. Wind speeds were measured on the Ekofisk L platform 2.3 km south of the stereo camera location with a Vaisala WMT703 sonic anemometer located at 102.3 m height above mean sea level. Due to the high elevation of the wind anemometer, the wind speeds at Ekofisk L were converted to 10-m wind speed assuming neutral atmospheric stratification using the power-law approximation

$$U_{10} = U_z(10/H)^{\alpha}, \tag{1}$$

where U_z is the wind measurement observed at height $H = 102.3$ m, and $\alpha = 0.06$. The wind profile approximation in Equation 1 applied to oil platform-based anemometer data in the North Sea was found to best correspond to measured radiosonde wind profiles by Furevik and Haakenstad (2012), as well as more recently to microwave satellite wind speeds by Manaster et al. (2019). Hereafter, all references to U_{10} implicitly mean the equivalent neutral wind. The environmental conditions encountered during the stereo video acquisition periods are summarized in Figure 1, with significant wave height and peak period, H_s and T_p, estimated from the stereo video wave field reconstructions. Due to the limited field of view of the stereo video footprint, the directional spread σ_θ is estimated from two-dimensional spectra obtained from an X-band marine radar using the wave monitoring system WAMOS (Reichert et al., 1999) situated on the helideck of the EKOK platform (at ∼49 m above mean sea level). See also Section 3.1 for a validation of the stereo video wave spectra against the WAMOS product and a nearby laser altimeter array located on a footbridge connecting the EKOK platform to the nearby B platform (see Figure 1f). Additional details of the degree of groupiness of the wave field (group lengths, spectral bandwidth, and directional spread) encountered in the EKOK data set are presented in Section 5.1.

2.2. North Pacific Cruise Data

We supplement the North Sea stereo video measurements with single-camera whitecap coverage estimates acquired during a research cruise onboard the R/V Sikuliaq in the North Pacific Ocean in December 2019. We hereafter refer to this data set with the abbreviation PAPA, after Ocean Station P ("Papa")—an oceanographic observation site in the mid-North Pacific visited during the cruise. The PAPA cruise was a 2.5-week field experiment dedicated to measuring environmental parameters driving the physics of air-sea interactions such as wave breaking and bubble dynamics.

The digital camera setup on the PAPA experiment was identical to the one described in Schwendeman and Thomson (2015a) and analyzed in Schwendeman and Thomson (2015b), and will therefore only be briefly introduced here. Two Point Grey Flea2 digital camera equipped with 2.8 mm focal-length wide angle lenses were attached to the port and starboard railings on the bridge deck of the ship at approximately 16 m height above the water level. Video recordings at frame rates between 5 and 7.5 fps and 1,288 × 964 pixels resolution were acquired at times when the vessel was held stationary due to other sampling activity such as buoy deployments and recoveries or vertical water profiling casts. Only one of the cameras could be operated at a time, and the choice of which camera to operate was generally motivated by the ship's heading (to minimize sky reflections or direct sunlight) and local wind direction (to avoid droplet accumulation on the recording camera lens in the presence of rain or sea spray). The length of the video recordings varied between approximately 5 and 60 min, but only continuous recordings with a minimum length of 10 min were used here for further analysis. Likewise, continuous records longer than 20 min were split into shorter sequences between 10 and 20 min in length.

Wind speeds were measured underway from a sonic anemometer mounted on the ship's bow mast at ∼16 m height. The 16-m wind speeds were converted to neutrally stratified 10-m estimates using the COARE algorithm, a standard procedure for low-elevation, buoy and ship-based wind speed conversion in the marine atmospheric boundary layer (Fairall et al., 2003). The wave field was continuously observed with freely floating, retrievable

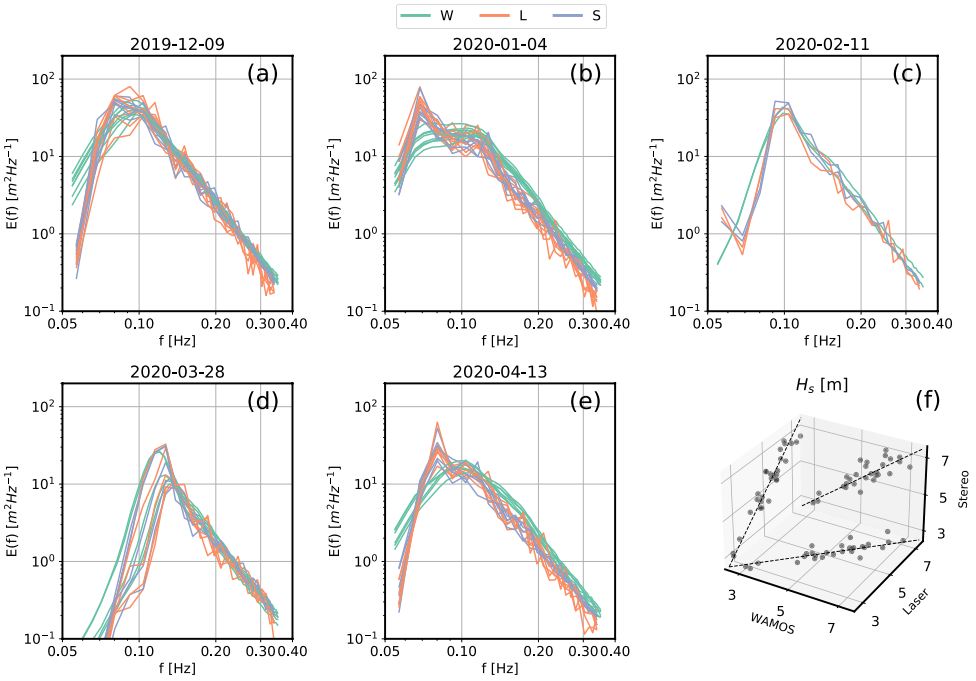

Figure 2. (a)–(e) Comparison of scalar wave spectra from the WAMOS radar (*W*), laser altimeter array (*L*) and stereo video reconstructions (*S*) during the EKOK observational records. (f) Comparison of H_s estimates inferred from the respective spectra.

SWIFT wave buoys (Thomson, 2012), which provided measurements of wave field parameters, such as wave height and period. The buoy locations did not, however, coincide with the footprints covered by the video cameras. See Figure 1 for a synopsis of the sea state conditions encountered during the video acquisitions on the PAPA cruise. Details of the groupiness of the wave field in the PAPA data set are given in Section 5.1.

3. Data Processing Methods

3.1. Stereo Video Reconstruction

The EKOK stereo video image pairs were used to reconstruct the instantaneous sea-surface topography with the open-source stereo wave processing software "Waves Acquisition Stereo System" (WASS), see Benetazzo (2006), Benetazzo et al. (2012), and Bergamasco et al. (2017). WASS automates the processing steps required to perform the extrinsic calibration, feature matching, and triangulation, producing three-dimensional point clouds of the instantaneous sea surface elevation, which we later interpolated onto regular 2-D x, y grids with 50×50 cm^2 grid size. The intrinsic calibration is not automated and was performed manually on the platform on 7 August 2019, prior to the acquisition and processing of the images.

In Figure 2, we compare scalar wave energy frequency spectra $E(f)$ estimated from virtual wave staffs within 20-min sequential stereo video grids against spectra from a nearby 5-Hz laser altimeter array (Magnusson & Donelan, 2013) and the WAMOS radar. All spectra are truncated at a low frequency of 0.05 Hz and a high-frequency cutoff of 0.35 Hz in order to cover the fairly limited frequency range of the WAMOS radar. The spectral shapes from the stereo video and the laser altimeters show good agreement, while the WAMOS spectra—obtained by integrating the frequency-directional spectra over all directions—are generally smoother and display less pronounced peaks, especially in the low-frequency swell range. However, the estimates of the significant

Table 1
Stereo Video and Image Grid Characteristics in the EKOK and PAPA Data Sets

Data set	Grid type	Grid variable	Spatial resolution [m]	Frame rate [fps]	Area [m^2]
EKOK	Stereo video	η [m]	0.5	5	4,020
EKOK	Image	Pixel intensity	0.5	5	4,020
PAPA	Image	Pixel intensity	0.8	5–7.5	6,504 (5,416, 7,964)

Note. The PAPA grid area reported is the median area, and the maximum and minimum areas are in parentheses.

wave height $H_s = 4\sqrt{m_0}$, inferred from the zeroth-order spectral moments m_0 and compared in Figure 2f, are quite consistent across all instruments.

3.2. Whitecap Thresholding

In this section, we describe our process for estimating, via pixel brightness thresholding operations, the fractional whitecap coverage from the optical imagery in EKOK and PAPA field data sets. Hereafter, we will refer to two separate quantities related to the whitecap coverage, namely the total whitecap coverage W, which quantifies the full fractional coverage of whitecap-related foam present on the sea surface at any given time, and the active whitecap coverage W_A, in which only the actively breaking contribution of the whitecap coverage is considered. Moreover, we use the variable names W and W_A to refer to the instantaneous, frame-wise whitecap coverage, whereas $\overline{W}$ and $\overline{W}_A$ refer to time-averaged quantities.

Prior to whitecap thresholding, the digital video frames from the EKOK and PAPA data sets were geo-rectified into earth-referenced projections and gridded onto regular x, y grids using Delaunay triangulation and bi-linear interpolation. Since the EKOK data set includes double frames for each time step while only one frame is required for whitecap thresholding, only frames from the left camera were used. The EKOK frames were geo-rectified using the camera pose estimated by the extrinsic calibration of the stereo video analysis, and interpolated onto grids of the same shape as the sea-surface reconstructions. The ship-based PAPA video frames were stabilized and geo-rectified using the horizon-tracking algorithm of Schwendeman and Thomson (2015a) and interpolated onto grids with 80 cm grid cell side length. Due to the rolling motion of the ship, the PAPA grid sizes display small variations depending on the instantaneous angle of view. In general, the PAPA image grids cover a somewhat larger footprint than the EKOK grids because of the wider angle lenses used. We also performed the analysis presented in this study on reduced (i.e., cropped) grid sizes for the PAPA data set, but found no significant impact on the results, supporting similar findings reported by Schwendeman and Thomson (2015b). Table 1 summarizes the grid characteristics in the two data sets.

3.2.1. Total Whitecap Coverage W

We estimated the fractional whitecap coverage W from the image grids in both data sets following the pixel threshold-based approach of Kleiss and Melville (2011). By examining the shapes of the cumulative pixel intensity histograms of several sequential grayscale image grids, this methodology identifies a pixel intensity value above which the pixels likely represent foam from either actively breaking waves or decaying whitecaps. The thresholding operation results in binary image grids, and the instantaneous value of W is calculated as the fraction of pixels whose value exceeds the threshold within each grid. Due to the potential presence of other bright features in the images apart from whitecap foam, such as sun glints or rain droplets, we performed a manual inspection of the thresholded image grids to verify that the thresholding mainly isolates the foam while largely ignoring other bright features. In some cases in the PAPA image data set (where the camera exposure was controlled manually), we manually varied the pixel threshold to optimally isolate the foam. Image grid sequences with extensive amounts of sky reflections or droplet accumulation on the camera lenses were discarded.

3.2.2. Active Whitecap Coverage W_A

The thresholding approach outlined above produces estimates of the total whitecap coverage W within the camera footprint, including the residual decaying foam of previously broken waves. To estimate the fractional whitecap coverage due to actively breaking waves, W_A, we followed the approach of Schwendeman and Thomson (2015b),

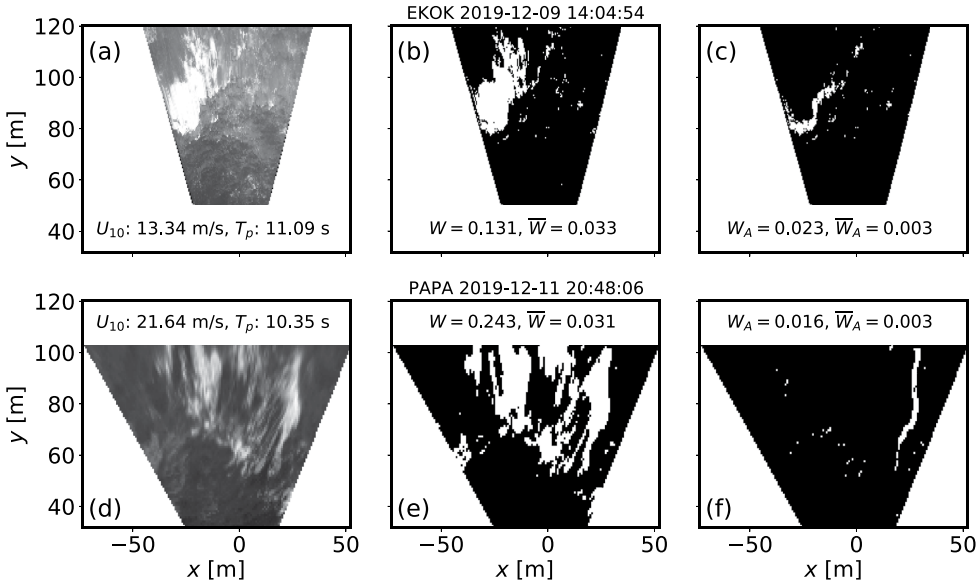

Figure 3. Sample image grid snapshots from the EKOK (upper row) and PAPA (lower row) data sets, displaying the differences between whitecap foam classification for total whitecap coverage W and actively breaking whitecap coverage W_A. Panels (a) and (d) show geo-rectified image grids in which each pixel (i.e., grid cell) can take on integer values between 0 (black) and 255 (white). The prevailing wind speed U_{10} and peak wave period T_p are annotated under/above the original image grids in (a) and (d). Panels (b) and (e) show the resulting binary grids of the thresholding process of Kleiss and Melville (2011) applied on the original image grids, where the pixels representing whitecap-related foam (white pixels with value 1) have been isolated from the background sea surface (black pixels with value 0). Panels (c) and (f) show the estimated actively breaking foam fraction, determined following the approach of Schwendeman and Thomson (2015b). The instantaneous values of W and W_A for each example frame, as well as the respective record-mean values $\overline{W}$ and $\overline{W}_A$, are annotated under/above the respective binary image grids.

in which the binary pixels of a thresholded image grid are assumed to be part of an actively breaking wave crest the first time the pixel values change from 0 to 1 within a short time period. The assumption is that the pixels remain "flipped" until the remnant foam patch has dissipated. In our W_A analysis, we set the time lag for tracking the pixel value changes to 10 s, which in most of our field data corresponds approximately to the period of the dominant waves (see Figure 1c). As the example in Figure 3 shows, this method of W_A classification only isolates the leading crests of breaking waves, potentially leading to lower values of time averaged W_A compared to observations based on different classification criteria, for example, dynamically motivated filtering algorithms (Mironov & Dulov, 2008) or manually selected image features (Scanlon & Ward, 2013). However, the W_A estimates produced by the method of Schwendeman and Thomson (2015b) effectively pinpoint the location and time of breaking initiation, and are therefore well-suited to the purpose of this study, namely the analysis of the group-enhancement of breaking activity (see Section 5.2) and breaking intermittency (see Section 5.3).

4. Analysis Methods

The analysis conducted in this study can be divided into two main parts. First, we investigate the wave group-enhancement of the whitecap coverage from the coherent sea surface height-whitecapping information in the EKOK data set only. The methods for identifying wave groups from the stereo video reconstructions are described in Section 4.1. The second part of the analysis concerns the intermittency and clustering of the whitecap coverage. This part only requires time series of the whitecap coverage, and is therefore performed on both the EKOK and PAPA data sets. The intermittency analysis methodology is described in Section 4.2.

4.1. Wave Group Detection

The tendency of dominant waves to occur in distinct groups of successive high waves is enhanced when the wave energy frequency spectrum $E(f)$ is narrow (Goda, 1970; Longuet-Higgins, 1984). In the canonical JONSWAP parameterization of developing wave spectra (Hasselmann et al., 1973), the peakedness of the wave spectrum is modeled with a peak enhancement factor that has been shown to depend strongly on wave age, with young, growing seas typically exhibiting relatively narrow, peaked spectra that correspond to pronounced wave field groupiness (Donelan et al., 1985). The spectral width is commonly estimated with the bandwidth parameter of Longuet-Higgins (1975),

$$\nu = \sqrt{\frac{m_2 m_0}{m_1^2} - 1}, \tag{2}$$

where m_n is the n-th spectral moment,

$$m_n = \int_0^\infty f^n E(f)\,\mathrm{d}f. \tag{3}$$

However, due to its dependence on the second-order spectral moment m_2, the value of the ν parameter is sensitive to the high-frequency spectral cutoff. For this reason, a more robust bandwidth measure can be composed from the spectral peakedness parameter of Goda (1970),

$$Q_p = \frac{2}{m_0^2}\int_0^\infty f E^2(f)\,\mathrm{d}f. \tag{4}$$

Following Janssen and Bidlot (2009), the spectral bandwidth in the spectral peak region can be estimated with the inverse peakedness parameter Q_p^{-1}.

Due to the dispersive nature of waves in deep water, individual dominant wave components advance through wave groups at the phase speed $c = 2c_g$, where c_g is the group speed of wave energy propagation, undergoing modulations of their amplitude and steepness underway. This type of dispersive wave energy focusing is primarily a *linear* effect caused by additive superpositions of wave components with different wavelengths and frequencies. Linear superposition of wave components may also occur due to the directional focusing of wave trains traveling in crossing directions. Another measure of the spectral width that is of importance to the group structure of the wave field is therefore the directional spread σ_θ of the wave energy distribution. The directional spread can be inferred from the distribution of directional components in the frequency-direction wave spectrum $E(f, \theta)$. However, in practice, the directional spread of measured wave spectra is often calculated from the first two-to-four Fourier coefficients of the directional distribution, since these coefficients are readily estimated from the cross spectra of the horizontal and vertical displacements of for example, drifting wave buoys (Herbers et al., 2012; Kuik et al., 1988).

Under certain conditions, wave groups are also subject to a type of *nonlinear* evolution known as modulational instability, during which the wave spectrum undergoes nonlinear transformations which can lead to pulse-like wave groups with potentially extremely high amplitude and steepness (Benjamin & Feir, 1967). Modulational instability has been shown to produce large-amplitude rogue and breaking waves in laboratory and numerical experiments (Dysthe et al., 2008), but its significance in the real open ocean is a topic of ongoing debate due to the strict assumptions of spectral narrowness in both frequency and directional spread required for the instability to take effect (Adcock et al., 2011; Fedele et al., 2016). Janssen and Bidlot (2009) introduced the parameter

$$R = \frac{\sigma_\theta^2}{2(Q_p^{-1})^2} \tag{5}$$

to quantify the joint contributions of directional spread and frequency bandwidth on the susceptibility of a directional sea state to modulational instability. Within the range $0 < R < 1$, Janssen and Bidlot (2009) considered the wave field to be in a focusing regime in which wave field nonlinearity is enhanced, whereas $R \geq 1$ implies a defocussing regime in which nonlinear interactions are suppressed by directional dispersion.

In this study we define wave groups as periods of elevated wave energy within a wave record. Focusing here solely on the EKOK data set, the wave group structure recovered from the stereo video data is directly compared to the coherent whitecap coverage within the same area of the sea surface. In order to isolate groups formed by the dominant waves, we perform a spatial filtering of the EKOK stereo video sea surface reconstructions by averaging each instantaneous elevation grid over a centralized square area whose side length equals one-eighth of the peak wavelength L_p, estimated with the linear dispersion relation from the peak wave period T_p of the point-wise scalar wave energy spectra of the virtual wave staffs (see Section 2.1). This creates the equivalent of a low-pass filtered sea surface elevation time series $\bar{\eta}(t)$, formally defined as

$$\bar{\eta}(t) = \frac{1}{N_x N_y} \sum_{i=1}^{N_x} \sum_{j=1}^{N_y} \eta_{ij}, \tag{6}$$

where $N_x = N_y$ indicate the number of grid cells to average over in the x and y directions, respectively, and are determined by the peak wavelength L_p. The side length of the averaging area was chosen as $L_p/8$ in order to fit the square within the stereo video footprint also for the longest wave lengths in the EKOK data set. From $\bar{\eta}(t)$, wave groups can be identified with minimal influence of short, riding wave components which may cause unnecessary splitting of the dominant wave groups. An example of a filtered mean sea surface time series is shown in Figure 4a.

4.1.1. The Run Threshold Method

By the simplest definition, a wave group is a train of high dominant waves appearing in a consecutive fashion. In a surface elevation time series, for example, such a wave train would show an uninterrupted sequence of waves higher than some prescribed threshold. Following Kimura (1980), we use a threshold wave height of H_{rms}, the root-mean-square wave height, where individual wave heights are estimated from the 20-min $\bar{\eta}(t)$ records in the EKOK data set using the zero-upcrossing method (Holthuijsen, 2007). Each run of waves exceeding H_{rms} and longer than one peak wave period in duration is defined as a wave group.

4.1.2. The Hilbert Spectrum

Another common approach to detecting wave groups is by examining the instantaneous energy of the wave signal. This can be performed by analyzing the envelope of the wave signal by, for example, the Hilbert transform (Bitner-Gregersen & Gran, 1983), the wavelet transform (Donelan et al., 1996), or convolution-based smoothing techniques (Funke & Mansard, 1980). In this study, we apply the empirical mode decomposition (EMD) based method introduced by Veltcheva and Guedes Soares (2007), in which the instantaneous wave energy IE is estimated from the Hilbert spectrum (defined below) of the mean sea surface elevation time series. Wave groups are defined by the crossings of the IE signal above and below its record-mean level, as in Veltcheva and Guedes Soares (2016). Moreover, as for the H_{rms} threshold method, we require the wave groups identified by the IE threshold to be at least one peak wave period in length.

EMD is a method developed by Huang et al. (1998) for extracting the local frequency content of a broadband, multi-component (and potentially nonlinear and non-stationary) signal. The principle behind EMD analysis consists of decomposing a time series into a finite number of single-component basis functions called intrinsic mode functions (IMF) and a residual trend, the superposition of which reconstructs the original signal. The IMFs are determined via an iterative sifting process in which each IMF by definition is an oscillating signal containing an almost equal number of local extrema and zero-crossings (the respective numbers can differ at most by one), and has a zero mean at all points between the envelopes connecting the local IMF minima and maxima. Defined in this way, each IMF represents one mode of oscillation of the original signal, and the distances between consecutive IMF extrema represent the signal's intrinsic time scales. The residual component typically lacks a full oscillation and thus can be viewed as describing a background trend. In contrast to conventional Fourier decomposition, in which the signal is decomposed into simple trigonometric basis functions, the IMFs can be both amplitude and frequency modulated. As a result, the EMD method is not limited by the strict requirement of signal stationarity that applies to Fourier analysis, and can also be applied successfully to nonlinear signals (Huang et al., 1998).

The EMD method allows us to represent the variation of the wave signal's energy content in both time and frequency. An analytic function $Z_j(t)$ can be estimated for each IMF by

$$Z_j(t) = X_j(t) + iY_j(t), \tag{7}$$

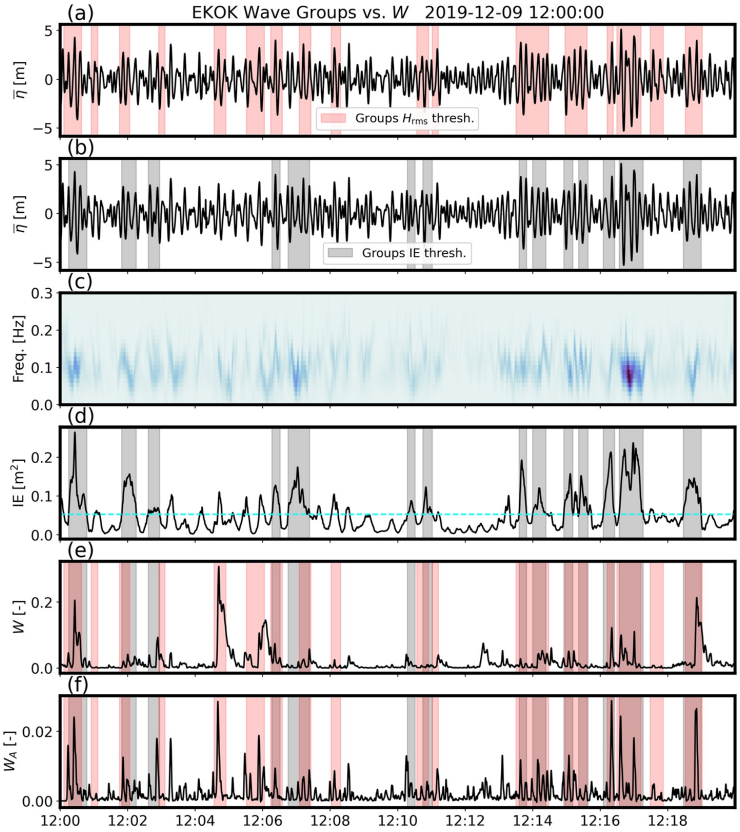

Figure 4. Sample coherent time series from the EKOK data set. (a) and (b) The stereo video spatially averaged sea-surface elevation $\bar{\eta}$. (c) The Hilbert spectrum of $\bar{\eta}$. (d) The instantaneous wave energy IE. (e) The instantaneous total whitecap coverage W. (f) The instantaneous active whitecap coverage W_A. In (a), wave groups defined by the H_{rms} threshold are shaded red, and in (b) wave groups defined by the IE threshold are shaded gray. The record-mean level of IE, that is, the wave group threshold, is marked with a horizontal dashed line in (c). Both the IE and H_{rms} group definitions are plotted in (e) and (f).

where the conjugate pair $X_j(t)$ and $Y_j(t)$ are the j-th IMF and its Hilbert transform, respectively, and i is the imaginary unit. The analytic function (7) can be used to estimate the envelope amplitude and a well-defined instantaneous frequency for each IMF. For the purposes of the current study, the instantaneous amplitude and frequency are used to quantify the group modulation—in both amplitude and frequency—of the wave signals $\bar{\eta}(t)$ in terms of the Hilbert spectrum $\mathcal{H}(f,t)$. The Hilbert spectrum was defined by Huang et al. (1998) as the distribution of the squared amplitude envelopes of all IMFs in both time and frequency. Following Veltcheva and Guedes Soares (2016; their Equation 19), integrating the Hilbert spectrum over all frequencies gives the instantaneous energy IE(t) of the wave signal,

$$\mathrm{IE}(t) = \int_{f_1}^{f_2} \mathcal{H}(f,t)\,\mathrm{d}f. \tag{8}$$

Sample time series of $\mathcal{H}(f,t)$ and the associated instantaneous wave energy IE(t) are shown in Figures 4c and 4d.

Advantages of the Hilbert spectral approach—also known as the Hilbert-Huang Transform (HHT)—over more traditional Fourier and wavelet-based time-frequency energy distributions applied to nonlinear phenomena, such

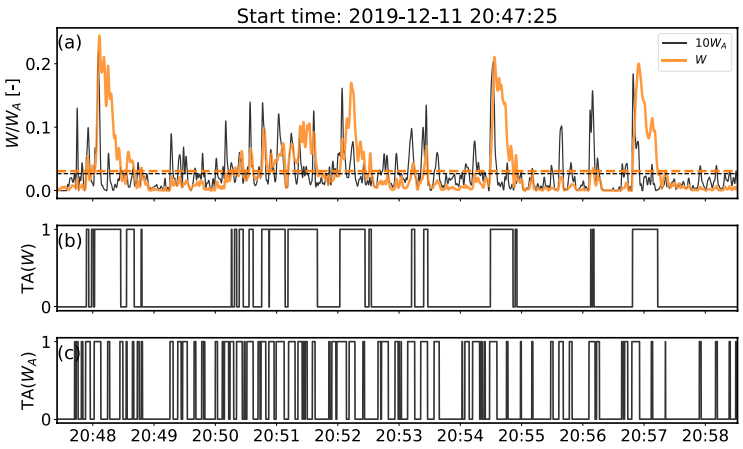

Figure 5. (a) Sample time series from the PAPA data set of the instantaneous total whitecap coverage W and the active whitecap coverage W_A, scaled by a factor of 10 to be visible on the same figure as W. See Figures 3d–3f for snapshots from the same record. The time mean levels of $\overline{W}$ and $10\overline{W_A}$ are marked with dashed lines. (b) The binary telegraph approximation (TA) time series of W, in which only mean-level zero-crossing information is retained while amplitude variations are ignored. (c) The TA time series of W_A.

as oceanic surface waves, include higher frequency resolution (due to the local nature of the intrinsic time scales represented by the IMFs) and its resilience against the impact of spurious harmonic wave components inherent in the Fourier spectral representation of nonlinear signals (Huang et al., 1999).

4.2. Intermittency Analysis

We investigate the intermittency of wave breaking in both the EKOK and PAPA data sets by analyzing the time variability of the whitecap coverage data. For this we employ the telegraphic approximation (TA) formalism on the instantaneous time series of W and W_A. The TA form of a time series is a binary sequence in which only the zero-crossing information is retained, while amplitude variations are disregarded (Sreenivasan & Bershadskii, 2006). The TA of a zero-mean time series $s(t)$ is defined as

$$\mathrm{TA}(s) = \frac{1}{2}\left(\frac{s(t)}{|s(t)|} + 1\right). \tag{9}$$

The TA time series assumes a value of one when the zero-level threshold is exceeded and zero otherwise. Examples of the TA of a record of coherent W and W_A time series from the PAPA data set are shown in Figure 5. Because the fractional whitecap coverage is a positive semi-definite quantity, we subtract the record mean before computing the TA time series of W and W_A.

It has been shown for various intermittent stochastic processes that the spectral density of the TA of a time series is related to the spectral density of the original series in regions where the original spectrum displays power-law behavior. Specifically, if the original spectrum decays as f^{-n}, then the spectrum of the TA series is expected to decay as f^{-m}, where

$$m = \frac{n+1}{2}. \tag{10}$$

For $n > 1$, $m < n$, which has been interpreted as an indication of the TA spectrum's higher memory content due to the decorrelating effect of amplitude variations on the original spectrum (Sreenivasan & Bershadskii, 2006).

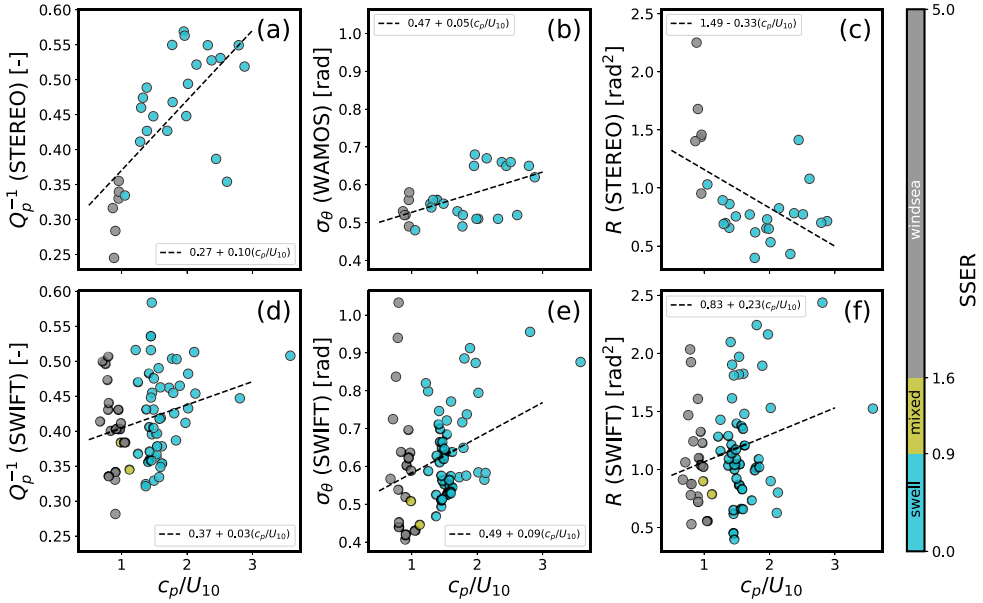

Figure 6. Various spectral width parameters from the two data sets as a function of the wave age c_p/U_{10}: (a) the spectral bandwidth in frequency estimated by Q_p^{-1}. (b) The directional spread σ_θ. (c) The multidirectionality coefficient $R = \sigma_\theta^2 Q_p^2/2$. The upper row relates to the EKOK data set, and the lower row relates to the PAPA data set. The dashed lines are the linear least-squares fits to the scatter plots. The scatter points are colored based on the sea-swell energy ratio of the wave energy spectra.

5. Results and Discussion

5.1. Wave Field Groupiness in the Field Data Sets

Figures 6 and 7 sum up the degree of groupiness of the wave fields encountered during the EKOK and PAPA video acquisition periods analyzed in this study. The comparisons of spectral width parameters against wave age c_p/U_{10} in Figures 6a and 6d, support the widely assumed relationship between spectral narrowness (i.e., low Q_p^{-1}) and young sea states, although the relationship appears more robust in the EKOK data set, collected in the North Sea, than in the North Pacific PAPA data set. This may reflect the bias of the JONSWAP parameterization toward fetch-limited sea states typical for the North Sea; however, the number of data points in the EKOK data set is too limited to draw confident conclusions on this matter. The directional spread σ_θ exhibits a similar, growing trend with aging seas in both data sets, but the multi-directionality parameter R displays inconsistent behavior between the data sets, owing mainly to the large range of directional spreads estimated from the SWIFT wave buoy motions in the PAPA data set.

Figure 7 compares the distributions of mean group duration T_g, normalized by the peak wave periods T_p, calculated with the IE and H_{rms} threshold methods in the two data sets (see Sections 4.1.1 and 4.1.2). The EKOK group durations are calculated from the stereo video mean sea surface elevation time series $\bar{\eta}$, and the PAPA group durations are computed from SWIFT buoy heave time series. Heave records from SWIFTs were not available at all video acquisition periods, however, and the lengths of individual heave time series ranged between 6 and 8 min. The EKOK wave groups display behavior consistent with the JONSWAP model, with prominent, long wave groups being somewhat more prevalent during sea states with narrow wave spectra in both frequency and directional spread. The PAPA group durations, on the other hand, display less consistency with the behavior expected and observed in the North Sea.

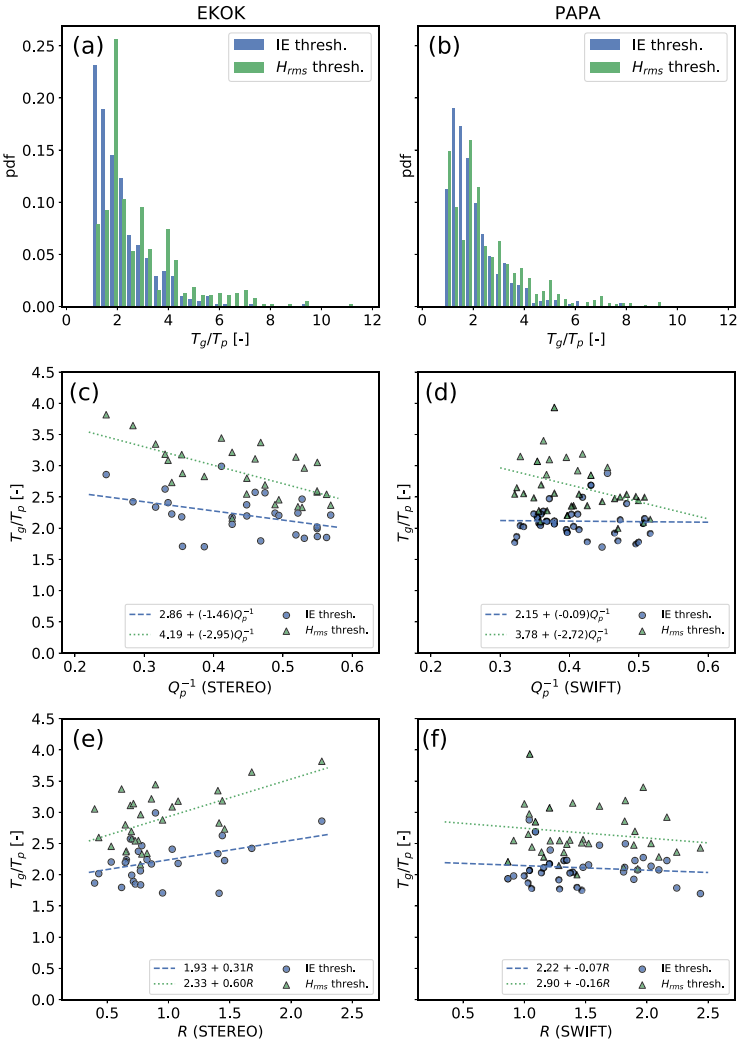

Figure 7. Left column: comparison of group durations in the EKOK data set defined by the Hilbert spectrum-based IE criterion of Veltcheva and Guedes Soares (2016) and the run-based H_{rms} criterion of Kimura (1980). (a) Histograms of the distributions of group durations T_g normalized by the peak periods T_p of the stereo video scalar spectra. (c) Normalized group durations as a function of the spectral bandwidth parameter Q_p^{-1}. (e) Normalized group durations as a function of the multidirectionality coefficient $R = \sigma_\theta^2 Q_p^2/2$, where the directional spread σ_θ is obtained from the WAMOS product, while Q_p is the peakedness of the stereo spectra. The dotted and dashed lines in (b) and (c) are the least-squares linear fits to the T_g/T_p scatter points. The right column shows the same parameters, estimated from the SWIFT buoy data in the PAPA data set.

5.2. Wave Group-Enhanced Breaking

5.2.1. Instantaneous W and W_A Distributions

Figure 8 shows the probability distributions of the instantaneous values of W and W_A spanning the full EKOK data set that coincide with wave groups detected in the time series of $\bar{\eta}$, versus W and W_A coinciding with the segments of $\bar{\eta}$ that fall between the wave groups, as illustrated in the example in Figure 4. The time series of instantaneous

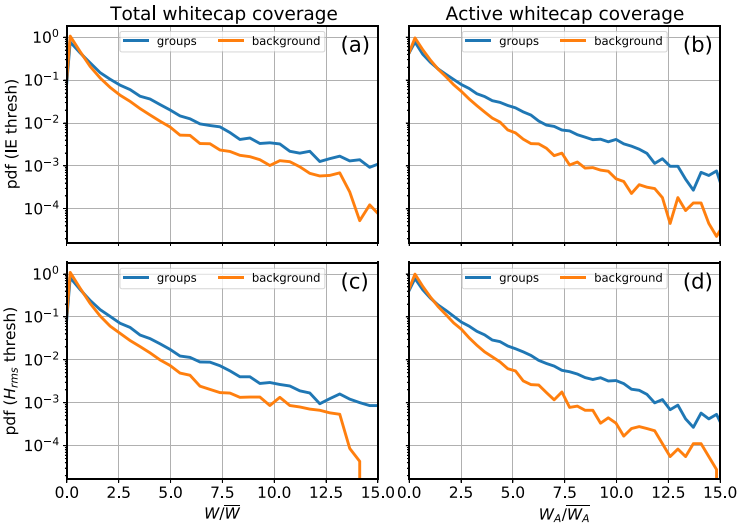

Figure 8. (a) and (c) Probability distributions of the relative instantaneous whitecap coverage $W/\overline{W}$ within the EKOK stereo camera footprint during wave group passage (blue curves) and between wave groups (orange curves). In (a) the wave groups are defined with the instantaneous wave energy (IE) threshold method, and in (c) the groups are defined as runs of high waves exceeding H_{rms} in height. (b) and (d) As in (a) and (c), but for the relative active whitecap coverage $W_A/\overline{W_A}$. The probability distributions are composed from all twenty-eight 20-min records in the EKOK data set, and truncated at relative whitecap coverage values of 15 to exclude the poorly sampled and noisy distribution tails.

W and W_A have been low-pass filtered with a 0.5-Hz cutoff in order to minimize the effects of high-frequency noise due to, for example, short-lived sun glints. To verify that the group-background distributions are insensitive to the choice of wave group definition, we show the results for both the run threshold-based group definition of Kimura (1980) and the IE-based group definition of Veltcheva and Guedes Soares (2007). Irrespective of the group definition employed, Figures 8a and 8c show that wave groups are associated with an approximately two to threefold enhancement of the probability of encountering elevated values of total whitecap coverage W relative to its record-wise mean value, $\overline{W}$. As shown in Figures 8b and 8d, this group-related enhancement in probability grows to approximately fivefold for high values of the relative active whitecap coverage $W_A/\overline{W_A}$.

The disparity between the W and W_A group-background distributions is likely to be influenced by our choice of method for W_A classification. We follow the approach of Schwendeman and Thomson (2015b), which isolates only the leading edges of propagating whitecaps. We argue that our estimates of W_A therefore provide a better indication of the initiation of breaking and maximum breaking extent (in terms of breaking crest length) than our estimates of W. The latter includes the influence of decaying foam patches that likely do not contribute to active breaking, but which, especially in instances of large-scale breaking events, may linger for several wave periods. As has been pointed out before (Mironov & Dulov, 2008), the total area of large whitecaps, the main contributor to the instantaneous value of W, may continue to grow for a period of time beyond the instant of maximum active breaking due to the dispersion and advection of the foam patch due to the orbital motion of the waves. For these reasons, elevated values of W may persist for several wave periods after the group that initiated the breaking has passed, whereas spikes in W_A effectively pinpoint the dominant wave-group phase at which the breaking is in its most active stage.

The consistently elevated probability of encountering high-amplitude values of W (indicative of large scale breaking events) during wave groups compared to between groups suggests that the prevalence of dominant wave breaking is related to the groupiness of the wave field, as reported in the early investigations of Donelan et al. (1972) and Holthuijsen and Herbers (1986). However, due to the variable decay rate of whitecaps, dependent on, for example, breaking strength (Callaghan et al., 2012), enhanced values of W may persist within the camera footprint for a longer period than the passage of wave groups, making it difficult to verify the true group-phase

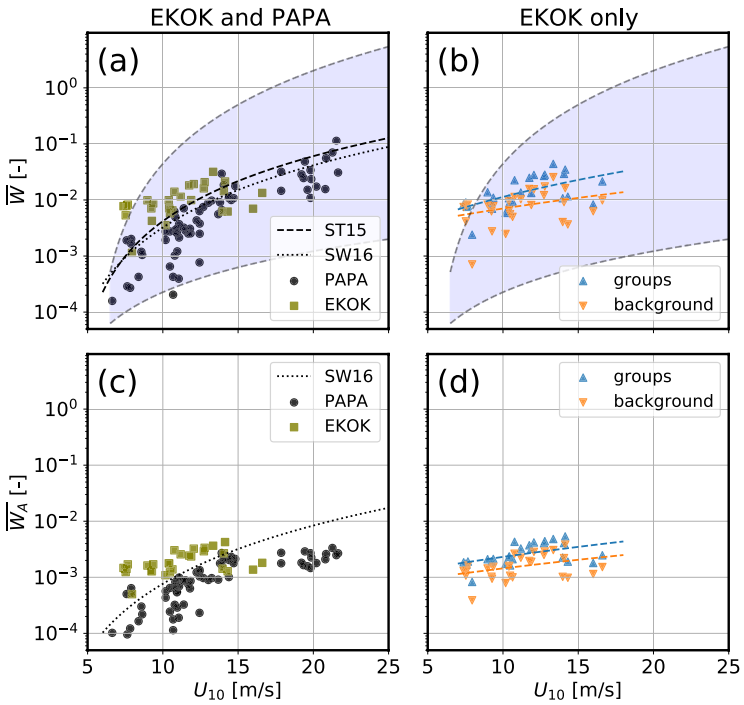

Figure 9. (a) Time-averaged total whitecap coverage $\overline{W}$ as a function of wind speed U_{10}, estimated from the PAPA image sequences (circles) and EKOK image sequences (squares). The dashed and dotted curves show the functional fits of ST15 (Schwendeman & Thomson, 2015b) and SW16 (Scanlon & Ward, 2016), respectively. The shading covers the reported 90% confidence interval around the ST15 fit. (b) The mean EKOK W values averaged during wave group passage (upward-pointing triangles) and between wave groups (downward-pointing triangles). The ST15 confidence interval is also included in shading. (c) The time-averaged active whitecap coverage $\overline{W_A}$ as a function of wind speed, with the Scanlon and Ward (2016) fit shown with the dotted curve. (d) As (b), but for the EKOK active whitecap coverage. The dashed lines in (b) and (d) are cubic fits of the form Equation 12 to the group/background data points. The wave group definition applied in (b) and (d) is the IE threshold method.

origin of all high W values in Figures 8a and 8c. However, the stronger group-related enhancement visible in the group versus background distributions of W_A (Figures 8b and 8d) suggest that the group modulation of breaking is a significant mechanism in determining breaking location in time and space. However, as seen in Figure 5, the amplitude of W_A may be a weaker indication of the full scale of breaking than the amplitude of W. This result likely follows from the W_A thresholding procedure which primarily isolates thin slices of the rapidly propagating, actively breaking crests (see Figure 3).

5.2.2. Time-Averaged W and W_A

Time-averaged values of W and W_A, denoted $\overline{W}$ and $\overline{W_A}$, are plotted in Figure 9 against the neutral 10-m wind speed U_{10}. The averaging periods for EKOK estimates of W and W_A are 20 min, while the variable-length PAPA estimates were averaged over periods ranging from 10 to 20 min. The PAPA wind speeds shown are 10-min averages. The mean total whitecap coverage $\overline{W}$ data points from both the EKOK and PAPA data sets, plotted in Figure 9a, are compared to empirical fits from two fairly recent studies, namely Schwendeman and Thomson (2015b; ST15) and Scanlon and Ward (2016; SW16). The ST15 fit was published with 90% confidence intervals, which are included in shading in Figure 9a. The ST15 data set was collected in the same geographic location as the PAPA data set using the same equipment and compiled with essentially the same processing methods. The ST15 fit was achieved with a generalized power-law function

$$\overline{W} = a(U_{10} - b)^n, \tag{11}$$

where $a = 2.81 \times 10^{-5}$, $b = 3.87$ m s^{-1}, and $n = 2.76$. Figure 9a shows a tendency of the PAPA data points to be biased somewhat below the ST15 fit. This may be related to our approach to the choice of pixel intensity threshold, which was intentionally conservative (meaning we generally applied high threshold values) in order to avoid false whitecap detection due to sun glints. The SW16 data set was collected in the North Atlantic and the Southern Ocean, and the fit of the data points of $\overline{W}$ against U_{10} was approximated with a cubic function of the form

$$\overline{W} = a(U_{10} - b)^3, \tag{12}$$

with $a = 7.84 \times 10^{-6}$ s^3 m^{-3} and $b = 2.56$ m s^{-1}. Because the SW16 fit generally lies below the ST15 fit, $\overline{W}$ data points in the PAPA data set generally correspond more closely to the SW16 fit (see Figure 9a). This is most apparent at high wind speeds ($U_{10} > 17$ m s^{-1}). The EKOK $\overline{W}$ data points, on the other hand, are in general biased higher than PAPA, especially for low wind speeds. While pixel-intensity threshold selection may influence the differences in magnitude of $\overline{W}$ between the data sets to some degree, it is reasonable to expect that the wind speed conversion from 102.3 to 10 m at EKOK is associated with markedly larger uncertainty than the 16-to-10 m conversion in the PAPA data set. Therefore, it is plausible that the U_{10} estimates are biased low rather than the $\overline{W}$ estimates being biased high at EKOK.

We remind the reader that the wind speeds U_{10} reported in this study are equivalent wind speeds for a neutrally stratified atmospheric boundary layer. While neutral winds are commonly used in whitecap coverage parameterizations (Brumer et al., 2017; Scanlon & Ward, 2016), it is known that stability effects may account for appreciable deviations of the true wind from the neutral estimate, especially at short timescales (Kara et al., 2008). Whilst a number of studies have investigated the effect of explicitly accounting for stability in $W(U_{10})$ parameterizations, the results have largely proved inconclusive on the significance of its impact (Monahan & Woolf, 1989; Paget et al., 2015). The whitecap data analyzed in this study were mainly collected in wind-forced conditions in the open ocean, with air-sea temperature differences associated with unstable or neutral atmospheric stratification (not shown). We therefore anticipate stability-related effects on our U_{10} estimates to be rather small, at least in comparison to the spread in the W estimates.

A physical factor worthy of consideration for the observed bias between the data sets is the difference in effective water depth between the geographical locations. Whereas the PAPA data set was collected in very deep water, the 70-m mean water depth at Ekofisk means that the dominant wave field is regularly in an intermediate water regime (Christensen et al., 2017). The topic of whether the depth-induced steepening of the dominant waves leads to more frequent wave breaking in the North Sea compared to the North Pacific is, however, outside the scope of the current study, and will be addressed in future work. Furthermore, despite the apparent bias between the $\bar{W}$ estimates in the two data sets, individual data points from both mostly remain confined within the 90% confidence intervals reported for the ST15 data set.

The time-averaged $\overline{W_A}$ estimates (Figure 9c) are compared to the SW16 fit, in which actively breaking whitecaps were separated manually from decaying remnant foam patches. The SW16 fit for W_A follows Equation 12 with $a = 1.39 \times 10^{-6}$ s^3 m^{-3} and $b = 1.80$ m s^{-1}. While our $\overline{W_A}$ estimates reasonably follow the ST16 fit for low-to-intermediate wind speeds, the higher-windspeed (> 15 m s^{-1}) $\overline{W_A}$ data points appear to flatten out and remain markedly below the ST16 curve. This behavior likely reflects our selected method for W_A detection (Schwendeman & Thomson, 2015b), which isolates fairly narrow regions of propagating whitecapping crests for very short durations (i.e., single frames). ST16, on the other hand, used the manual active breaker detection methodology described by Scanlon and Ward (2013), in which individual whitecaps are classified as either actively breaking or remnant foam based on the wave crest locations, the visual intensity and image texture. It was later found (Scanlon et al., 2016) that the active whitecap estimates thus calculated were a better match to the dissipation from breaking waves estimated by a wave model than the total whitecap coverage. Moreover, while the pixel "flipping" method for W_A detection was described by ST15, they did not report estimates of $\overline{W_A}$ made using the technique. The authors used the technique in a later study (Schwendeman & Thomson, 2017) to isolate breaking crests, but again no $\overline{W_A}$ estimates were reported. To our knowledge, Figure 9c is the first reported result in which the ST15 technique has been applied for producing estimates of $\overline{W_A}$.

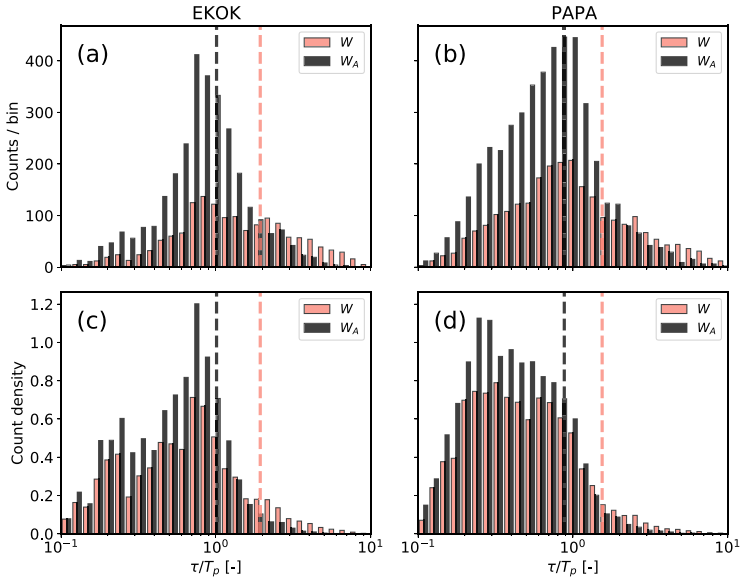

Figure 10. Histograms of the time periods τ between successive mean-level up-crossings of the time series of W and W_A, normalized by the prevailing peak wave periods T_p. The histograms are estimated with 30 logarithmically spaced bins between 0.1 and 10. Histograms relating to W are colored red and those relating to W_A are colored black. The mean τ/T_p values for W and W_A are marked with dashed red and black vertical lines, respectively. Results from the EKOK data set are shown in the left column, and PAPA results in the right column. The upper row (panels (a) and (b)) shows the number of values within each bin, and in the lower row (panels (c) and (d)), the counts per bin have been normalized by the product of the total number of counts and the variable bin width.

The right column of Figure 9 shows EKOK estimates of $\overline{W}$ and $\overline{W_A}$, in which the time averaging has been performed in versus between wave groups using the coherent time series of $\bar{\eta}$ from the stereo video reconstructions. As would be expected from the analysis of the instantaneous W and W_A estimates presented in Figure 8, the time-averaged values display clear wave group-induced enhancement. The apparent separation in magnitude of $\overline{W}$ and $\overline{W_A}$ when averaged during wave-group passage versus during quiescent periods suggests that the degree of wave field groupiness may be a source of the large scatter exhibited by previously reported whitecap coverage estimates (Anguelova & Webster, 2006; Brumer et al., 2017; Salisbury et al., 2013). Previous attempts at introducing wave field-dependent variables to W parameterizations have found only weak dependence of the variability of W and W_A with general wave field parameters (Albert et al., 2016; Brumer et al., 2017; Scanlon & Ward, 2016; Schwendeman & Thomson, 2015b). Our results presented in Figures 9b and 9d, however, demonstrate that wave field groupiness characteristics directly impact estimates of the whitecap coverage. Future studies may test the wave group effects on larger data sets by revisiting satellite measurements of W and controlling for wave field groupiness in terms of, for example, spectral bandwidth, peakedness, and directional spread using a spectral wave model.

5.3. Time Scales and Intermittency of the Whitecap Coverage

5.3.1. Inter-Breaking Periods

The time variability of wave breaking is investigated by analyzing the mean-level crossings of the low-pass filtered instantaneous time series of W and W_A. Since coherent sea-surface elevation records are not required for this analysis, this section includes results from both the EKOK and PAPA data sets. In Figure 10, we estimate the distributions of the time periods between consecutive mean-level up-crossings τ of the whitecap coverage records, normalized with the prevailing peak wave periods T_p, with logarithmically spaced histogram bins. The

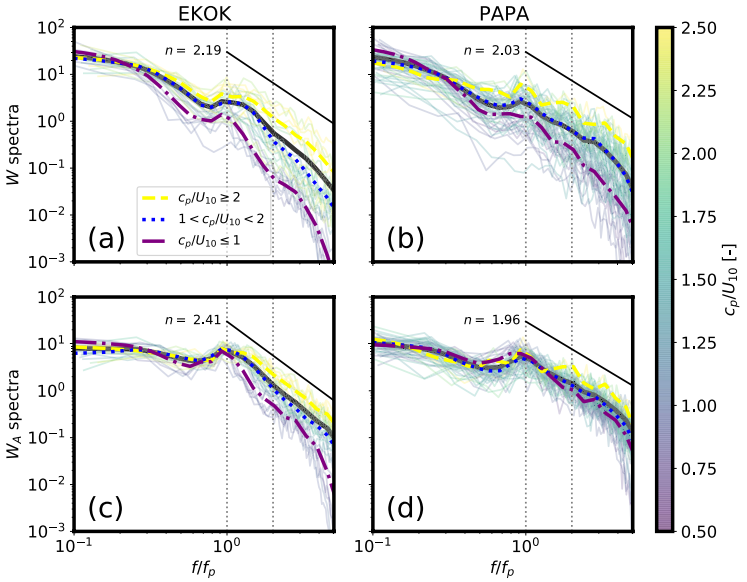

Figure 11. (a) and (b) Spectral densities of the instantaneous total whitecap coverage W. (c) and (d) Spectral densities of the instantaneous active whitecap coverage W_A. The spectra from the EKOK data set are in the left column, and the PAPA spectra are in the right column. The x axes are the spectral frequencies normalized by the peak wave frequencies f_p during each W and W_A acquisition period. The locations of $f/f_p = 1$ and $f/f_p = 2$ are marked with dotted vertical lines. The color scaling of the individual spectra (thin curves) indicates the prevailing wave age c_p/U_{10}. The thick solid curves (black) are the means of all individual spectra. The dashed yellow curves are the mean spectra for wave ages above 2, the dotted blue curves are the mean spectra for wave ages between 1 and 2, and the dash-dotted purple curves are the mean spectra for wave ages below 1. The steep decay of the young-sea spectra at high relative frequencies may be partly due to the low-pass filtering of the W and W_A time series at 0.5 Hz. The power-law fits to the full mean spectra above $f/f_p = 1$ are plotted with solid lines, with the power-law exponents n indicated next to the fit lines.

distributions displayed by counts per bin (Figures 10a and 10b) exhibit skewed unimodal or weakly bi-modal shapes, with mode values approximately at $\tau/T_p = 1$ or somewhat lower. In comparison, the mean τ/T_p values of all total whitecap coverage time series W are $\tau/T_p = 1.93$ and $\tau/T_p = 1.54$ for the EKOK and PAPA data sets, respectively. The equivalent mean values of all W_A time series are $\tau/T_p = 1.01$ and $\tau/T_p = 0.88$ for EKOK and PAPA, respectively. When the bin-wise counts are normalized by the products of the total number of counts and the variable bin widths (Figures 10c and 10d), the distributions assume more bi-modal shapes, with modes skewed at even lower values of τ/T_p.

The tendency of the instantaneous W_A records to exhibit mean-upcrossings at a frequency very near the peak wave frequency supports results from previous studies showing preferential breaking of shorter wave components at the crests of dominant waves (Dulov et al., 2002; Yurovsky et al., 2017). The nearly twofold difference in the mean values of τ/T_p between W and W_A in both data sets suggests that the mean-upcrossings of W_A capture a larger portion of small-scale breaking occurring during or between large-scale or high-impact breaking events than the mean-upcrossings of W, in which clusters of elevated values may persist for several wave periods as a result of slowly dissipating foam patches which may mask smaller-scale intermediate breaking events (see the example time series in Figure 5). Moreover, the mean-upcrossings of W display similar periodicity to the observations of Donelan et al. (1972), who observed dominant waves breaking at a frequency related to approximately twice the peak wave period.

5.3.2. Spectral Density of W and W_A

A spectral representation of the whitecap coverage is shown in Figure 11, where frequency spectra are estimated from each individual time series of instantaneous W and W_A in both the EKOK and PAPA data sets, and colored

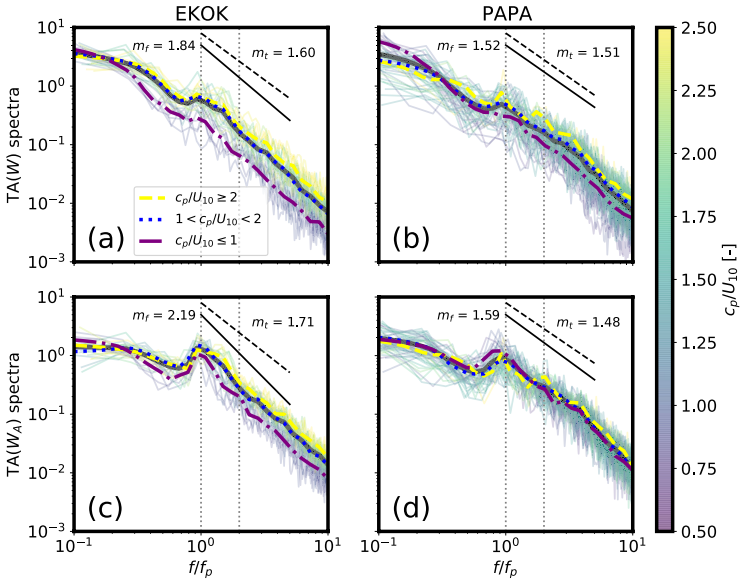

Figure 12. As Figure 11, but for spectra of the TA of the total whitecap coverage W (upper row), and spectra of the TA of the active whitecap coverage W_A (lower row). Color scaling as in Figure 11. The solid lines are the power-law fits to the mean TA spectra (solid black curves) in the tail region between $f/f_p = 1$ and 2 (same interval as in Figure 11), with slopes indicated by m_f. The dashed lines are the theoretical power-law slopes based on the spectral slopes n in Figure 11 as predicted by Equation 10, with theoretical slope coefficients indicated by m_t.

according to the wave age of the underlying sea state. As shown in Figure 11a and 11b, the individual W spectra in both data sets exhibit considerable scatter. A few distinguishing features can, however, be identified from the mean spectra classified by wave age intervals. The high energy content at the lowest frequencies visible in all mean W spectra is most likely due to the slow decay of large foam patches from large scale breaking events. At all wave ages a secondary peak, or at least a flattening of the spectral slope, is visible close to the peak wave frequency. The secondary peak is followed by decaying spectral density with a tendency toward power-law behavior, although the spectral tail slopes display some variation across wave ages and data sets. At the highest relative frequencies, the slopes of the young sea spectra may be somewhat affected by the low-pass filtering of the W and W_A time series at 0.5 Hz. The high wave age ($c_p/U_{10} \geq 2$) mean W spectrum in the PAPA data set also appears to have a third peak at approximately $f/f_p = 2$; however, the significance of this third peak is questionable, as the high wave age mean spectrum of the PAPA data set is averaged over only four separate spectra. The estimated power-law fits to the $f/f_p > 1$ regions of the total mean spectra are also included in Figures 11a and 11b, with power-law exponents $n = 2.19$ and 2.03 for the EKOK and PAPA mean W spectra, respectively.

The W_A spectra (Figures 11c and 11d) display a more pronounced peak at $f/f_p = 1$, reflecting the more localized nature of the W_A estimate, in which breaking events are characterized by short-lived spikes focused at the points in time when the breaking crests attain their maximum extent. Compared to the W spectra, the W_A spectra also display somewhat less scatter at high frequencies. The power-law exponents of the mean W_A spectra are estimated as $n = 2.41$ and $n = 1.96$ for EKOK and PAPA, respectively.

5.3.3. Intermittency Spectra

A complementary representation to the whitecap coverage spectra in Figure 11 is shown in Figure 12 with the spectral densities of the TA of the W and W_A time series. Since the TA representation only retains information of the time separation between successive crossings of the mean W and W_A levels, such that the de-correlating effects of amplitude variations are minimized, previously published results on general stochastic processes (Cava et al., 2012; Sreenivasan & Bershadskii, 2006) give reason to expect that the TA spectra exhibit more consistency

than the W and W_A spectra shown in Figure 11. Indeed, this behavior is evident, especially in the tail regions of all TA spectra, where the spectral slopes display less variation with wave age, and the power-law behavior extends to higher relative frequencies than in the W and W_A spectra. The spectral peak at the peak wave frequency is also pronounced, especially in the TA spectra of W_A, shown in Figures 12c and 12d. The fitted power-law exponents m_f of all mean TA spectra show reasonable agreement with the theoretical slopes m_t, predicted by the relationship in Equation 10, suggesting that the intermittency characteristics of W and W_A are of a similar nature to other stochastic processes occurring in both natural and controlled environments.

5.3.4. Comparison to Prior Observations

The analyses of the time scales of breaking presented in this section point toward a universal breaking at a period that is closely linked to the period of the dominant waves. This supports the amplitude analysis presented in Section 5.2, which showed enhanced breaking activity linked to the passage of energetic wave groups. Dominant wave crests have also been shown to be the preferential breaking regions for waves of various scales in previous field studies (Donelan et al., 1972; Dulov et al., 2002, 2021; Holthuijsen & Herbers, 1986; Yurovsky et al., 2017). A marked contrast exists, however, between the magnitude of long wave modulation of wave breaking in our results, which show a 2–5 fold enhancement of breaking probability attributed to wave groups, compared to those of Dulov et al. (2002, 2021) who found modulation factors as high as 20–24. It is, however, important to keep in mind that our analysis sorts long waves into two categories, namely wave groups and the "background" wave field. Both of these categories consist of dominant waves, a portion of which are related to wave breaking of varying scales as shown in Figure 4. The analyses of Dulov et al. (2002, 2021), on the other hand, examine the modulation of breaking by long waves irrespective of their amplitude and group structure. With this in mind, our results should be viewed as complementary, not contradictory, to those of Dulov et al. (2002, 2021).

It is important to note that our analysis presented herein is relatively ambiguous regarding the scale (e.g., spatial extent or breaking strength) of the breaking that occurs at dominant wave-related periodicity. Previous studies on the distributions of crest-lengths per unit area and crest propagation speed have found that dominant-wave breaking accounts for only a fraction of the total breaking rate in typical wind-forced sea states, with the majority of breaking occurring at much shorter wave scales with mean breaking crests speeds typically of the order of half the phase speeds of peak waves or less (Kleiss & Melville, 2010; Romero, 2019; Schwendeman et al., 2014; Thomson et al., 2009). Our results should not be considered contradictory to these previous findings, but should be viewed as further evidence that dominant-wave modulation is an important mechanism in driving wave breaking at a wide range of scales.

6. Conclusions

We have analyzed the variability of high-temporal resolution oceanic whitecap coverage with the underlying dominant wave group structure using stereo video observations from a platform in the central North Sea. The observations show enhanced probability of occurrence of high instantaneous whitecap coverage coincident with wave group passage, which implies that wave groupiness is associated with larger scale wave breaking activity and extent (Figure 8). The group enhancement of the whitecap coverage is apparent both in the instantaneous total whitecap coverage W and the whitecap coverage related to actively breaking wave crests W_A, although the difference between intra-group and inter-group whitecap coverage is more pronounced for W_A (approximately threefold for W vs. a fivefold enhancement for W_A). This result was shown to be insensitive to the specific definition used to distinguish wave groups from the background sea state. Wave groups were also shown to lead to enhanced values of time-averaged W and W_A compared to quiescent periods. This result suggests that wave field groupiness may be a source of scatter among previously published whitecap coverage data sets.

Analyses of the time variability of the instantaneous W and W_A data showed a tendency toward periodicity at time scales near the peak wave period, supporting previous observations of preferential breaking of short wave components near the crests of long waves. The consistency of this result was substantiated by the inclusion of a second whitecap coverage field data set collected with ship-based video cameras in a wide range of environmental conditions in the North Pacific.

Data Availability Statement

Data will be posted at https://digital.lib.washington.edu/researchworks/handle/1773/48143. Whitecap thresholding and ship motion correction codes used in the analysis can be found at https://github.com/mikapm/ship-whitecaps.

Acknowledgments
Mika Petteri Malila received funding from the Valle Foundation for a scientific stay at the University of Washington in 2019–2020. The Ekofisk stereo camera system was installed with support from the funding partners ConocoPhillips Norway and Equinor ASA through the StereoWave joint industry project which we gratefully acknowledge. Additional funding was provided by the European Union's Horizon 2020 Research and 391 Innovation Programme under grant agreement 821 001. We would like to express our gratitude to Lars Bahr (ConocoPhillips Norway) for his tireless technical support. The image processing was in part carried out on the post-processing infrastructure of the Norwegian Meteorological Institute. Our thanks to Nico Budewitz and Roger Storvik for their continued support. We also wish to thank the captain and crew of R/V Sikuliaq, as well as APL-UW field engineers Joe Talbert and Alex de Klerk, for their help in collecting the North Pacific cruise data.

References

Adcock, T. A. A., Taylor, P. H., Yan, S., Ma, Q. W., & Janssen, P. A. E. M. (2011). Did the Draupner wave occur in a crossing sea? *Proceedings of the Royal Society A: Mathematical, Physical & Engineering Sciences*, *467*(2134), 3004–3021. https://doi.org/10.1098/rspa.2011.0049

Agrawal, Y. C., Terray, E. A., Donelan, M. A., Hwang, P. A., Williams, A. J., Drennan, W. M., et al. (1992). Enhanced dissipation of kinetic energy beneath surface waves. *Nature*, *359*(6392), 219–220. https://doi.org/10.1038/359219a0

Albert, M. F., Anguelova, M. D., Manders, A. M., Schaap, M., & de Leeuw, G. (2016). Parameterization of oceanic whitecap fraction based on satellite observations. *Atmospheric Chemistry and Physics*, *16*(21), 13725–13751. https://doi.org/10.5194/acp-16-13725-2016

Anguelova, M. D., & Webster, F. (2006). Whitecap coverage from satellite measurements: A first step toward modeling the variability of oceanic whitecaps. *Journal of Geophysical Research: Oceans*, *111*(C3). https://doi.org/10.1029/2005jc003158

Babanin, A. V. (2011). *Breaking and dissipation of ocean surface waves*. Cambridge University Press.

Babanin, A. V., Chalikov, D., Young, I., & Savelyev, I. (2007). Predicting the breaking onset of surface water waves. *Geophysical Research Letters*, *34*(7). https://doi.org/10.1029/2006gl029135

Babanin, A. V., Waseda, T., Kinoshita, T., & Toffoli, A. (2011). Wave breaking in directional fields. *Journal of Physical Oceanography*, *41*(1), 145–156. https://doi.org/10.1175/2010jpo4455.1

Banner, M. L., Babanin, A. V., & Young, I. R. (2000). Breaking probability for dominant waves on the sea surface. *Journal of Physical Oceanography*, *30*(12), 3145–3160. https://doi.org/10.1175/1520-0485(2000)030<3145:BPFDWO>2.0.CO;2

Banner, M. L., & Melville, W. K. (1976). On the separation of air flow over water waves. *Journal of Fluid Mechanics*, *77*(4), 825–842. https://doi.org/10.1017/s0022112076002905

Banner, M. L., & Peirson, W. L. (2007). Wave breaking onset and strength for two-dimensional deep-water wave groups. *Journal of Fluid Mechanics*, *585*, 93–115. https://doi.org/10.1017/s0022112007006568

Barthelemy, X., Banner, M. L., Peirson, W. L., Fedele, F., Allis, M., & Dias, F. (2018). On a unified breaking onset threshold for gravity waves in deep and intermediate depth water. *Journal of Fluid Mechanics*, *841*, 463–488. https://doi.org/10.1017/jfm.2018.93

Benetazzo, A. (2006). Measurements of short water waves using stereo matched image sequences. *Coastal Engineering*, *53*(12), 1013–1032. https://doi.org/10.1016/j.coastaleng.2006.06.012

Benetazzo, A., Fedele, F., Gallego, G., Shih, P.-C., & Yezzi, A. (2012). Offshore stereo measurements of gravity waves. *Coastal Engineering*, *64*, 127–138. https://doi.org/10.1016/j.coastaleng.2012.01.007

Benjamin, T. B., & Feir, J. E. (1967). The disintegration of wave trains on deep water. *Journal of Fluid Mechanics*, *27*(3), 417–430. https://doi.org/10.1017/s002211206700045x

Bergamasco, F., Torsello, A., Sclavo, M., Barbariol, F., & Benetazzo, A. (2017). Wass: An open-source pipeline for 3D stereo reconstruction of ocean waves. *Computers & Geosciences*, *107*, 28–36. https://doi.org/10.1016/j.cageo.2017.07.001

Bitner-Gregersen, E. M., & Gran, S. (1983). Local properties of sea waves derived from a wave record. *Applied Ocean Research*, *5*(4), 210–214. https://doi.org/10.1016/0141-1187(83)90035-4

Brumer, S. E., Zappa, C. J., Brooks, I. M., Tamura, H., Brown, S. M., Blomquist, B. W., et al. (2017). Whitecap coverage dependence on wind and wave statistics as observed during SO GasEx and HiWinGS. *Journal of Physical Oceanography*, *47*(9), 2211–2235. https://doi.org/10.1175/jpo-d-17-0005.1

Buckley, M. P., & Veron, F. (2016). Structure of the airflow above surface waves. *Journal of Physical Oceanography*, *46*(5), 1377–1397. https://doi.org/10.1175/jpo-d-15-0135.1

Callaghan, A. H., Deane, G. B., Stokes, M. D., & Ward, B. (2012). Observed variation in the decay time of oceanic whitecap foam. *Journal of Geophysical Research: Oceans*, *117*(C9). https://doi.org/10.1029/2012jc008147

Cava, D., Katul, G. G., Molini, A., & Elefante, C. (2012). The role of surface characteristics on intermittency and zero-crossing properties of atmospheric turbulence. *Journal of Geophysical Research: Atmospheres*, *117*(D1). https://doi.org/10.1029/2011jd016167

Chella, M. A., Tørum, A., & Myrhaug, D. (2012). An overview of wave impact forces on offshore wind turbine substructures. *Energy Procedia*, *20*, 217–226. https://doi.org/10.1016/j.egypro.2012.03.022

Christensen, K. H., Carrasco, A., Bidlot, J.-R., & Breivik, Ø. (2017). The "shallow-waterness" of the wave climate in European coastal regions. *Ocean Science*, *13*(4), 589–597. https://doi.org/10.5194/os-13-589-2017

Derakhti, M., & Kirby, J. T. (2016). Breaking-onset, energy and momentum flux in unsteady focused wave packets. *Journal of Fluid Mechanics*, *790*, 553–581. https://doi.org/10.1017/jfm.2016.17

Derakhti, M., Kirby, J. T., Banner, M. L., Grilli, S. T., & Thomson, J. (2020). A unified breaking onset criterion for surface gravity water waves in arbitrary depth. *Journal of Geophysical Research: Oceans*, *125*(7), e2019JC015886. https://doi.org/10.1029/2019jc015886

Derakhti, M., Thomson, J., & Kirby, J. T. (2020). Sparse sampling of intermittent turbulence generated by breaking surface waves. *Journal of Physical Oceanography*, *50*(4), 867–885. https://doi.org/10.1175/jpo-d-19-0138.1

Donelan, M. A., Drennan, W. M., & Magnusson, A. K. (1996). Nonstationary analysis of the directional properties of propagating waves. *Journal of Physical Oceanography*, *26*(9), 1901–1914. https://doi.org/10.1175/1520-0485(1996)026<1901:NAOTDP>2.0.CO;2

Donelan, M. A., Hamilton, J., & Hui, W. (1985). Directional spectra of wind-generated ocean waves. *Proceedings of the Royal Society A: Mathematical, Physical & Engineering Sciences*, *315*(1534), 509–562.

Donelan, M. A., Haus, B. K., Plant, W. J., & Troianowski, O. (2010). Modulation of short wind waves by long waves. *Journal of Geophysical Research: Oceans*, *115*(C10). https://doi.org/10.1029/2009jc005794

Donelan, M. A., Longuet-Higgins, M. S., & Turner, J. S. (1972). Periodicity in whitecaps. *Nature*, *239*(5373), 449–451. https://doi.org/10.1038/239449a0

Dulov, V. A., Korinenko, A. E., Kudryavtsev, V. N., & Malinovsky, V. V. (2021). Modulation of wind-wave breaking by long surface waves. *Remote Sensing*, *13*(14), 2825. https://doi.org/10.3390/rs13142825

Dulov, V. A., Kudryavtsev, V. N., & Bol'shakov, A. N. (2002). A field study of whitecap coverage and its modulations by energy containing surface waves. In M. A. Donelan, W. M. Drennan, E. S. Saltzman, & R. Wanninkhof, (Eds.), *Gas transfer at water surfaces* (Vol. 127, pp. 187–192). American Geophysical Union.

Dysthe, K., Krogstad, H. E., & Müller, P. (2008). Oceanic rogue waves. *Annual Review of Fluid Mechanics*, *40*(1), 287–310. https://doi.org/10.1146/annurev.fluid.40.111406.102203

Fairall, C. W., Bradley, E. F., Hare, J. E., Grachev, A. A., & Edson, J. B. (2003). Bulk parameterization of air–sea fluxes: Updates and verification for the COARE algorithm. *Journal of Climate*, *16*(4), 571–591. https://doi.org/10.1175/1520-0442(2003)016<0571:BPOASF>2.0.CO;2

Fedele, F., Brennan, J., De León, S. P., Dudley, J., & Dias, F. (2016). Real world ocean rogue waves explained without the modulational instability. *Scientific Reports*, *6*, 27715. https://doi.org/10.1038/srep27715

Funke, E. R., & Mansard, E. P. D. (1980). On the synthesis of realistic sea states. *Coastal Engineering*, *1980*, 2974–2991. https://doi.org/10.1061/9780872622647.179

Furevik, B. R., & Haakenstad, H. (2012). Near-surface marine wind profiles from rawinsonde and NORA10 hindcast. *Journal of Geophysical Research: Atmospheres*, *117*(D23). https://doi.org/10.1029/2012jd018523

Gemmrich, J. R., & Farmer, D. M. (1999). Observations of the scale and occurrence of breaking surface waves. *Journal of Physical Oceanography*, *29*(10), 2595–2606. https://doi.org/10.1175/1520-0485(1999)029<2595:ootsao>2.0.co;2

Goda, Y. (1970). Numerical experiments on wave statistics with spectral simulation. *Report of the Port and Harbour Research Institute*, *9*, 3–57.

Guimaraes, P. V. (2018). *Sea surface and energy dissipation* (Unpublished doctoral dissertation). Université Bretagne Loire; École Centrale de Nantes.

Hasselmann, K. F., Barnett, T. P., Bouws, E., Carlson, H., Cartwright, D. E., Enke, K., et al. (1973). Measurements of wind-wave growth and swell decay during the joint North Sea wave project (JONSWAP). *Ergaenzungsheft zur Deutschen Hydrographischen Zeitschrift Reihe*, *A8*(12), 95.

Herbers, T. H. C., Jessen, P. F., Janssen, T. T., Colbert, D. B., & MacMahan, J. H. (2012). Observing ocean surface waves with GPS-tracked buoys. *Journal of Atmospheric and Oceanic Technology*, *29*(7), 944–959. https://doi.org/10.1175/jtech-d-11-00128.1

Holthuijsen, L. H. (2007). *Waves in oceanic and coastal waters*. Cambridge University Press.

Holthuijsen, L. H., & Herbers, T. H. C. (1986). Statistics of breaking waves observed as whitecaps in the open sea. *Journal of Physical Oceanography*, *16*(2), 290–297. https://doi.org/10.1175/1520-0485(1986)016<0290:sobwoa>2.0.co;2

Huang, K. Y., Katul, G. G., & Hultmark, M. (2021). Velocity and temperature dissimilarity in the surface layer uncovered by the telegraph approximation. *Boundary-Layer Meteorology*, *1–21*. https://doi.org/10.1007/s10546-021-00632-2

Huang, N. E., Shen, Z., & Long, S. R. (1999). A new view of nonlinear water waves: The Hilbert spectrum. *Annual Review of Fluid Mechanics*, *31*(1), 417–457. https://doi.org/10.1146/annurev.fluid.31.1.417

Huang, N. E., Shen, Z., Long, S. R., Wu, M. C., Shih, H. H., Zheng, Q., et al. (1998). The empirical mode decomposition and the Hilbert spectrum for nonlinear and non-stationary time series analysis. *Proceedings of the Royal Society A: Mathematical, Physical & Engineering Sciences*, *454*(1971), 903–995. https://doi.org/10.1098/rspa.1998.0193

Jähne, B., Klinke, J., & Waas, S. (1994). Imaging of short ocean wind waves: A critical theoretical review. *Journal of the Optical Society of America A*, *11*(8), 2197–2209.

Janssen, P. A. E. M., & Bidlot, J.-R. (2009). *On the extension of the freak wave warning system and its verification*. European Centre for Medium-Range Weather Forecasts.

Kara, A. B., Wallcraft, A. J., & Bourassa, M. A. (2008). Air-sea stability effects on the 10 m winds over the global ocean: Evaluations of air-sea flux algorithms. *Journal of Geophysical Research: Oceans*, *113*(C4). https://doi.org/10.1029/2007jc004324

Kimura, A. (1980). Statistical properties of random wave groups. *Coastal Engineering*, *1980*, 2955–2973. https://doi.org/10.1061/9780872622647.178

Kleiss, J. M., & Melville, W. K. (2010). Observations of wave breaking kinematics in fetch-limited seas. *Journal of Physical Oceanography*, *40*(12), 2575–2604. https://doi.org/10.1175/2010JPO4383.1

Kleiss, J. M., & Melville, W. K. (2011). The analysis of sea surface imagery for whitecap kinematics. *Journal of Atmospheric and Oceanic Technology*, *28*(2), 219–243. https://doi.org/10.1175/2010JTECHO744.1

Komen, G. J., Cavaleri, L., Donelan, M. A., Hasselmann, K., Hasselmann, S., & Janssen, P. A. E. M. (1994). *Dynamics and modelling of ocean waves*. Cambridge University Press.

Kudryavtsev, V., & Chapron, B. (2016). On growth rate of wind waves: Impact of short-scale breaking modulations. *Journal of Physical Oceanography*, *46*(1), 349–360.

Kuik, A. J., Van Vledder, G. P., & Holthuijsen, L. H. (1988). A method for the routine analysis of pitch-and-roll buoy wave data. *Journal of Physical Oceanography*, *18*(7), 1020–1034. https://doi.org/10.1175/1520-0485(1988)018<1020:AMFTRA>2.0.CO;2

Longuet-Higgins, M. S. (1975). On the joint distribution of the periods and amplitudes of sea waves. *Journal of Geophysical Research*, *80*(18), 2688–2694. https://doi.org/10.1029/jc080i018p02688

Longuet-Higgins, M. S. (1984). Statistical properties of wave groups in a random sea state. *Proceedings of the Royal Society A: Mathematical, Physical & Engineering Sciences*, *312*(1521), 219–250.

Longuet-Higgins, M. S., & Stewart, R. W. (1960). Changes in the form of short gravity waves on long waves and tidal currents. *Journal of Fluid Mechanics*, *8*(4), 565–583. https://doi.org/10.1017/S0022112060000803

Longuet-Higgins, M. S., & Stewart, R. W. (1964). Radiation stress in water waves: A physical discussion with application. *Deep-Sea Research*, *11*, 529–562. https://doi.org/10.1016/0011-7471(64)90001-4

Magnusson, A. K., & Donelan, M. A. (2013). The Andrea wave characteristics of a measured North Sea rogue wave. *Journal of Offshore Mechanics and Arctic Engineering*, *135*(3). https://doi.org/10.1115/1.4023800

Manaster, A., Ricciardulli, L., & Meissner, T. (2019). Validation of high ocean surface winds from satellites using oil platform anemometers. *Journal of Atmospheric and Oceanic Technology*, *36*(5), 803–818. https://doi.org/10.1175/jtech-d-18-0116.1

Melville, W. K. (1996). The role of surface-wave breaking in air-sea interaction. *Annual Review of Fluid Mechanics*, *28*(1), 279–321. https://doi.org/10.1146/annurev.fl.28.010196.001431

Michell, J. H. (1893). On the highest waves in water. *The London, Edinburgh, and Dublin Philosophical Magazine and Journal of Science*, *36*(222), 430–437. https://doi.org/10.1080/14786449308620499

Mironov, A. S., & Dulov, V. A. (2008). Detection of wave breaking using sea surface video records. *Measurement Science and Technology*, *19*(1), 015405. https://doi.org/10.1088/0957-0233/19/1/015405

Monahan, E. C., & O'Muircheartaigh, I. G. (1986). Whitecaps and the passive remote sensing of the ocean surface. *International Journal of Remote Sensing*, *7*(5), 627–642. https://doi.org/10.1080/01431168608954716

Monahan, E. C., & Woolf, D. K. (1989). Comments on "variations of whitecap coverage with wind stress and water temperature. *Journal of Physical Oceanography*, *19*(5), 706–709. https://doi.org/10.1175/1520-0485(1989)019<0706:COOWCW>2.0.CO;2

Paget, A. C., Bourassa, M. A., & Anguelova, M. D. (2015). Comparing in situ and satellite-based parameterizations of oceanic whitecaps. *Journal of Geophysical Research: Oceans*, *120*(4), 2826–2843. https://doi.org/10.1002/2014jc010328

Perlin, M., Choi, W., & Tian, Z. (2013). Breaking waves in deep and intermediate waters. *Annual Review of Fluid Mechanics*, *45*, 115–145. https://doi.org/10.1146/annurev-fluid-011212-140721

Phillips, O. M. (1985). Spectral and statistical properties of the equilibrium range in wind-generated gravity waves. *Journal of Fluid Mechanics*, *156*, 505–531. https://doi.org/10.1017/s0022112085002221

Reichert, K., Hessner, K., Nieto Borge, J. C., & Dittmer, J. (1999). WaMoS II: A radar based wave and current monitoring system. *Paper presented at the the ninth international offshore and polar engineering conference, Brest, France*.

Reul, N., Branger, H., & Giovanangeli, J.-P. (2008). Air flow structure over short-gravity breaking water waves. *Boundary-Layer Meteorology*, *126*(3), 477–505. https://doi.org/10.1007/s10546-007-9240-3

Romero, L. (2019). Distribution of surface wave breaking fronts. *Geophysical Research Letters*, *46*(17–18), 10463–10474. https://doi.org/10.1029/2019gl083408

Saket, A., Peirson, W. L., Banner, M. L., Barthelemy, X., & Allis, M. J. (2017). On the threshold for wave breaking of two-dimensional deep water wave groups in the absence and presence of wind. *Journal of Fluid Mechanics*, *811*, 642–658. https://doi.org/10.1017/jfm.2016.776

Salisbury, D. J., Anguelova, M. D., & Brooks, I. M. (2013). On the variability of whitecap fraction using satellite-based observations. *Journal of Geophysical Research: Oceans*, *118*(11), 6201–6222. https://doi.org/10.1002/2013jc008797

Scanlon, B., Breivik, Ø., Bidlot, J.-R., Janssen, P. A. E. M., Callaghan, A. H., & Ward, B. (2016). Modeling whitecap fraction with a wave model. *Journal of Physical Oceanography*, *46*, 887–894. https://doi.org/10.1175/JPO-D-15-0158.1

Scanlon, B., & Ward, B. (2013). Oceanic wave breaking coverage separation techniques for active and maturing whitecaps. *Methods in Oceanography*, *8*, 1–12. https://doi.org/10.1016/j.mio.2014.03.001

Scanlon, B., & Ward, B. (2016). The influence of environmental parameters on active and maturing oceanic whitecaps. *Journal of Geophysical Research: Oceans*, *121*(5), 3325–3336. https://doi.org/10.1002/2015jc011230

Schwendeman, M. S., & Thomson, J. (2015a). A horizon-tracking method for shipboard video stabilization and rectification. *Journal of Atmospheric and Oceanic Technology*, *32*(1), 164–176. https://doi.org/10.1175/jtech-d-14-00047.1

Schwendeman, M. S., & Thomson, J. (2015b). Observations of whitecap coverage and the relation to wind stress, wave slope, and turbulent dissipation. *Journal of Geophysical Research: Oceans*, *120*(12), 8346–8363. https://doi.org/10.1002/2015jc011196

Schwendeman, M. S., & Thomson, J. (2017). Sharp-crested breaking surface waves observed from a ship-based stereo video system. *Journal of Physical Oceanography*, *47*(4), 775–792. https://doi.org/10.1175/jpo-d-16-0187.1

Schwendeman, M. S., Thomson, J., & Gemmrich, J. R. (2014). Wave breaking dissipation in a young wind sea. *Journal of Physical Oceanography*, *44*(1), 104–127. https://doi.org/10.1175/jpo-d-12-0237.1

Smith, M. J., Poulter, E. M., & McGregor, J. A. (1996). Doppler radar measurements of wave groups and breaking waves. *Journal of Geophysical Research: Oceans*, *101*(C6), 14269–14282. https://doi.org/10.1029/96jc00766

Song, J.-B., & Banner, M. L. (2002). On determining the onset and strength of breaking for deep water waves. Part I: Unforced irrotational wave groups. *Journal of Physical Oceanography*, *32*(9), 2541–2558. https://doi.org/10.1175/1520-0485-32.9.2541

Sreenivasan, K. R., & Bershadskii, A. (2006). Clustering properties in turbulent signals. *Journal of Statistical Physics*, *125*(5), 1141–1153. https://doi.org/10.1007/s10955-006-9112-0

Stokes, G. G. (1880). *On the theory of oscillatory waves*. Transactions of the Cambridge Philosophical Society.

Sutherland, P., & Melville, W. K. (2015). Field measurements of surface and near-surface turbulence in the presence of breaking waves. *Journal of Physical Oceanography*, *45*(4), 943–965. https://doi.org/10.1175/jpo-d-14-0133.1

Terray, E. A., Donelan, M. A., Agrawal, Y. C., Drennan, W. M., Kahma, K. K., Williams, A. J., et al. (1996). Estimates of kinetic energy dissipation under breaking waves. *Journal of Physical Oceanography*, *26*(5), 792–807. https://doi.org/10.1175/1520-0485(1996)026<0792:EOKEDU>2.0.CO;2

Terrill, E., & Melville, W. K. (1997). Sound-speed measurements in the surface-wave layer. *Journal of the Acoustical Society of America*, *102*(5), 2607–2625. https://doi.org/10.1121/1.420315

Thomson, J. (2012). Wave breaking dissipation observed with "SWIFT" drifters. *Journal of Atmospheric and Oceanic Technology*, *29*(12), 1866–1882. https://doi.org/10.1175/JTECH-D-12-00018.1

Thomson, J., Gemmrich, J. R., & Jessup, A. T. (2009). Energy dissipation and the spectral distribution of whitecaps. *Geophysical Research Letters*, *36*(11). https://doi.org/10.1029/2009GL038201

Thomson, J., Schwendeman, M. S., Zippel, S. F., Moghimi, S., Gemmrich, J. R., & Rogers, W. E. (2016). Wave-breaking turbulence in the ocean surface layer. *Journal of Physical Oceanography*, *46*(6), 1857–1870. https://doi.org/10.1175/JPO-D-15-0130.1

Thorpe, S. (1982). On the clouds of bubbles formed by breaking wind-waves in deep water, and their role in air-sea gas transfer. *Philosophical Transactions of the Royal Society A*, *304*(1483), 155–210. https://doi.org/10.1098/rsta.1982.0011

Veltcheva, A., & Guedes Soares, C. (2007). Analysis of abnormal wave records by the Hilbert–Huang transform method. *Journal of Atmospheric and Oceanic Technology*, *24*(9), 1678–1689. https://doi.org/10.1175/JTECH2067.1

Veltcheva, A., & Guedes Soares, C. (2016). Analysis of wave groups by wave envelope-phase and the Hilbert Huang transform methods. *Applied Ocean Research*, *60*, 176–184. https://doi.org/10.1016/j.apor.2016.09.006

Yurovsky, Y. Y., Kudryavtsev, V. N., & Chapron, B. (2017). Simultaneous radar and video observations of the sea surface in field conditions. *Paper presented at the 2017 progress in electromagnetics research symposium-spring (piers)* (pp. 2559–2565). IEEE. https://doi.org/10.1109/piers.2017.8262183

Zappa, C. J., McGillis, W. R., Raymond, P. A., Edson, J. B., Hintsa, E. J., Zemmelink, H. J., & Ho, D. T. (2007). Environmental turbulent mixing controls on air-water gas exchange in marine and aquatic systems. *Geophysical Research Letters*, *34*(10). https://doi.org/10.1029/2006gl028790

Article III

6.3 Statistical and dynamical characteristics of extreme wave crests assessed with field measurements from the North Sea

Mika P. Malila, Francesco Barbariol, Alvise Benetazzo, Øyvind Breivik, Anne Karin Magnusson, Jim Thomson and Brian Ward.

Journal of Physical Oceanography, under review, submitted 2022-06-07

Graphic design: Communication Division, UiB / Print: Skipnes Kommunikasjon AS

uib.no

ISBN: 9788230858561 (print)
9788230861042 (PDF)